PROBING DEFECTS AND ELECTRONIC PROCESSES ON GADOLINIA-DOPED CERIA SURFACES USING ELECTRON STIMULATED DESORPTION

A Dissertation
Presented to
The Academic Faculty

by

Haiyan Chen

In Partial Fulfillment
of the Requirements for the Degree
Doctor of Philosophy in Chemistry

Georgia Institute of Technology
May, 2006

PROBING DEFECTS AND ELECTRONIC PROCESSES ON GADOLINIA-DOPED CERIA SURFACES USING ELECTRON STIMULATED DESORPTION

Approved by:

Dr. Thomas M. Orlando, Advisor
School of Chemistry and Biochemistry
Georgia Institute of Technology

Dr. Meilin Liu
School of Materials Science and Engineering
Georgia Institute of Technology

Dr. Jiri Janata
School of Chemistry and Biochemistry
Georgia Institute of Technology

Dr. Phillip First
School of Physics
Georgia Institute of Technology

Dr. Robert L. Whetten
School of Chemistry and Biochemistry
Georgia Institute of Technology

Dr. Andrew Lyon
School of Chemistry and Biochemistry
Georgia Institute of Technology

Date Approved: December 8, 2005

This thesis is dedicated to my parents Qinglian Xi, Xinggui Chen
and my daughter Xuan Gui

ACKNOWLEDGEMENTS

First, I would like to sincerely thank my Advisor Professor Thomas Orlando for his guidance in my scientific growth. I am very grateful for his strong encouragement of independent thinking and his open-mindedness towards trying new ideas. His diversified research group has given me a healthy exposure to many scientific fields, from surface science, DNA damage, to astrobiology, and has enabled me to see the big picture of chemical science.

My Co-advisor Professor Meilin Liu has challenged me with both technologically and scientifically significant problems, supported my research with generosity in time, and made the collaboration with his group a great experience. Dr. Shaowu Zha, Dr. Jian Dong, and Mr. Zhe Chen from Professor Liu's group contributed directly to the sample preparation and characterization and have always been willing to answer my questions on fuel cells with patience and promptness. For all these I am very grateful.

I am also extremely grateful to Dr. Alexandr Aleksandrov, for his enthusiastic input at every stage of my project. Without his tireless coaching, mentoring, and theoretical expertise in radiation chemistry of solid state materials, I would never have been able to reach a reasonable understanding of the physics and chemistry of the intriguing system I have been working on. His philosophic view of science itself and the ways people approach science has had a great influence on me and will guide me in my future scientific endeavors. Most importantly, his support and interest in my work has contributed to the development of my self confidence and enthusiasm to begin my career in science.

During the course of my graduate study, Professor Robert Whetten and Professor Phillip First provided me with valuable opportunities to work in their laboratories. People from these two groups: Dr. Asmeron Ogbazghi, Mr. Tianbo Li, Mr. Jianfei Shao, and Mr. Ryan Price, helped me with hands-ons work in their labs. Professor Brent Carter from the School of Materials Science and Engineering trained me on XPS, which helped my research significantly. I would like to send my sincere thanks to all of them.

I am also very grateful for the professional help with my chamber construction generously provided by the following individuals of Georgia Tech: Mr. Norman Scott and Mr. Sam Mize from the Machine Shop, School of Physics; Mr. Donald Woodyard from the Glassblowing Laboratory, School of Chemistry and Biochemistry; and Mr. Richard Bedell from the Electronics Shop, School of Chemistry and Biochemistry.

I would like to thank my group members Dr. Janine Captain, Yanfeng Chen, Dr. Taishan Fan, Dr. Gregory Grieves, Ken Kite, Christopher Lane, Doogie Oh, Babajide Olanrewaru, Kristin Shepperd, and Lan Sun for offering help whenever needed, for asking stimulating questions, for reading and re-reading my draft papers, for sending articles on my interests in pdf files, and for sharing relaxing moments on Thirsty Thursdays at Rocky Mountain Pizza! I will cherish their comradeship and friendship all my life.

Outside of the Georgia Tech scientific world, there are many people helping me and my family altruistically. Particularly I would like to thank Dr. Kai Su, Mrs. Linda Su, and my four-year roommate Ms. Kristie Su for their affection and financial help. My friends Ms. Ying Zhang, Ms. Rebecca Kaizerman, Ms. Vivian Luo, Ms. Hong Yang, Dr.

Jun Sun, and Dr. Hong Qu are always there to support me emotionally and see me through hard times.

Finally, I would like to acknowledge the United States Department of Energy for financial support.

TABLE OF CONTENTS

LIST OF FIGURES

LIST OF SYMBOLS AND ABBREVIATIONS

Å	Angstrom
amu	Atomic mass unit
a. u.	Arbitrary units
DESD	Diffraction in electron stimulated desorption
E_a	Activation energy
EELS	Electron energy loss spectroscopy
E_i	Incident electron energy
EICO	Electron-ion coincidence
EPR	Electron paramagnetic resonance
ESD	Electron stimulated desorption
ESDIAD	Electron stimulated desorption ion angular distribution
ESR	Electron spin resonance
eV	Electron volts
FT-IR	Fourier transfer infrared spectroscopy
g	Grams
GDC	Gadolinia-doped ceria
h	Hour
HOMO	Highest occupied molecular orbital
HPLC	High performance liquid chromatography
Hz	Hertz
IEDP	Isotope exchange depth profiling

IP	Ionization potential
K	Kelvin
K-F	Knotek-Feibelman
KJ	Kilojoules
kV	Kilovolts
L	Langmuir
LSVCs	Linear surface oxygen vacancy clusters
LUMO	Lowest unoccupied molecular orbital
mA	Milliamps
meV	Milli electron volts
MGR	Menzel-Gomer-Redhead model
min	Minutes
ML	Monolayer
mm	Millimeter
mol	Mole
NC-AFM	Non-contact atomic force microscopy
nm	Nanometer
pA	Picoamps
Pa	Pascal
PSD	Photon stimulated desorption
QMS	Quadrupole mass spectrometry
REMPI	Resonance enhanced multi-photon ionization
s	Second

SEM	Scanning electron microscopy
SIMS	Secondary ion mass spectrometry
SOFC	Solid oxide fuel cell
STM	Scanning tunneling microscopy
SVTs	Surface oxygen vacancy trimers
TOF	Time of flight
TPB	Triple phase boundary
TPD	Temperature programmed desorption
UHV	Ultra-high vacuum
UPS	Ultraviolet photoelectron spectroscopy
UV	Ultraviolet
V	Volts
Va	Anion vacancy
VCs	Vacancy clusters
XANES	X-ray adsorption near-edge spectroscopy
XPS	X-ray photoelectron spectroscopy
XRD	X-ray diffraction
$Y_{ESD(O^+)}$	Yield of electron stimulated O^+ desorption
YSZ	Yttria-stabilized zirconia
μm	Microns
μs	Microsecond

SUMMARY

Polycrystalline gadolinia-doped ceria (GDC) has been widely investigated as a promising low temperature solid oxide fuel cell (SOFC) electrolyte and as part of composite electrodes. In this research, electron stimulated desorption (ESD) has been used to probe the electronic properties of GDC surfaces and the interactions of water and molecular oxygen with these surfaces.

H^+, O^+, and H_3O^+ are the primary electron stimulated cation desorption products from GDC surfaces. The investigation of ion kinetic energies and yields show that the charging of GDC by electron beam bombardment is dependent on the incident electron energy: negative at lower energy and positive at higher energy. The positive charge caused by high energy electron irradiation can be neutralized by the negative charge generated by low energy electrons and vice versa. The gadolinium aggregated, oxygen vacancy rich grain boundaries can serve as very effective electron traps as well as hole traps.

The threshold energy data of H^+ and H_3O^+ indicate the presence of hydroxyl groups and chemically adsorbed water molecules on the GDC surfaces at room temperature. ESD temperature dependence measurements of GDC reveal that the interaction of water with surface defect sites, mainly oxygen vacancies, influences the desorption of H^+, O^+ and H_3O^+. The temperature dependence study of O^+ desorption yields an activation energy of 0.21 eV for O^+ desorption, which is close to the energy needed for oxygen vacancy production on ceria surfaces.

Highly efficient electron stimulated O^+ desorption from highly defective gadolinia-doped ceria surfaces was observed and is associated with electronic excitation of Ce 5s and Gd 5s core levels and electron transfer from the O 2p level to empty defect states. As a result of this transfer, the electron density of oxygen anions is reduced and the cross section for O^+ emission is increased. Water and molecular oxygen heal the defects through adsorption to vacancy sites and decrease the O^+ ESD yields. The activation energy for positive charge dissipation has been evaluated to be 0.43 eV via O^+ kinetic energy measurements. This 0.43 eV is close to the activation energy for ionic conduction of GDC measured from other methods.

Electron stimulated desorption of O_2^+ from gadolinia-doped ceria surfaces during and after molecular oxygen adsorption also shows the ability of ESD to detect chemically adsorbed O_2. The velocity distributions of O_2^+ can be used to probe intermediate adsorption species such as O_2^-, as well as the positive charge of the surface.

In summary, ESD can provide important information on the kinetics and dynamics of surface charging, charge transport, adsorption and reactions occurring at defective insulating metal oxides materials. These abilities make ESD a valuable technique for surface chemistry and catalysis studies.

CHAPTER 1

INTRODUCTION

1.1 Solid oxide fuel cell (SOFC)

In the time of looming energy crisis and worsening environmental pollution caused by energy industries, technologies that can enhance the energy efficiency of existing fossil fuels without damaging the fragile environment is highly desired. In the past two decades, solid oxide fuel cell (SOFC) technology has regained steady research and industrial interests because of it's overall high energy conversion efficiency (~80%) and environmental benignity.[1-7] Scientific and technological investigations into various aspects of SOFCs have been active and improvements have been made in the increase of power density and decrease of the severity of the operation conditions. For example, increase in power density from 250 mW / cm^2 @ 1000 °C to 2 W / cm^2 @ 800 °C has been achieved for laboratory planar cells operated on hydrogen with the advancement in structural design and in materials.[8] A single chamber fuel cell has been demonstrated and may enable greatly simplified and compact fuel cell design.[9]

A single-cell solid oxide fuel cell has three basic components, a cathode, an electrolyte, and an anode as shown schematically in Figure 1.1. During operation, oxygen is reduced at the cathode to oxygen ions, which are conducted by the electrolyte to the anode side and react with fuel to produce electrical energy. An ideal fuel cell electrolyte should be highly ionically conducting, impermeable to gases, electronically resistive, and chemically stable under a wide range of conditions. For fuel cell electrodes, they must

transport gaseous reactants, ions, electrons, and catalyze electro-oxidation at the anode or electro-reduction at the cathode.

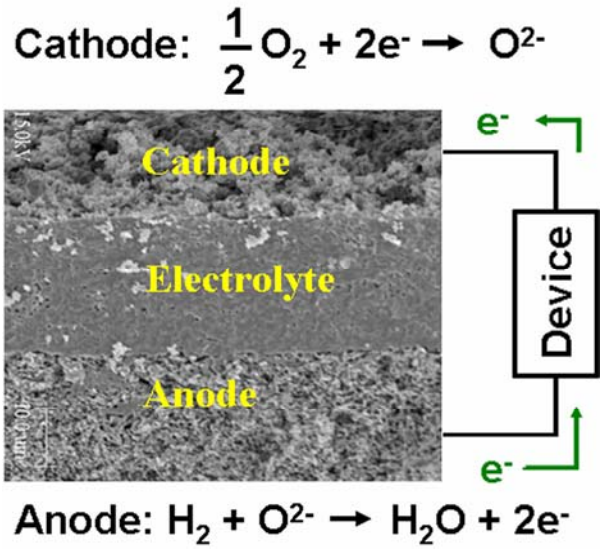

Figure 1.1 Schematic of a solid oxide fuel cell comprised of a porous anode, an electrolyte, and a porous cathode. Anode and cathode reactions given are only for hydrogen fuel and oxide ion conducting electrolyte.

The efficiency of fuel cells depends on the internal losses including the ohmic resistance of the electrolyte, as well as the overpotential losses at the anode and cathode. The ohmic losses in oxide electrolytes are well understood and can be minimized by making thinner, less resistive electrolyte films. Currently almost all SOFCs systems being developed employ an yttria-stabilized zirconia (YSZ) electrolyte. YSZ has high oxygen ion conductivity, good chemical stability, low in cost, easy to fabricate, but requires an operating temperature above 850 °C. As a consequence of the high operation temperature, the severe demands on materials and fabrication make the SOFC technology very

expensive. Therefore, there is great interest in lowering the operating temperature to enable the use of cheaper materials to reduce fabrication costs.

With current fabrication technologies, the thickness of electrolyte films supported on the anode or cathode has reached 10 - 15 μm, which can lower the operation temperature significantly.[6] On the other frontier, non-YZS based electrolyte material, such as gadolinia doped ceria (GDC), has been actively pursued as a promising potential electrolyte for SOFC to be operated between 500 to 600 °C. If the operating temperature is lowered to around 500 °C, the internal loss from the overpotentials of electrodes surpasses the ohmic resistance loss and becomes dominant. Since the activation of oxygen reduction is generally believed to be more difficult on SOFCs operating at relatively low temperatures, reducing of overpotentials caused by slow cathode reaction has been a focus of research. Understanding the mechanisms of oxygen reduction and the physics governing the electrode overpotential losses is crucial in developing technologies that allow the fuel cells to operate at a commercially viable temperature.

A typical SOFC cathode is made of porous electrode materials cast onto an electrolyte. Reduction of oxygen on the cathode involves three phases: molecular oxygen from the gas phase, the electronic conducting phase, and the ionically conducting phase. The reaction is commonly believed to occur at a three-phase (or triple phase) boundary (TPB) where oxygen can interact with both the electronically and ionically conductive phases simultaneously.[10] Oxygen molecules are generally thought to adsorb onto the surfaces of one or more solid phase where they undergo catalytic and / or electrocatalytic reduction steps to form partially reduced ionic or atomic intermediates. At any stage of the partial reduction, these intermediates can migrate along surfaces, interfaces, or inside

the bulk of the electrode to be incorporated as O^{2-} in the electrolyte. Even though oxygen reduction at the cathode has been intensively pursued for decades, this very complicated process is only empirically understood from electrochemical measurements and modeling techniques. So far, no proposed mechanism explains the reduction of oxygen on all electrodes, and disagreements in the literature concerning rate-limiting steps and factors important for cathode performance are frequent.

To understand this elusive and challenging process experimentally, new surface specific techniques should be employed to uncover the fundamentals regarding the interactions of oxygen with the surfaces of the cathode and electrolyte. Since most materials used in SOFCs are mixed oxides with intrinsic defects which play critical roles in chemical reaction and ionic transport, techniques sensitive to surface defects, such as Electron stimulated desorption (ESD), are highly desirable in this context.

1.2 Electron stimulated desorption (ESD)

The electron stimulated desorption (ESD) of energetic cations, anions, and neutrals from surfaces or adsorbates on the surface has been extensively studied since the 1960's and periodically reviewed.[11-15] Materials that have been studied by ESD techniques include metals, transition metals, highly ionic oxides, alkali-halide solids, and semiconductors. Adsorbates investigated by ESD include physisorbed noble gases, chemisorbed small molecules, and bio-organic molecules on various substrate surfaces. Rich information on substrate surface structure, surface defect structure, bonding geometry such as bonding length and orientations of adsorbates on single-crystal surfaces,

substrate-adsorbate interactions, and the production of catalytic intermediate species can be deduced from ESD measurements.

Electron stimulated desorption ion angular distribution (ESDIAD) is a good example to showcase the power of electron stimulated desorption. In ESDIAD measurements, interactions of low energy electrons with absorbed atoms or molecules on single crystal surfaces produce narrow positive ion beams.[16] These ion beams have sharp angular distributions which often are in registry with certain crystallographic azimuths of the single crystal substrate. This angular distribution is primarily determined by the directionality of the chemical bonds being broken, and therefore can give information concerning the orientations of the parent adsorbed molecules. Since any movement of adsorbed molecules on the surface can induce the variation of bonding geometry, the ESDIAD measurements of the range of angular distortion can be used to directly observe the dynamic behavior of the surface species.

ESD has been considered mainly as a characterization technique, but recently its potential as a nanometer scale surface processing method has been proposed in the form of diffraction in electron stimulated desorption (DESD).[17-19] DESD manifests itself as a periodic variation in the desorption rate as a function of the incident electron beam direction. Analysis of DESD patterns can be pursued as a potential tool to determine desorption sites of unknown structures with sub-Angstrom resolution of bond vectors with the help of more sophisticated theoretical treatment. The difference in desorption rate, on the other hand, means selective desorption of adsorbates may be controlled and manipulated by varying the energy and direction of the incident electron beam. This

provides a parallel technique to pattern the surface with the adsorbate and this may be very useful in nanotechnology.

In principal, ESD is treated as the result of an electron-adsorbate inelastic scattering event where direct momentum transfer is usually not dominant. Electronic energy transfer processes play a central role in ESD. The interaction of electrons with solid surfaces can cause not only bond breaking events on the surface, but electron impact induced chemical conversions of molecules on surfaces as well. Several physical mechanisms to explain ESD phenomena from different types of surfaces and the chemical consequences of ESD effects on adsorbates have been developed to explain the nature of ESD.

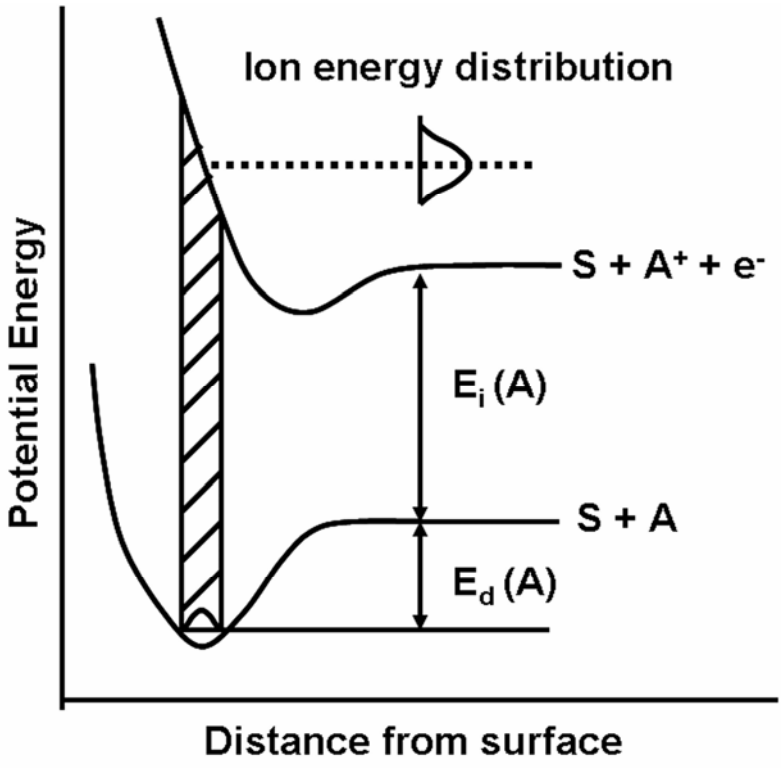

Figure 1.2 Schematic potential energy curves for the Menzel-Gomer-Redhead model. S stands for surface and A for adsorbate. $E_d(A)$ is the binding energy of A to S and $E_i(A)$ is the ionization potential of A.

One of the earliest models shown in Figure 1.2 is the Menzel-Gomer-Redhead (MGR) description which is based on the Frank-Condon principle.[20,21] Electronic excitations of a bonding substrate-adsorbate (S+A) system can create a repulsive state S + A^+ + e $^-$ from which A^+ may desorb with a range of kinetic energies. Reneutralisation of A^+ may result in a bonding state from which excited neutrals may be produced. The total ESD cross section is then the product of the primary excitation cross section and total desorption probability which is determined by reneutralisation. This model predicts much higher neutral desorption than ionic desorption, which is verified experimentally. A modification of the original MGR mechanism, Antoniewicz model, is successful in describing ESD from physisorbed layers.[22]

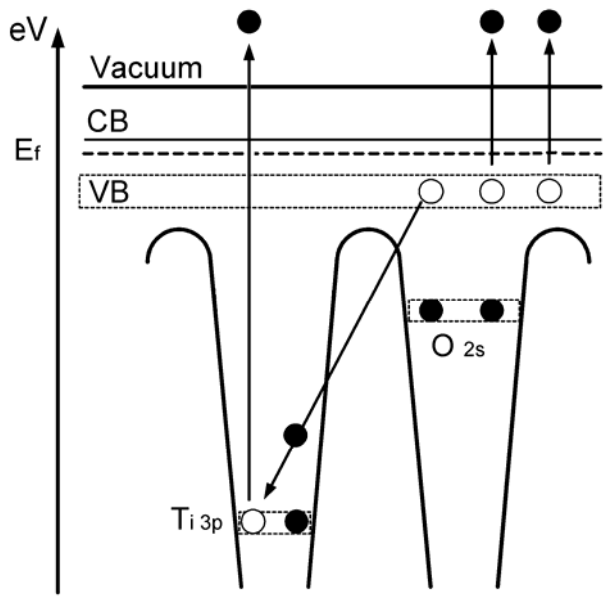

Figure 1.3 Energy diagram for the TiO_2 and the Knotek-Feibelman desorption mechanism. VB stands for valence band, CB for the bottom of conduction band, E_f for Fermi level, solid circle for electron, and hollow circle for hole.

Another mechanism which has gained widespread application in describing the electron stimulated desorption of O^+ from metal oxide surfaces was proposed by Knotek and Feibelman (K-F mechanism).[23] Figure 1.3 is an illustration of O^+ desorption from TiO_2 surface by this mechanism. K-F model involves the ionization of a metal core level where a core hole is produced. This core hole is filled with electrons from the valence band primarily associated with oxygen atoms via an inter-atomic Auger process, removing enough electrons from O^{2-} to produce O^+. This O^+ then is ejected from the surface by Coulomb repulsion from the coordinating cations. K-F mechanism accounts for the observed ion kinetic energies and desorption threshold energies, which are supposed to be binding energies of metal core levels. In the K-F mechanism, the metal core level is envisioned as the highest occupied level so intra-atomic Auger process, which is much faster than inter-atomic Auger process, would not occur. This means that if the metal in the metal oxides is not in its highest oxidation state, no O^+ desorption should be observed, which is not in agreement with experimental findings.

Recently, a new mechanism based on electron-ion coincidence spectroscopy (EICO) study of photostimulated ion desorption from $TiO_2(110)$ and $ZnO_2(1010)$ surfaces was proposed.[24] In this new model, for metals with d or f orbits, the core holes created by electronic ionization can lower the potential of the lowest unoccupied d or f levels, enabling the electron transfer from O 2p to the d or f levels of the metal. This charge transfer thus lowers the electron density on oxygen anions so no inter-atomic Auger process is required for O^+ desorption. There is still much to be done to further verify this model, but this demonstrates that there are still many grey areas in our understandings of electron stimulated desorption and continued research efforts are

needed to advance our knowledge on ESD. For example, stimulated desorption by secondary electrons is one of the least well-understood aspects of ESD. How excitons, secondary electrons, hot holes created by electronic excitation in the bulk are transported to the surface is still under investigation on a case by case basis. The influence of surface and bulk defects on ESD has been observed in many occasions but still needs to be fully understood for this technique to be meaningful in the investigation of materials with intrinsic defects. The application of ESD in the study of SOFC related metal oxide materials then represents challenges and opportunities. This research project is motivated by the scientific and technological potentials presented by this combination.

1.3 Electron stimulated desorption study of metal oxides surfaces

Metal oxides are scientifically intriguing and technologically critical materials in many areas including SOFC. The metal oxides investigated by electron stimulated desorption range from stoichiometric to non-stoichiometric oxides.[25] In general, the cations desorbed from metal oxides surfaces are mainly H^+, O^+ and H_3O^+ (historically indentified as F^+). Extensive studies of single crystal TiO_2 surfaces by ESD and ESDIAD as model surfaces display the capabilities of this technique in the characterization of the structure of metal oxide surfaces. Kinetic energy measurements of O^+ ESD from TiO_2(110) surfaces were used to distinguish oxygen atoms from bridging sites or in-plane sites. The ESDIAD study of the thermal reconstruction of TiO_2 surfaces contributes significantly to resolve the nature of surface oxygen bonding upon transformation of the surface from (1 × 1) to (1 × 2).[26] Enhancement of O^+ yields by the presence of defects

created by Ar^+ bombardment was observed and correlated with desorption from step edges.

Application of ESD to non-stoichiometric oxides has been explored but these types of studies are not as abundant as those on metal oxide single crystals. Observation of both O^+ and O_2 neutral ESD from YBaCuO provides insight into the structure of this superconductor material.[27-29] The ESD of ions from mineral oxide surfaces of relevance to the origins of Na and K in the atmosphere of Mercury and the Moon has been performed to understand planetary findings.[30] Application of ESD to insulating metal oxides is rare and not very successful. For example, ESD studies on insulating MgO(100) surfaces are not as conclusive as those on the semi-conducting TiO_2 surfaces due primarily to severe surface charging.[31,32]

ESD and ESDIAD studies of the interactions of molecules with oxide surfaces reveal important information on adsorption and surface reactivity. These types of study gives the information on preferred adsorption sites, the nature of adsorption, bond formation, and bonding geometry. Interactions of metal oxide surfaces with small molecules such as H_2O, NH_3, SO_2, CO, H_2, NO, and O_2, which are important to catalysis, have been studied and oxygen deficient surfaces are found to be more reactive than nearly perfect surfaces. Adsorption of relatively large molecules such as CH_3-COOH and C_6H_5COOH onto TiO_2 surfaces illustrates how surface carboxylate species are oriented on the surface and the rotation of -CH_3 group along the C-C bond can be visualized by H^+ ESDIAD.[33,34]

1.4 Electron stimulated desorption study of GDC

In the previous section, electron stimulated desorption has been discussed as an effective tool in the study of metal oxide surfaces and is employed in this research to study the surfaces of gadolinia-doped ceria. Gadolinia-doped ceria is chosen because of its material significance as a low temperature SOFC electrolyte and as a composite of electrodes.[35-39] Extensive research efforts have been undertaken to investigate the preparation,[40-47] electronic and ionic conductivity,[46,48-57] and surface oxygen exchange and mass transport[57-60] of GDC but surface specific techniques have not been widely explored. X-ray photoelectron spectroscopy (XPS) and X-ray adsorption near edge spectroscopy (XANES) have been occasionally used for the characterization of oxidation states of the elements and the interrogation of the influence of dopants on GDC properties.[61]

Electron stimulated desorption studies of GDC face several severe challenges. First, the electronic conductivity of GDC is very low so surface charging will be a major problem. Understanding and controlling of the surface charging are among the most important issues to address. Second, the heterogeneity of the surface morphology of GDC imposes difficulties in data interpretation. Most ESD studies are done on single crystal surfaces which are better understood than polycrystalline surfaces. On GDC surfaces, the random orientations of grains and the presence of large amounts of grain boundaries not only prohibit the use of ESDIAD, but also add the complication of mechanistic analysis of the results. Third, insufficient knowledge on the electronic structure of GDC makes the identification of the electronic excitations involved difficult. Last, the various defects on

the surface or in the bulk, including intrinsic and induced oxygen vacancies and vacancy clusters, will increase the dimension of complexity of the study exponentially.

However, with the sophisticated experimental techniques and advancements in theoretical understandings of the mechanisms of ESD, all the above obstacles are not insurmountable. The insights gained from this research would greatly enlarge our arsenal to attack issues involving defective surfaces and contribute significantly to the elucidation of surface processes important to SOFC's eventual commercialization.

CHAPTER 2

EXPERIMENTAL

2.1 GDC Sample preparation[46]

The $Ce_{0.9}Gd_{0.1}O_{2-\delta}$(GDC) samples were prepared using a glycine-nitrate process. Stoichiometric amounts of $Ce(NO_3)_3 \cdot xH_2O$ (Aldrich, 99.99%) and $Gd(NO_3)_3 \cdot xH_2O$ (Aldrich, 99.9%) were dissolved in distilled water, to which 0.5 mol glycine per mole nitrate was added. Combustion of the metal nitrate–glycine solution was performed in a glass beaker on a hotplate, with about 20 ml of the solution (0.1 mol with respect to metal ions) burned at a time. The precursor solution turned to a brown-red gel as solvent was evaporated and then spontaneous ignition occurred, leading to pale-yellow ash. The resultant ash was then collected and calcined in air at 600 °C for 2 h to remove any carbon residues remaining in the oxide powder. The calcined GDC powder was cold pressed under 250 MPa into cylindrical pellets (10 mm diameter and ~1 mm thickness) using a uniaxial die-press. The electrolyte thickness was controlled by the amount of GDC powder. The GDC pellets were subsequently fired at 1250–1450 °C for 5 h with a heating rate of 2 °C/min and a cooling rate of 10 °C/min.

2.2 Sample characterization[46]

The relative densities of the sintered GDC pellets were measured using the standard Archimedes method. The phase compositions of the as-synthesized ash, calcined

GDC powders, and the sintered GDC pellets were studied using X-ray diffraction (XRD, PW-1800 system, with Cu-Kα radiation operated at 40 kV and 30 mA, and a 2θ scanning rate of 0.2°/min). The morphologies of the ash and sintered samples were revealed using a scanning electron microscope (SEM, Hitachi S-800). The specific surface area of the GDC powder was measured by an isothermal nitrogen adsorption–desorption measurement (Coulter SA3100). XPS data were acquired using a Surface Science Laboratories Model SSX-100 Small Spot ESCA Spectrometer containing a monochromatized Al Kα X-ray source. An electron gun SPI Model 9602 True Spot was used to control specimen charging. Spectra were collected for a 400–800 μm diameter X-ray spot size.

2.3 Setup for Electron stimulated desorption (ESD)

The basic experimental setup for ESD includes an ultra high vacuum (UHV) chamber (base pressure 2×10^{-10} torr), a sample manipulator, a pulsed low-energy electron gun, a quadrupole mass spectrometer (QMS) and / or a time-of-flight (TOF) mass spectrometer, and a calibrated dosing system. The schematic of a typical UHV system used in these experiments is shown in Figure 2.1.

The sample manipulator consists of a rotatable sample holder, a button heater to heat the sample and a cryohead to cool the sample. The sample holder is made of a tantalum sheet to which the GDC pellet and the button heater are attached to both sides back to back. This assembly is then mounted to the end of a cryohead with a sapphire plate between the tantalum sheet and cryohead as an electrical insulator. The thermal

conductivity of sapphire is low at high temperature but high at low temperature, a property that helps maintain the electrical insulation without blocking cooling. The sample can be either grounded or biased through the tantalum sheet via an electrical wire. This design allows the sample temperature to be controlled from 100 K to 900 K.

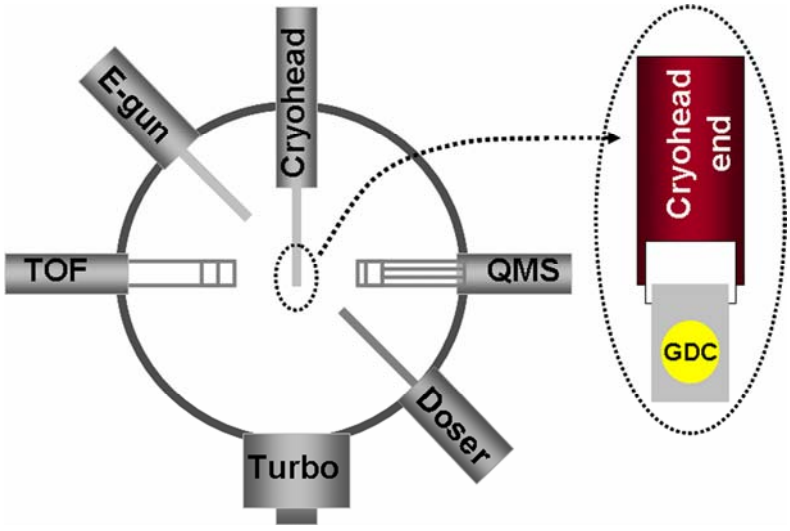

Figure 2.1 Schematic of a typical UHV system for electron stimulated desorption study. Enlarged is the sample holder attached to the end of the cryohead.

The low energy electron-gun for ESD is an ELG-2A system from Kimball Physics which has an operating energy range from 5 eV to 1000 eV with an energy spread of 0.4 eV. The beam current can be varied from 1 nA to 10 μA and fast pulsing can be done in the 20 ns to 100 μs range with a capacitive pulse junction box. The beam diameter is ~ 1 mm in the energy range we use. The beam current at different electron energies is calibrated with a Faraday cup in pulsing mode and is used to normalize the ion yields. The angle of the incident electron beam is 45° relative to the sample normal and the irradiation condition can be varied over a broad range of parameters.

Both a quadrupole mass spectrometer (Extrel) and time-of-flight mass spectrometer (custom made) can be used to detect the desorbed ions and neutrals from ESD with the appropriate setup. The QMS is primarily used to monitor the composition of gas phase or in temperature programmed desorption (TPD) measurements. If the QMS is employed in ion detection, its ionizer needs to be turned off so only the ions from ESD can be detected. Under this condition, the QMS can either operate in a voltage scanning mode to detect ions with different masses or in a constant voltage mode to monitor just one mass, which is useful in determining the velocity distribution of the ion of interest. If the ionizer is turned on, the QMS can detect both ions and neutrals, which also includes neutrals from electron stimulated desorption. However, because of the electron impact ionization of the residue gas in the UHV chamber, background noise level is always carefully monitored during the experiment. The time-of-flight mass spectrometer is a natural choice for the detection of desorbed ions and is generally more sensitive than the QMS. The ion optics can be easily set for ion kinetic energy distribution measurements. If the TOF is intended to detect neutrals, a separate ionization source, usually laser ionization, should be implemented.

The directional vapor dosing line consists of a stainless steel doser fitted to the inlet of a leak valve mounted on a translational stage. The dosing line is equipped with a liquid nitrogen trap to minimize the contamination from organics in the dosing manifold. For water dosing, the water to be dosed is purified by several freeze-pump-thaw cycles to remove dissolved gas, and the dosing lines are passivated with water vapor by several cycles of saturating and evacuating. The exposure is calibrated by QMS and controlled by the dosing pressure and time.

2.4 Experimental procedures

With our experimental setup, the experimental variables are: sample temperature, sample potential, extraction potential of the TOF extraction lens, incident electron energy, electron flux, and the electron pulse length. The properties of the desorbing species are measured by mass spectra, total ion yields, and velocity distribution (i.e. kinetic energy distribution).

The GDC sample was mounted to the tantalum sheet by spot wielding with tantalum strips and was annealed to 400 ºC to remove all organic contaminants from the surface. The sample was irradiated by the pulsed electron beam at 1000 Hz with an electron flux of 10^{14} electrons/cm^{2}s during a given pulse or time-averaged currents of 200 pico-Ampere to a few nano-Ampere.

Emitted cations were collected by applying a pulsed extraction potential to the TOF front lens assembly just after the end of the electron pulse to avoid the influence of the potential field on the incident electron energy. The pulse length for the electron gun was chosen according to experimental needs and the pulse length for TOF extraction was 100 μs. Both pulses were delivered by a pulse generator. All ions were detected using pulse counting and a transient digitizer and the yields were normalized to the electron beam current.

Ion kinetic energy distributions are converted from ion velocity distributions measured under free field condition using either the TOF or QMS operated in constant mass mode. The distance from the sample to the detector is fixed and known. To convert

velocity distribution dN/dt to kinetic energy distribution dN/dE, the Jacobian transformation was used.

$$\frac{dN}{dE} = \frac{dN}{dt} \times \frac{t^3}{mL^2} \quad (1)$$

t: flight time

m: mass of ions

L: distance from the sample surface to detector

CHAPTER 3

CHARGING EFFECTS ON ELECTRON STIMULATED DESORPTION OF CATIONS FROM CADOLINIA-DOPED CERIA SURFACES

3.1 Overview

Electron beam induced charging and stimulated desorption have been used to probe the electronic properties of gadolinia-doped ceria (GDC) surfaces. The main cationic desorption products resulting from electron bombardment are H^+, H_3O^+ and O^+. The dependence of the H^+ and H_3O^+ ion kinetic energies and yields on the surface potentials have been systematically investigated. Positive potentials increase the cation kinetic energies linearly while negative potentials reduce the cation yields dramatically. The charging of GDC by electron beam bombardment is dependent on the incident electron energy: negative at lower energy and positive at higher energy. Irradiation with 400 eV electrons can produce a positive surface potential of several volts while irradiation of the sample with 75 eV electrons can produce a negative sample potential of at least -6 V. The positive charge caused by high energy electron irradiation can be neutralized by the negative charge generated by low energy electrons and vice versa. The probable hole-traps are sites close to Gd^{3+}, and the abundant presence of defects at oxygen vacancy rich grain boundaries can serve as very effective electron traps. Most of the information in this chapter has been published in Applied Surface Science, 243 (2005) 166.

3.2 Background

Solid oxide fuel cells (SOFCs) are highly efficient and environmentally benign chemical-to-electrical energy conversion devices with excellent fuel flexibility [6,8,62-65]. Largely due to their high operating temperatures (800 to 1000 ºC), the cost of SOFC systems is still too high to be commercially viable. However, the interfacial polarization resistances of the current SOFCs increase rapidly as the operating temperature is reduced, and severely limit fuel cell performance. In the search for SOFC materials suitable for low-temperature operation, a fundamental understanding of the defect mediated reactions at the surface and interface of electrolytes/electrodes is imperative. In particular, ceria-based solid electrolytes have attracted much attention [36] because of their high ionic conductivities at low temperatures. Among them, gadolinia-doped ceria ($Ce_{0.9}Gd_{0.1}O_{2-\delta}$, GDC) shows great promise for low-temperature SOFCs [46,66] and can thus serve as a model material for the exploration of surface properties relevant to electrochemical performance. Thus far, regarding surface reactions on GDC, only the oxygen surface exchange reaction has been investigated using isotope exchange depth profiling (IEDP) via secondary ion mass spectrometry (SIMS).[57,59,67] With IEDP-SIMS, the activation energy for the oxygen surface exchange reaction was found to be 0.9 eV for temperatures below 700 °C and 3.3 eV for temperatures above 700 °C. Similar energies were obtained for a single crystal GDC ($Ce_{0.69}Gd_{0.31}O_{1.845}$), i. e., 1 eV for temperatures below 650 °C and 2.41 eV for temperatures above 650 °C.[57] Apparently, the understanding of this

surface oxygen exchange process at an electronic level has yet to be realized by other surface specific analytical techniques.

Electron stimulated desorption (ESD), or desorption induced by electronic transition (DIET), is an effective technique [13,25] that can provide valuable information on the structure of adsorbates and on the dynamics of charge transfer. Defects or local disorder on a surface, which may act as trapping sites of electronic excitations, can serve as preferential sites for desorption. Therefore, ESD can be a useful technique for exploring defects and their role in surface reactions critical for electrochemical performances of SOFCs.

For decades, ESD has contributed significantly to the study of the structure and the surface reactivity of non-stoichiometric and stoichiometric oxide surfaces. Since the electronic conductivity of most metal oxides is very low, very thin layers of metal oxides prepared by various deposition or growth techniques were used in many investigations in order to avoid the complications caused by surface charging. The structure and composition of these prepared oxides can vary and may be different from those used for industrial purposes. For the few studies done on bulk crystalline or amorphous dielectric oxide samples, unexplainable results were encountered even under standard conditions. For example, ESD of MgO(100) has been studied by Gotoh et. al. [32] and O^+ desorption thresholds at 80 eV and 210 eV were found. These values are quite far from the Mg 2s excitation level at 50.8 eV. A similar study of MgO(100) surfaces obtained a 55 eV threshold after a +11 V correction for sample charge [31]. On the semi-conductive TiO_2(110) surface, an onset at about 100 eV for O^+ ion desorption was observed after dosing CO. This threshold does not correspond to any core levels of either O or Ti [68]. In

an ESD and photon-stimulated desorption study of yttria-stabilized ZrO_2 (100), the sample was kept at 400-500 K to prevent charging [69], and thresholds at the Zr 4p and O 2s levels were observed.

In this chapter, we present a study of electron induced surface charging effects on the electron stimulated desorption of cations from the surfaces of GDC, a dielectric metal oxide. For this defective metal oxide, surface charging depends strongly on incident electron energy and other parameters such as current density, pulse length, and irradiation time. The results illustrate the influence of charging on the kinetic energies and yields of ejected ions. Collectively, the results reveal details regarding electronic properties of the surface.

3.3 Experimental details

3.3.1 Sample preparation and characterization

The $Ce_{0.9}Gd_{0.1}O_{2-\delta}$(GDC) samples were prepared using a glycine-nitrate process as described elsewhere [46]. Briefly, a flammable solution containing metal (Ce, Gd) nitrate and glycine was combusted in a glass beaker on a hot plate, producing a pale-yellow ash, which was then calcined in air at 600 °C for 2 hours to form the fluorite structure. The resulting GDC powder was then ball-milled and cold pressed into cylindrical pellets under 250 MPa. The green pellets were subsequently fired at 1250–1450 °C for 5 hours with a heating and cooling rate of 5 °C/min in air to achieve greater than 95% relative density. The crystal structure of the GDC samples was studied using X-ray diffraction

(XRD, PW-1800 system, with Cu-Kα radiation operated at 40 KeV and 30 mA,) and the morphologies of the sintered samples were revealed using a scanning electron microscope (SEM, Hitachi S-800).

3.3.2 Electron stimulated desorption (ESD)

The ESD measurements were carried out in an ultra-high vacuum chamber (base pressure 2×10^{-10} torr) equipped with a rotatable helium-cooled sample holder, computer-controlled resistive tungsten sample heater or button heater, quadrupole mass spectrometer (QMS), time-of- flight (TOF) mass spectrometer, pulsed low-energy electron gun, and a calibrated dosing system. Details of the system have been discussed in Chapter 2 and elsewhere [70].

The dimensions of the GDC sample used for the ESD experiments were 10 mm × 6 mm and the thickness was ~ 1 mm. The GDC sample was mounted to a conductive molybdenum plate which was used to heat the sample and to apply the bias. The sample was annealed to 400 ºC to clean the surface and the ESD of H_3O^+ and O^+ was measured at room temperature (300 K) while the proton ESD was studied at 230 K. Irradiation of the sample (grounded or with an externally applied potential) was performed by the pulsed electron beam operated at 1000 Hz. The electron energy, flux, and pulse length were varied over a wide range, depending on the purposes of the experiment. Typical operating conditions were 10^{13} electrons/cm^{2}s during a given pulse or time-averaged currents of 20 pico-Ampere to a few nano-Ampere. Variation of the electron flux was performed exclusively by changing the gun emission current. Since we utilized a pulsed

electron beam, the ESD of ions was measured by either a TOF or quadrupole mass spectrometer (QMS), both with better than unit mass resolution. When using the TOF, emitted ions were usually collected by applying a -100 V pulsed extraction potential to the front lens assembly. The -100 V potential was high enough to ensure a large solid angle of collection and to rule out any discrimination against off-normal trajectories or ion angular distribution effects. The extraction pulse was applied just after the end of the electron pulse to avoid the influence of the potential field on the incident electron energy. All ions were detected using pulse counting and a transient digitizer.

No extraction pulse was used to measure accurate kinetic energy distributions of emitted ions. Since detection sensitivity is reduced under field free conditions, only the velocity distribution of the departing protons and hydroxonium (H_3O^+) were measured. When using the QMS as a mass analyzer, the ions were detected with its ionizer turned off. Calculations of ion velocities (and thus kinetic energy) from TOF and QMS were based on known path lengths from the sample to the detector and measured flight times.

3.4 Results and discussion

3.4.1 Sample Characterization

Figure 3.1 shows a typical XRD pattern of a GDC sample, indicating that it has a single-phase fluorite structure, the same as that of CeO_2. Shown in Figure 3.2 is the SEM image of the surface morphology of an as-sintered GDC sample. The grain size varies from 1 to 5 μm, and the sample has a significant number of grain boundaries and triple

junctions. According to the electron energy loss spectroscopy (EELS) profile across the grain boundary [71], there is an excess of oxygen vacancies and gadolinium cations in the grain boundary core. The width of the grain boundary core is about a few nanometers while the width of the depletion layer can be larger than 15 nm. Assuming an average grain size of ~ 2 μm with its surface dominated by structural defects that can trap free charges at a density of ~ 10 traps / nm^2, the volumetric trap density is estimated to be ~ $10^{18\sim19}$ traps / cm^3. A scanning tunneling microscopy (STM) study revealed that the dominant defects on the surface of nonstoichiometric CeO_2 (111) are triangular with three oxygen vacancies at room temperature and linear at elevated temperatures [72]. The defect structure of the GDC grain should be close to that of the nonstoichiometric CeO_2, but the defect structure of the grain boundary can be very complicated.

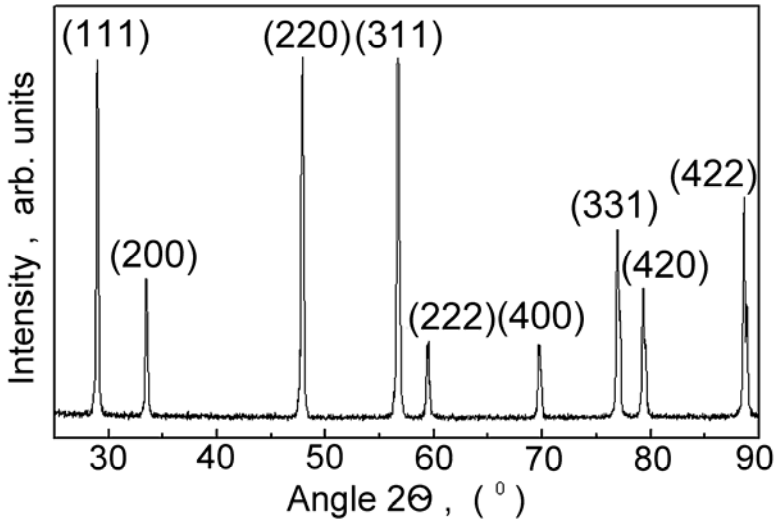

Figure 3.1 X-ray diffraction pattern of a sintered $Ce_{0.9}Gd_{0.1}O_{2-\delta}$ (GDC) pellet which indicates the fluorite structure.

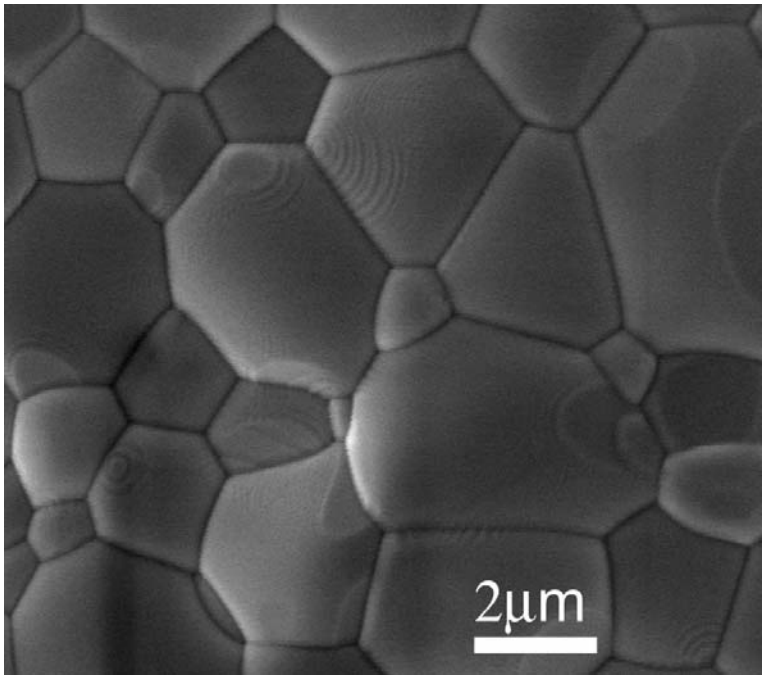

Figure 3.2 SEM image of the morphology of a sintered $Ce_{0.9}Gd_{0.1}O_{2-\delta}$ (GDC) pellet which shows that the sample has a significant number of defective grain boundaries and triple points on its surface.

3.4.2 ESD of cations

Electron irradiation of polycrystalline GDC causes emission of atomic and molecular ions. The dominant positively charged ions emitted from this annealed substrate are protons. Compared to proton emission, the emission of other ions, mainly H_3O^+ and O^+, occurs with one to two orders of magnitude less efficiency (Figure 3.3).

The experimental primary threshold energy for proton ESD from GDC is 22 eV, and is associated with an initial ionization of the O 2s level that Auger decays. The proton desorption involves the production of 2-hole states localized on hydroxyl groups which Coulomb explode directly at the surface. The O^+ threshold energy is also 22 eV, corresponding to direct ionization of O 2s, Ce 5p, or Gd 5p levels followed by an intra- /

inter-atomic Auger cascade [23]. The threshold energy appears to be lower than 22 eV for the molecular ion H_3O^+. The H_3O^+ ESD likely involves the chemisorption of water dimers that bridge surface anion vacancies. We suggest that the dimer may be polarized by the crystal field with the negative side of the [OH^- … H_3O^+] dipole oriented toward the oxygen vacancy. At electron energies below the O 2s threshold, ionization of the lattice site in the vicinity of an adsorption complex can cause emission of the H_3O^+ fragment. At higher energies, ESD of H_3O^+ most likely proceeds by the 2-hole 1-electron states of water [73].

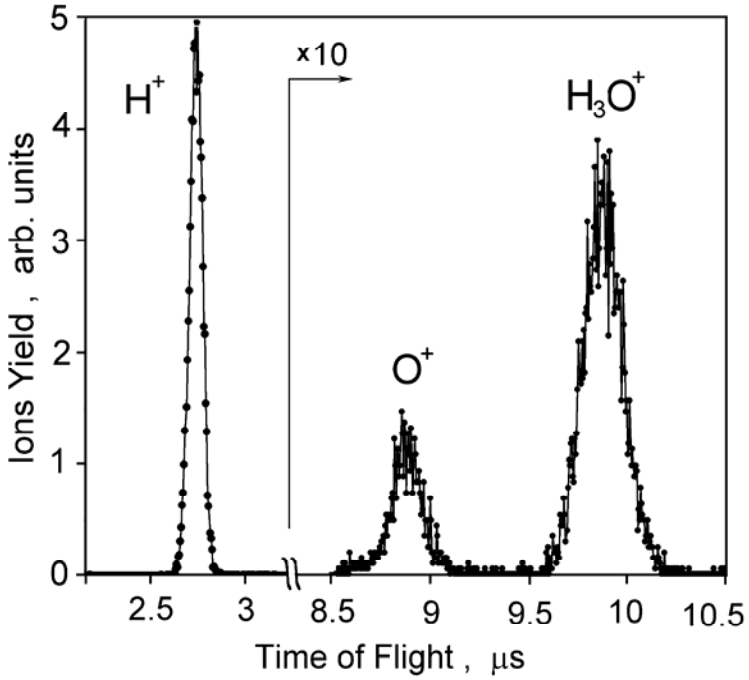

Figure 3.3 Typical TOF-ESD spectrum of ions emitted from GDC surface under the irradiation of 400 eV electrons. Note the yield of H^+ is considerably higher than the yield of all other cation products. The mass assignments were also confirmed with a quadrupole mass spectrometer.

3.4.3 Effect of positive potentials

Although the masses of the ionic ESD products differ, they all have non-thermal kinetic energy distributions. The kinetic energy of an emitted ion often yields direct information concerning its formation mechanism. However, the energy of an ion at the point of its detection can differ from the energy at the point of its emission. Both the extraction potential applied to the detecting device and the surface potential induced by incident electrons can be integrated into the experimentally measured kinetic energy. The influence of extraction potential on ion energy can be evaluated experimentally. However, it is more complicated to assess the influence of surface potentials originating from the differentials between the fluxes of primary electrons, low-energy secondary electron emission, backscattered electrons, and electrons conducted through the sample to/from ground.

To investigate the influence of electron-induced surface potentials on the ESD of ions, constant external (positive and negative) potentials were applied to the sample during irradiation while TOF-ESD spectra were recorded. The kinetic energy distributions of H_3O^+ as a function of applied positive potentials are presented in Figure 3.4. The sample potential dramatically changes the peak positions, and the peak kinetic energy depends linearly on the potential. The half-widths of the peaks increased with sample potential, probably indicating elevated heterogeneous charging caused by the larger sample bias. When a positive sample potential was applied to the back plate, transport of holes to the surface can be enhanced. The inhomogeneous positive charge built up at different sites can then reach a higher level at a larger bias, and can cause broadening of the kinetic energy distributions of desorbing cations. The ion yields approximately doubled when the sample potential was increased from 0 V to +2 V. Since

hole localization is always involved in the emission of cations, this yield increase may suggest that the holes can be trapped in shallow potential wells of surface states. The positive external electric field can suppress the diffusion of holes into the bulk and therefore can increase the number of holes on the surface that can induce ion emission. Similar data regarding the application of a positive potential was observed for H^+ ESD.

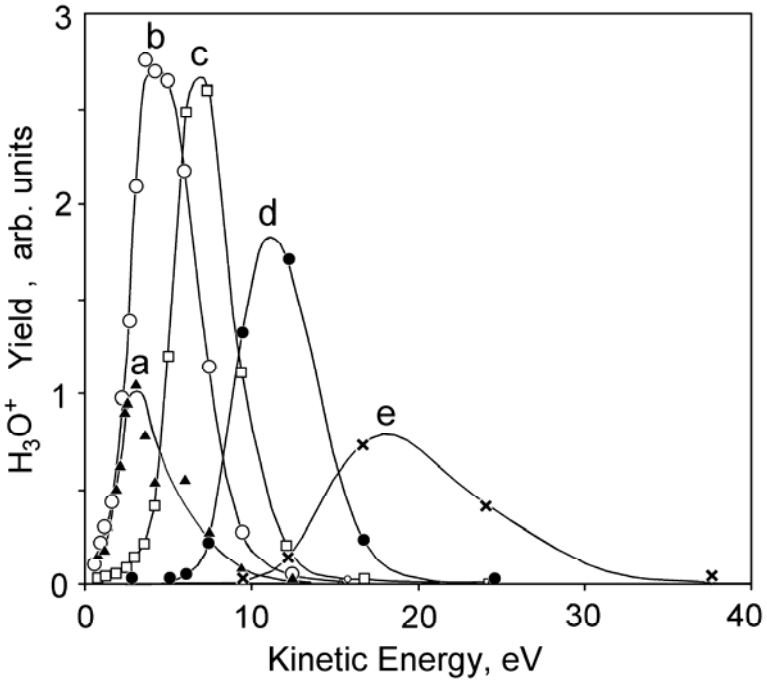

Figure 3.4 Kinetic energy distributions of H_3O^+ as a function of different applied external positive potentials. The incident electron energy was 400 eV, and the electron beam pulse length was 10 μs. Applied external potentials were: (a) 0 V; (b) 2 V; (c) 4 V; (d) 8 V; (e) 16 V.

Surface potentials induced by the incident electron beam are expected to influence the kinetic energies of the emitted ions. For GDC, the average surface potential resulting from pulsed irradiation of 400 eV electrons was found to be positive. The influence of the electron flux on the H_3O^+ kinetic energy distributions and ESD yields is presented in

Figure 3.5. The higher the electron flux, the higher the ion kinetic energy, and the higher the positive charge accumulation. When the electron flux was increased from 4×10^{12} electrons/cm^2·s to 3×10^{14} electrons/cm^2·s, the change of surface potential caused by electron bombardment was estimated to be ~ +3 V. The linear dependence of H_3O^+ yields on electron flux indicates that H_3O^+ is formed by a single direct impact ionization process.

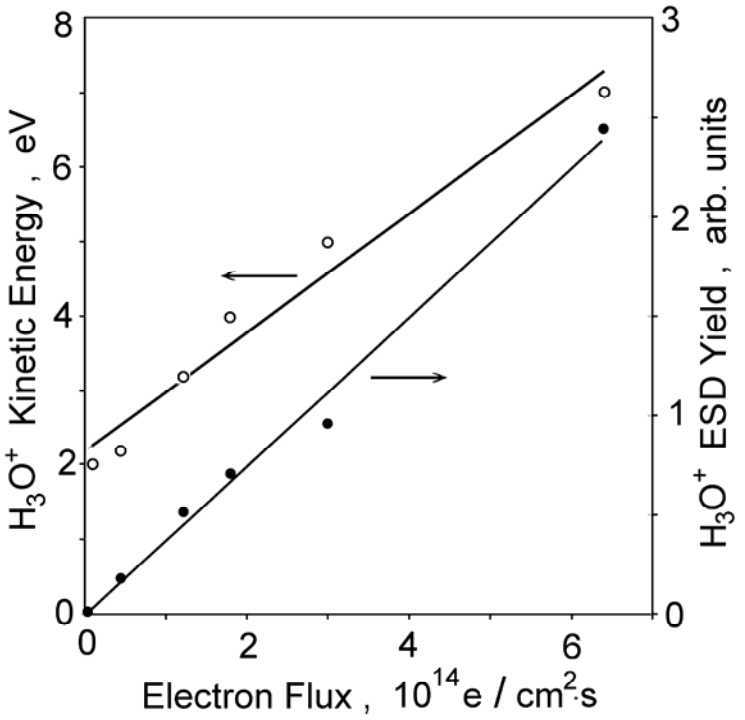

Figure 3.5 Influence of electron flux on the peak kinetic energy and ESD yield of H_3O^+ The incident electron energy was 400 eV, and the electron beam pulse length was 10 μs.

The positive charging of the GDC suggested the trapping of holes. In principle, holes should be trapped at sites with negative effective charge. For GDC, the most probable hole-traps would be close to Gd^{3+}, and the most probable form would be O^-. Another possible form may be O_2^- at the anion site. Electron spin resonance (ESR) experiments on the hole trapping in Al_2O_3 and ZrO_2 showed that the hole-induced charge

has a diamagnetic character. The charge was therefore believed to be related to metal ions or to protons resulting from the interaction of the hole with metal-hydrogen bonds [74,75]. Metal ions or protons may be other forms of hole trapping in GDC.

3.4.4 Effect of negative potentials

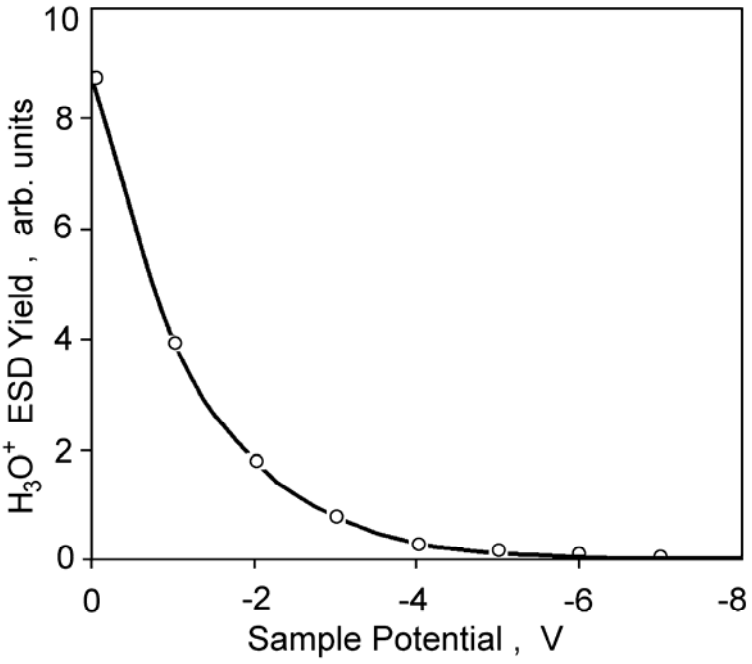

Figure 3.6 Influence of negative sample potential on the H_3O^+ ion yield. The incident electron energy was 400 eV and the electron beam pulse length was 10 μs. Note 99% of the H_3O^+ yield is suppressed with the application of ~ -6 V external potential.

Application of negative potentials to the sample under irradiation of 400 eV electrons caused significant decreases in the ion yields, as demonstrated in Figure 3.6. The H_3O^+ yields decrease exponentially with the sample potential, indicating recapture or neutralization by the surface. Using no extraction field, with a -6 V applied sample potential, 99% of the ions were recaptured. Similar data were also obtained for H^+.

Application of negative potentials also caused the flight time of ions to increase, as is shown for H^+ in Fig. 7. The apparent peak kinetic energy of H^+, expressed as the inverse of the square of the peak flight time, depends linearly on the applied negative potential. With -100 V extraction potential applied to the TOF entrance grid, 99% of the ions were recaptured when the applied negative potential was -30 V.

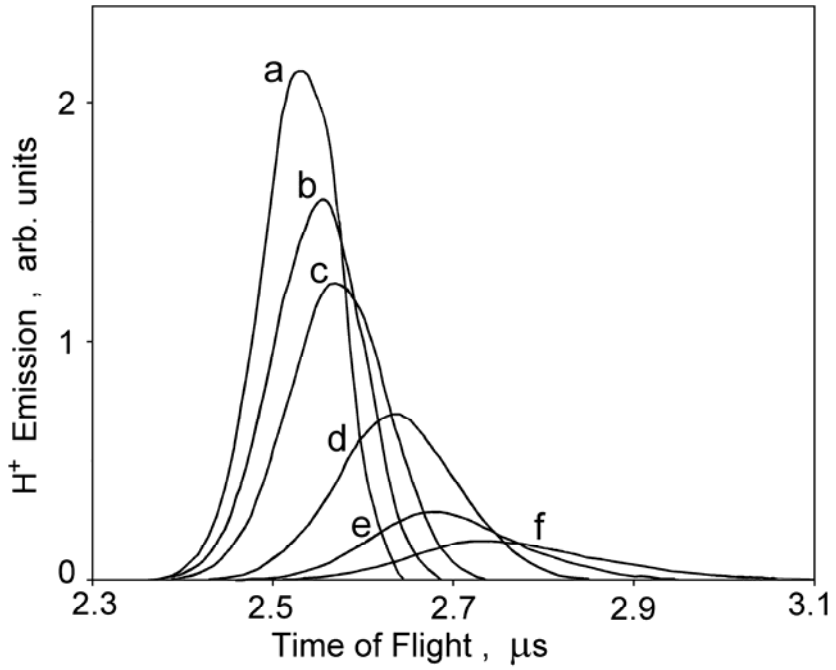

Figure 3.7 Influence of an externally applied negative potential on the TOF spectra of H^+. The incident electron energy was 400 eV, the electron beam pulse length was 300 ns, and the extraction field was -100 V. The external potentials were: (a) 0 V; (b) -2 V; (c) -4 V; (d) -10 V; (e) -15 V; (f) -20 V.

Electrons with an incident energy of 75 eV were chosen to further investigate the negative surface potential caused by electron bombardment. Electrons of lower energies are reflected significantly by the built-up negative charge and are retarded in the potential field of the surface. Irradiation with electrons of higher energies is less efficient in

charging the sample negatively because of increased emission of secondary electrons. The sample was pretreated with 200 eV electrons irradiation to insure that the surface is not initially negatively charged. After this pretreatment, the sample was subjected to irradiation of 75 eV electrons, and the TOF spectra were obtained periodically. In order to enhance the detection sensitivity, a -100 V extraction potential was applied to the entrance grid of the TOF mass spectrometer immediately after the 75 eV electron beam pulse.

The variation of the normalized ion yields versus total number of 75 eV electrons incident on the surface is presented in Figure 3.8. This shows three distinct features of the ion yield dependence on the total number of electrons deposited. The first is a relatively slow monotonic decrease of the ion yield with increasing electron dose until the total dose reached 1.2×10^{15} electrons/cm^2. During this process, the total drop of the ion yields is less than 50% for both H^+ and H_3O^+. The second feature is a drastic drop of ion yields when the electron dose was increased from 1.2×10^{15} electrons/cm^2 to 1.36×10^{15} electrons/cm^2. The last feature shows that 99.9% of ion emission is suppressed after the total dose of electrons is greater than 1.36×10^{15} electrons/cm^2.

The first feature can be explained by a charge neutralization process. Before the 75 eV electrons were deposited, the surface is positively charged due to the pretreatment with 200 eV electrons. With the deposition of 75 eV electrons, the peak flight time of the ions was increased (or the kinetic energy was decreased), indicating a decreased surface potential and therefore a decrease in the number of positive charges on the surface. If the surface is not positively charged during this stage, and if the negative charge build-up is a linear process, the ion yields should drop exponentially with the electron dose, which was

not observed experimentally. For longer pretreatment time, higher doses of 75 eV electrons are required to cause ~ 50% drop in the ESD ion yields, as is consistent with neutralization of an initial positive charge. The different influence of charge build-up on the ion yields of H^+ and H_3O^+ might be associated with the different mechanisms of ion formation at different emission sites.

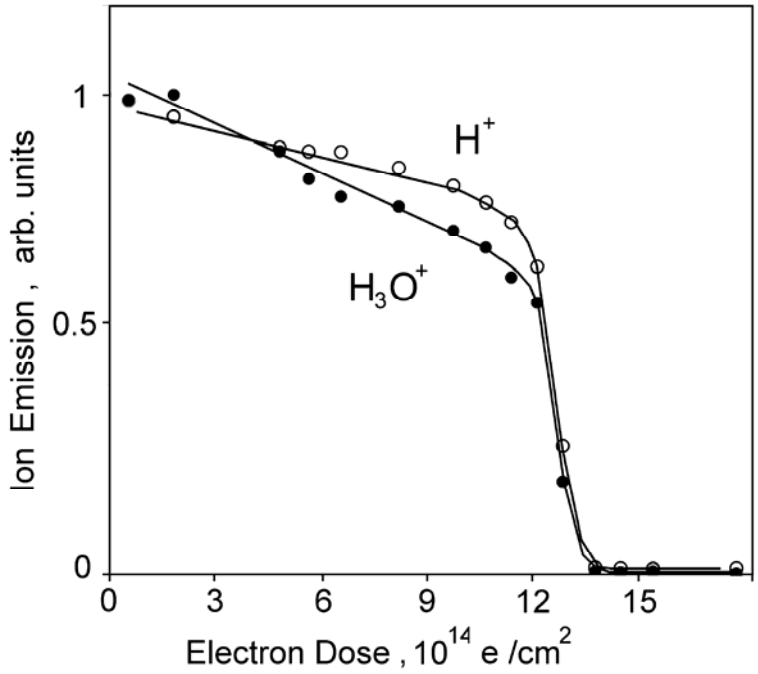

Figure 3.8 The dependence of normalized ion yield on electron dose. The incident electron energy was 75 eV; the electron beam pulse length was 300 ns; and the extraction field was -100 V. The significant decrease of ion yield implies the trapping of electrons by GDC.

The sudden drop off of figure 8 is caused mainly by the recapture of the emitted ions by a 75 eV electron beam induced negative surface potential field. The ion yield doesn't drop exponentially with the electron dose, possibly because of a non-linear

charge build-up process as well as the back-scattering of 75 eV electrons by the negative potential. A 99% drop in ion yields means that 75 eV electrons can charge the surface to such a level that the ion emission is actually quenched. The ion emission quenching is sustained as long as the 75 eV electrons are deposited to the GDC surface. After the ion emission was quenched, the intensity and peak flight time of the ESD ion signal could be restored completely by bombarding the GDC surface with 200 eV electrons. This observation indicates that the type and amount of charge on GDC surface could be manipulated by bombardment with electrons with different energies.

When the incident electron energy was 400 eV and no extracting potential was used, application of a ~ -6V negative potential to GDC sample completely suppressed the ESD of H_3O^+ (Fig. 6). Since the ion emission was quenched by the irradiation with 75 eV electrons, it means that the surface was charged to at least -6 V during the pulse of the electrons. Simple calculations show that the number of electrons reaching the surface during the period of a single pulse is high enough to cause local surface charging up to several volts in the area of the electron beam. Average spreading of the primary electrons inside a crystal during the inelastic scattering and thermalization to the Debye temperature (10-30 meV) occurs within ~10^{-12} s and doesn't exceed 50-100 nm. The migration of the thermalized free electrons has a diffusive character due to elastic scattering by optical phonons. Assuming that the mean free path of the electron is close to the one observed for alkali halide crystals, i.e. about 1-3 nm [76], the average mean-square shift of the scattered electrons between pulses (10^{-3} s) is evaluated to be 10^{-4} – 10^{-3} m, not far from the thickness of the sample. The potential field generated by the electron pulse that followed can repel the free electrons to ground. However, due to the presence of

abundant different types of structural defects in GDC, thermalized electrons could be in traps with different depths. Electrons trapped by a deep potential well can not be driven to ground and can thus form a long-lived negative charge inside the sample.

3.4.5 Role of defects

Negative surface charging of various materials, such as ice [77], plastics bombarded with low energy electrons (0.1-28 eV) [78], single crystal oxides bombarded by 30 keV electron beam [79], and thin layers of oxides on dielectric substrates [80] have been observed. When there are no surface defects, secondary electrons are able to be emitted from the bulk of the sample to the vacuum, reducing the trapping yield even to zero. When a defective layer exists at the surface of the sample, it acts as a barrier against the outgoing secondary electrons. Some of the secondary electrons are trapped beneath the surface, at the interface between the defective layer and the bulk. The probability of trapping free electrons can be very high for GDC, a low conductivity oxide with a highly defective surface area. Molecular dynamics simulation of gadolinia-doped ceria predicted the segregation of gadolinium and the association of oxygen vacancies with gadolinium [81]. This segregation effect at grain boundaries in $Gd_{0.2}Ce_{0.8}O_{2-x}$ was indeed observed and was characterized by a combination of Z-contrast imaging and electron energy loss spectroscopy (EELS) [71]. The composition profile obtained by EELS spectra showed that there is an excess of Gd and oxygen vacancies in the grain boundary core. The gadolinium segregated to the grain boundary partially compensates for the oxygen vacancies, but the level for segregation is insufficient to charge balance the vacancies.

Because the oxygen vacancies have positive effective charges, vacancy rich grain boundaries can serve as very efficient electron traps and charge the sample negatively. The sites close to Gd^{3+}, which are also located at grain boundaries, are most probable traps for holes. Therefore we believe the charging effect that we observed occurs primarily at the grain boundaries. Since grain boundaries can trap charge more efficiently, the conduction of electrons or holes by grain and grain boundaries is very different. This difference may be the reason for the observed inhomogeneous charging.

When secondary electron emission surpasses the primary electron dose during higher energy electron irradiation, the sample builds up a positive charge. Each emitted secondary electron should increase the positive surface charge because of the low conductivity of the sample; however, the positive charge can be neutralized by electrons attracted back to the surface. This charge neutralization will ultimately limit the amount of positive charge the sample can accumulate. In contrast to positive charging, negative charging has a natural limit determined by the energy of the primary electron beam. The charging will stop only when the surface potential repels the primary electrons. Another possible reason for the different efficiency of positive and negative sample charging might be different types of radiation induced conductivity – hole-type or electron-type. At low energies we inject excess electrons, but at high energies we produce holes. If their mobilities are very different and they are the main free charge carriers, then efficiency of discharging could be very different.

CHAPTER 4

PROBING WATER INTERACTIONS AND VACANCY PRODUCTION ON GADOLINIA DOPED CERIA SURFACES USING ELECTRON STIMULATED DESORPTION

4.1 Overview

Polycrystalline gadolinia-doped ceria (GDC) surfaces were studied using low-energy (5 – 400 eV) electron stimulated desorption (ESD). H^+, O^+, and H_3O^+ were the primary cationic desorption products with H^+ as the dominant channel. Both H^+ and H_3O^+ have a 22 eV threshold and a yield change around 40 eV. H^+ also has an additional yield change ~ 75 eV. The ESD of O^+ has a threshold ~ 40 eV and a change in yield ~150 eV. The H^+ and H_3O^+ threshold data collectively indicate the presence of hydroxyl groups and chemically adsorbed water molecules on the GDC surfaces. ESD temperature dependence measurements of GDC showed that the interaction of water with surface defect sites, mainly oxygen vacancies, influences the desorption of H^+, O^+, and H_3O^+. The O^+ ESD yield change ~150 eV may indicate bond breaking of Gd-O as an origin of O^+ desorption and the involvement of oxygen vacancies in O^+ desorption. The temperature dependence study of O^+ desorption at 400 eV incident electron energy yielded an activation energy of 0.21 eV for O^+ desorption, which is close to the energy needed for oxygen vacancy production on ceria surfaces. This may indicate a correlation between the O^+ ESD yield and oxygen vacancy density on GDC surfaces and a potential

correlation of O^+ ESD yield and GDC ionic conductivity. Most of the information in this chapter has been published in the Journal of Physical Chemistry B: 109 (2005) 11257.

4.2 Background

Solid oxide fuel cells (SOFCs) are highly efficient and environmentally benign energy conversion devices,[36,46,63,65,66] and polycrystalline $Ce_{0.9}Gd_{0.1}O_{2-\delta}$ (GDC) is considered to be one of the most promising electrolytes for low-temperatures (500 – 600 ºC) SOFCs. GDC has been used as the electrolyte for low-temperature SOFCs, and as part of composite electrodes to facilitate ionic conduction within the electrodes. To understand the mechanisms of defect mediated ion conduction and reactions at a fundamental level, it is critical to understand the GDC surface defects which play significant roles in these processes.

Gadolinia-doped ceria has the fluorite structure of CeO_2 with gadolinium atoms occupying a fraction of cerium lattice sites. Therefore, the knowledge of the structural and electronic characteristics of CeO_2 surfaces is relevant to that of GDC. For low index surfaces of CeO_2, CeO_2 (111) is the most stable. Upon annealing to high temperature, CeO_2 (110) and CeO_2 (001) form CeO_2 (111) faceted surfaces.[82] On the CeO_2 (111) surface, clustering of oxygen vacancies was theoretically predicted and experimentally verified.[72] In CeO_2, all four valence electrons of cerium, $6s^2 5d^1 4f^1$, nominally leave the host atoms and transfer into the p bands of the oxygen atoms, while in Ce_2O_3, the Ce 4f electrons are fully localized. According to theory, it requires 4.55 eV to form an oxygen vacancy in pure CeO_2 and only 0.26 eV if vacancy production occurs next to a pair of Ce^{3+} atoms embedded into the CeO_2 matrix.[83] The oxygen vacancy formation process is

facilitated by a simultaneous transfer of two electrons into the localized f-level traps on two cerium atoms, which therefore change their valence from 4+ to 3+. The localization and delocalization of Ce 4f electrons are involved in the formation and migration of vacancies. Oxygen vacancy pairs, probably important for O_2 uptake and release, are evidently easier to form on the CeO_2 (111) surfaces.

Similarly, for gadolinia-doped-ceria, molecular dynamics simulation showed that Gd ions are apt to form a Gd^{3+}– vacancy – Gd^{3+} cluster. Cerium ions are apt not to be adjacent to a vacancy.[81] This segregation effect in $Ce_{0.8}Gd_{0.2}O_{2-\delta}$ was observed and characterized by a combination of Z-contrast imaging and electron energy loss spectroscopy (EELS).[71] The composition profile obtained by EELS showed an excess of oxygen vacancies and gadolinium ions in the grain boundary core. This structural feature determines the importance of GDC grain boundaries in ionic conduction as well as in surface and interface reactions. Indeed, it has been found that the smaller the grain size, the higher the grain boundary electrical conductivity.[84]

Less work has been reported concerning surface reactions on GDC. Thus far, only the oxygen surface exchange reaction has been investigated using isotope exchange depth profiling (IEDP) via secondary ion mass spectrometry (SIMS).[57,67,59] With IEDP-SIMS, the activation energy for the oxygen surface exchange reaction was found to be temperature dependent, around 1 eV for temperatures below 650 or 700 °C and 2.4 ~ 3.3 eV at higher temperatures. The mechanisms leading to this temperature dependence are yet to be understood at an electronic level by other surface specific techniques.

Electron stimulated desorption (ESD) is a surface analysis technique that can probe adsorbates and their interaction with the surface through the characterization of

desorbed ionic or neutral species.[13,25] The threshold energy for producing desorbed species as well as their kinetic energy distributions are of importance in identifying the specific site of desorption. Since defects or local disorder on a surface may act as the trapping sites of electronic excitations, they can serve as preferential sites for desorption. Therefore, ESD can yield direct information regarding defects and their role in surface reactions critical to the electrochemical performances of SOFCs.

In order to explain the ESD of cations from metal oxides, Knotek and Feibelman (K-F) proposed a model based on an inter-atomic Auger neutralization of a hole produced in the core level of the surface atom.[23] The inter-atomic Auger decay of the core hole creates a positive ion at an initially negative ion site, and the expulsion of the positive ion results from the reversal of the Madelung potential. A more generalized Auger-stimulated desorption model has extended the K-F model to less ionic and covalent systems.[85]

In this chapter, we present a comprehensive study of electron stimulated desorption of cations from polycrystalline gadolinia-doped ceria surfaces. Section 4.3 describes the experimental approaches. The results include threshold and temperature dependencies of ESD cation yields and are presented in Section 4.4. Details of the ESD mechanisms, the importance of water interactions with the surface, and the significance of correlations between O^+ ESD and vacancy formation are discussed in Section 4.5.

4.3 Experimental details

4.3.1 Sample preparation and characterization

The $Ce_{0.9}Gd_{0.1}O_{2-\delta}$ (GDC) powder was prepared using a glycine-nitrate process as described elsewhere.[46] The GDC pellet used in this experiment was cold pressed from the powder and then fired at 1550 °C for 5 hours in air to achieve a greater than 95% relative density. The dimensions of the GDC pellet were about 10×6×1 mm. X-ray diffraction (XRD, PW-1800 system, with Cu-Kα radiation operated at 40 kV and 30 mA,) and scanning electron microscopy (SEM, Hitachi S-800) studies were performed on sintered GDC pellets. As shown in Figure 4.1, typical XRD patterns of a GDC sample indicate that GDC has a single-phase fluorite structure. The SEM images of the surface morphology of an as-sintered GDC sample show that grain size varies from 1 to 5 μm, and the sample has a significant number of grain boundaries.

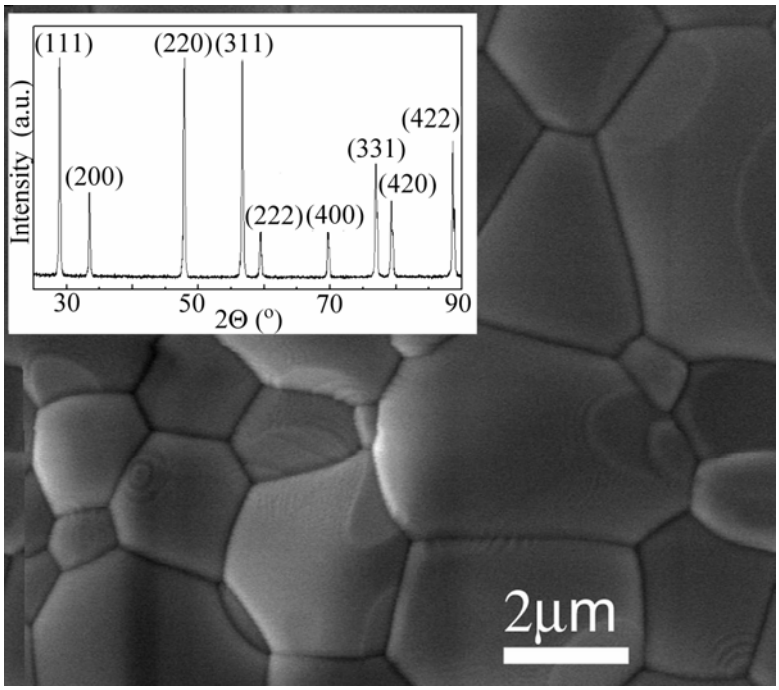

Figure 4.1 The SEM image of the GDC surface morphology. The inset is the XRD pattern of a sintered GDC pellet, indicating a fluorite structure. Note the defective grain boundaries and triple junctions on the surface.

4.3.2 Electron stimulated desorption (ESD)

Details of the ESD measurement system have been discussed in a previous paper.[86] The system consists of an ultra high vacuum chamber (base pressure 2×10^{-10} torr) equipped with a rotatable sample holder, a computer-controlled button heater, a quadrupole mass spectrometer (QMS), a time-of-flight (TOF) mass spectrometer, a pulsed low-energy electron gun, and a calibrated dosing system.

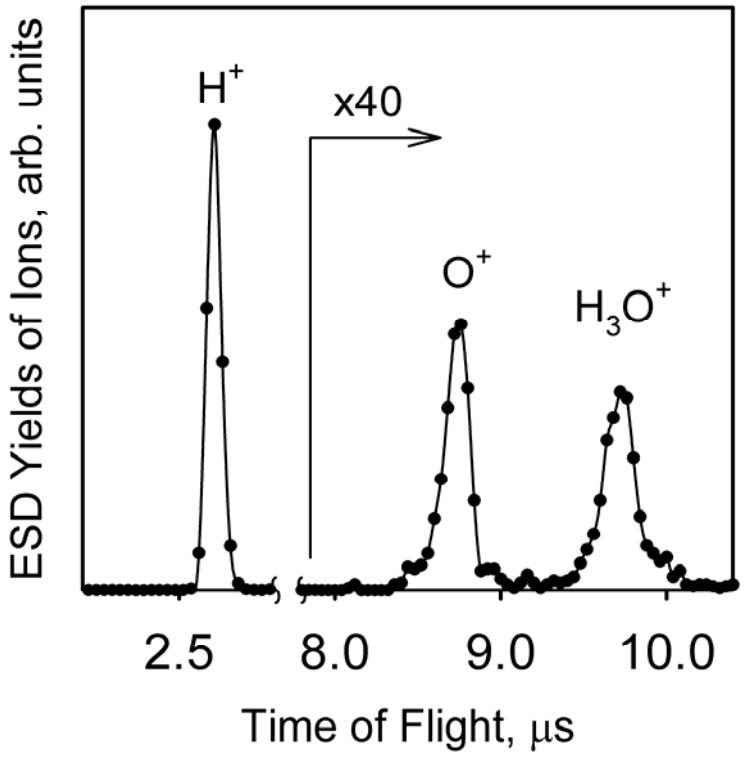

Figure 4.2 Typical TOF-ESD spectrum of ions emitted from a GDC surface during pulsed 400 eV electron irradiation. The H^+ yield is significantly larger than the O^+ and H_3O^+ yields.

The GDC sample was annealed to 400 ºC to remove all contaminants from the surface. The sample was irradiated by the pulsed electron beam at 1000 Hz with an electron flux of 10^{14} electrons/cm^{2}s during a given pulse or time-averaged currents of 200

pico-Ampere to a few nano-Ampere. Emitted cations were collected by applying a -100 V pulsed extraction potential to the TOF front lens assembly just after the end of the electron pulse to avoid the influence of the potential field on the incident electron energy. A typical time-of-flight spectrum of cation ESD is displayed in Figure 4.2, showing H^+, O^+, and H_3O^+ desorptions. No other ions were observed, indicating the cleanliness of the surface. For ESD temperature dependence measurements, the QMS (with its ionizer turned off) was employed as the mass analyzer. All ions were detected using pulse counting and a transient digitizer.

In our previous ESD study on GDC [86], it was found that the ESD ion yields were dependent on the electron beam induced surface charging. At higher electron energy, the surface was positively charged. For lower energies, the charge build-up was negative and the ion yields dropped exponentially with the negative surface potential. To avoid this dramatic influence of negative surface charging on ion yields, two special experimental procedures were undertaken: 1). A short electron pulse length (500 ns) and a short time for signal averaging were employed. 2). To insure the surface was not negatively charge, the sample was irradiated with a 400 eV pulsed electron beam for 60 s. Three ESD-TOF spectra were taken at each electron energy and the average yield was used for threshold measurements. The yields were normalized to the electron beam current at different energies.

4.4 Results and Discussion

4.4.1 Energy dependence of cation ESD yields

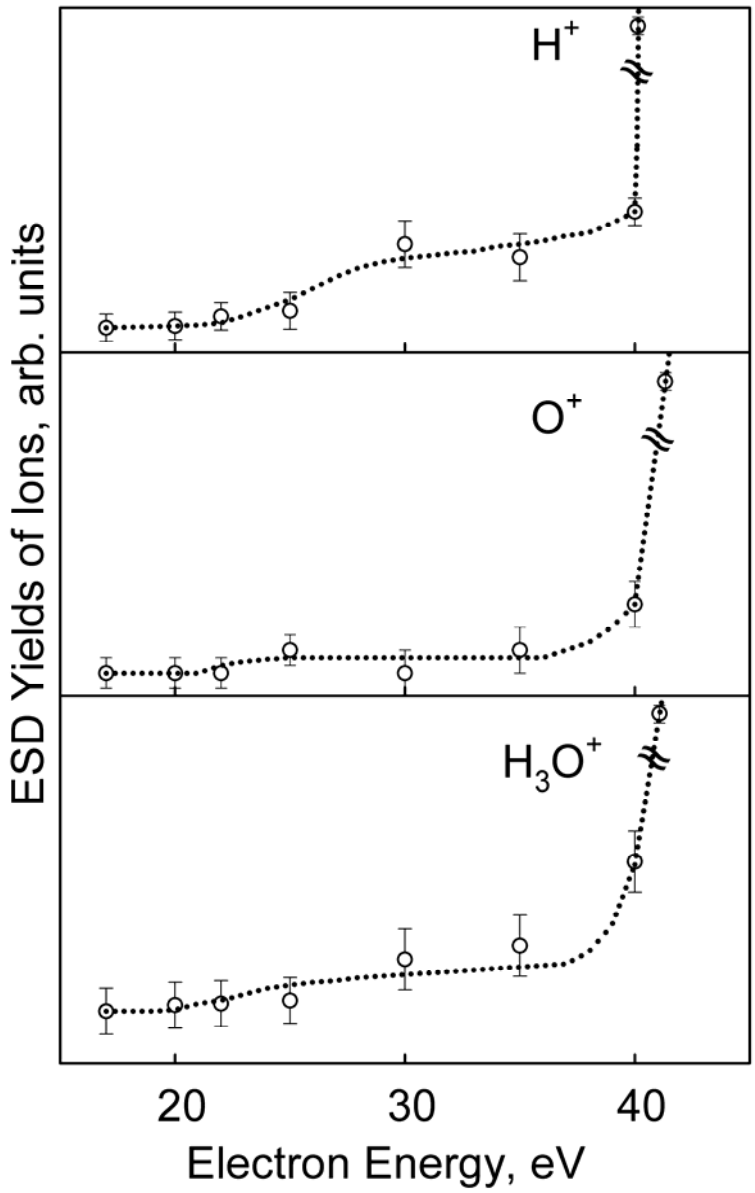

Figure 4.3 The dependence of ESD cation yields on incident electron energy in the range of 0 to 50 eV. The pulse length was 500 ns and the sample was at room temperature. Note the threshold at 22 eV for H^+ and H_3O^+ and around 40 eV for O^+.

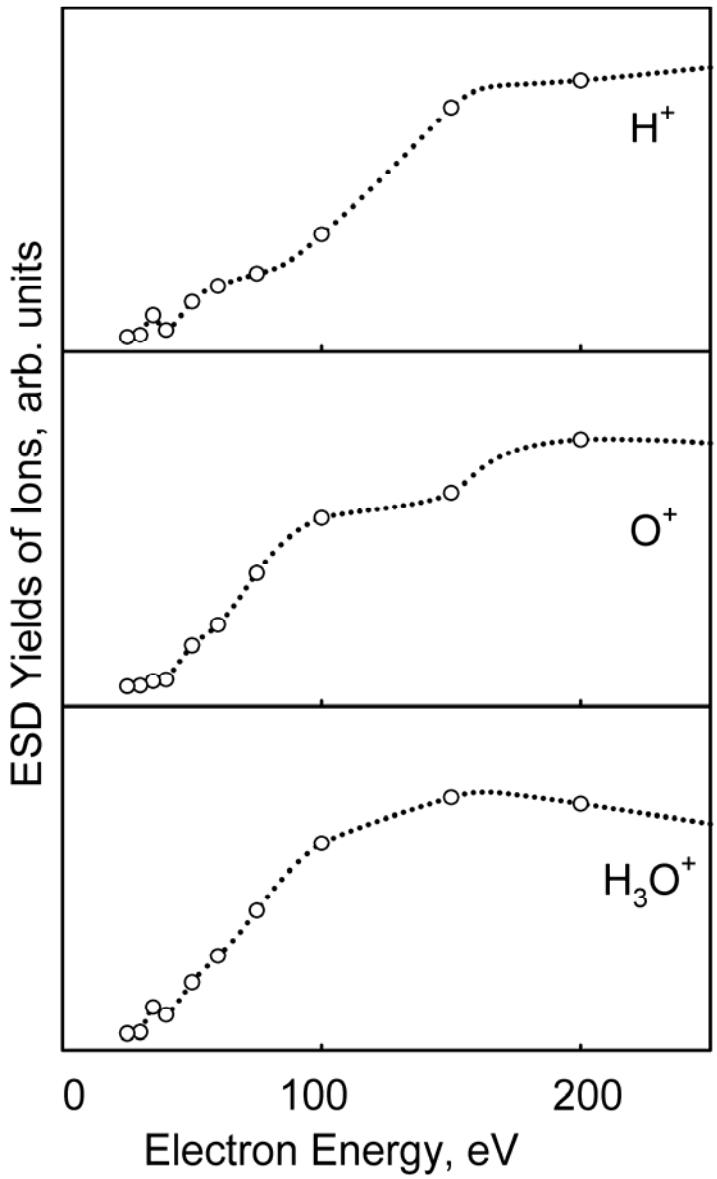

Figure 4.4 The dependence of ESD cation yields on incident electron energy. The pulse length was 500 ns and the sample was at room temperature. Note the yield change around 75 eV for H^+ and 150 eV for O^+.

Figure 4.3 and Figure 4.4 show the dependence of H^+, O^+ and H_3O^+ ESD from polycrystalline GDC on incident electron energy at room temperature. For H^+ and H_3O^+,

there is a threshold at 22 eV, followed by a yield change around 40 eV. Different from H_3O^+, the H^+ has another yield change around 75 eV. For O^+, however, the 22 eV onset is very weak compared to the 40 eV yield change, and there is an additional yield change around 150 eV. Though the dependence of the ESD yields on electron energies of these three cations share certain thresholds, each ion depends on electron energy differently. This suggests that on GDC surfaces, the sites and species contributing to positive ion desorption are basically different.

4.4.2 Electronic structure of GDC

Knowledge of the electronic structure of GDC is important for the understanding of electron stimulated cation desorption. Unfortunately, there is only one X-ray photoelectron spectroscopic (XPS) survey scan of gadolinia-doped ceria (GDC) thin films available in the literature.[87] There are, however, studies on the electronic structure of cerium and gadolinium oxides. In the energy range we are interested in, an XPS study of Gd_2O_3 powder found the binding energies of 9.4, 23.0, 46.2, 142.5, and 147.9 eV for 4f, 5p, 5s, $4d_{5/2}$, and $4d_{3/2}$ gadolinium core levels respectively.[88] The binding energy for the O 2s level was found to be 27 eV. An ultraviolet photoelectron spectroscopy (UPS) study of the gadolinium oxidation process showed that the O 2p valence band and O 2s core level for Gd_2O_3 were located at ~ 6 eV and ~ 23.5 eV, respectively.[89] The band gap of crystalline Gd_2O_3 is 5.3 eV according to Emeline et. al..[90]

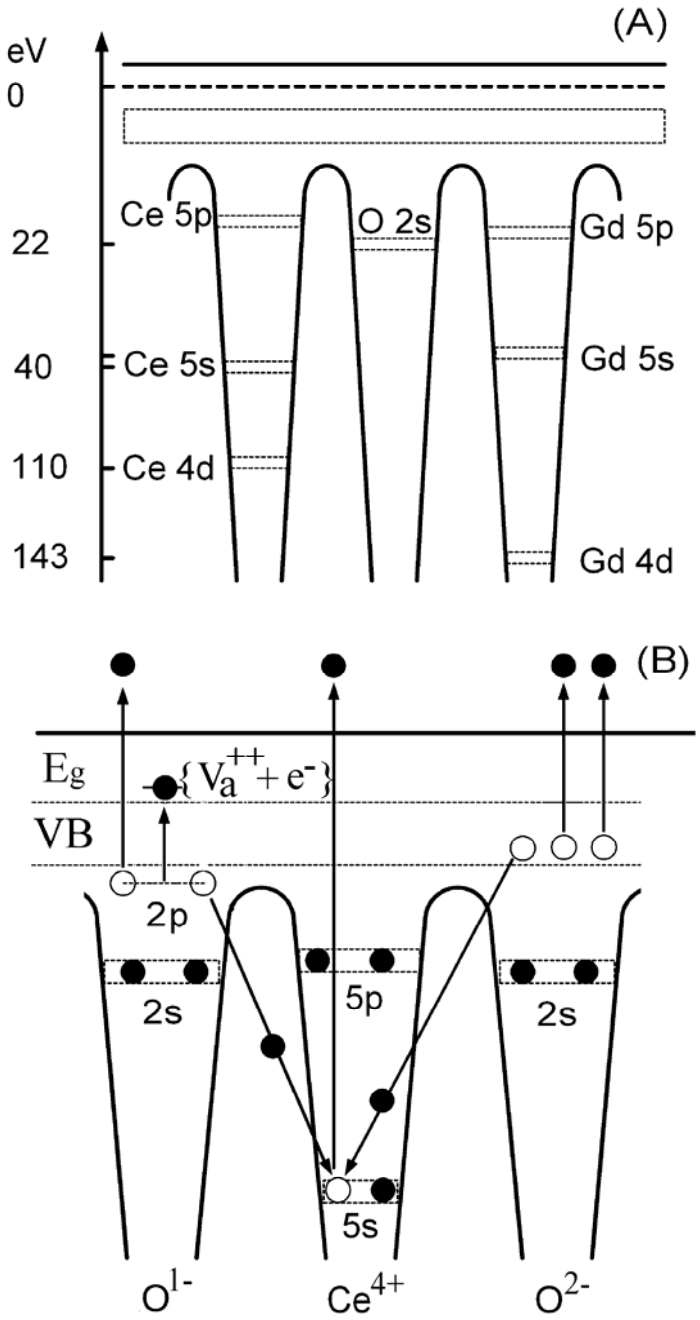

Figure 4.5 (A) Energy diagram of the core levels of cerium, gadolinium, and oxygen. The valance band level and band gap energy are unknown for GDC. (B) Illustration of inter-atomic Auger decay K-F desorption mechanism for O^+ desorption. Shown is the Ce 5s core hole production and subsequent Auger electron emission from O 2p level in the valence band. In the presence of anion vacancy V_a^{++}, the effective charge on oxygen can be lower than 2 the desorption from these sites are more efficient.

For CeO_2, the binding energies for Ce $5p_{3/2}$, 5s, $4d_{5/2}$ core levels are 18.0, 36.8, 108.5 eV, respectively, and O 2p is ~ 5 eV.[91] There is no O 2s binding energy for CeO_2 available, but the O 2s level for $CeNbO_4$ is 21.8 eV. CeO_2 has a band gap of 6 eV.[91] Figure 4.5 (A) is an energy diagram of the core levels of cerium, gadolinium, and oxygen in the energy range of this study, constructed by using the binding energies data of CeO_2 and Gd_2O_3. Neither the band gap nor the energy level of valence band of GDC is available.

4.4.3 Threshold values and ESD mechanisms

4.4.3.1 Desorption of H^+

On cerium oxide surfaces, hydrogen atoms may be bonded to the surface in two different ways. The first is as hydroxyl groups which are most likely bonded to cerium cations. Soft X-ray photoemission spectroscopy and thermal desorption spectroscopy studies showed that on reduced cerium oxide surfaces, water dissociates and forms hydroxyl. The hydroxyl group formation is found to be related to Ce^{3+} instead of Ce^{4+}. On GDC surfaces, because of the presence of oxygen vacancies, a fraction of cerium atoms existing in +3 oxidation states can lead to the formation of Ce-O-H on the surface. Similarly, hydroxyl groups can also bond to gadolinium atoms forming Gd-O-H. The second form of hydrogen can be from chemically adsorbed water, as has been demonstrated on fully oxidized CeO_2 surfaces by soft X-ray photoemission spectroscopy below 300 K.[92]

In general, desorption of positive ions from surfaces under electron irradiation involves the electronic excitation of the substrate or adsorbate core levels. Direct electronic excitation can also generate holes in the covalent bond of surface species, for example, on the σ-bond of the surface hydroxyl group. The core holes can decay through many different mechanisms. One radiationless decay channel is Auger decay, through which at least two electrons can be removed from the system, leaving two localized holes in the valence band. For metal oxides, the holes are localized on oxygen atoms. Two holes localized on an oxygen atom can reverse the Madelung potential so that the oxygen can be removed as neutral atomic oxygen or O^+. The Auger decay can also result in two holes on the σ-bond of a hydroxyl group, and the subsequent Coulomb repulsion can lead to the desorption of H^+.

From the energy diagram, the binding energies of O 2s (21.8-23.5 eV), Ce 5p (18 eV), and Gd 5p (23 eV) core levels are close to the 22 eV threshold for H^+ desorption. Therefore, H^+ desorption may be associated with the ionization or hole production in these core levels and the presence of surface hydroxyl groups. Ce 5p (18.5 eV) ionization was found to be involved in the ESD[93] and PSD[94] of H^+ from cerium oxides. Gd 5p excitation may contribute to H^+ desorption in a similar way. Because of the overlap of the O 2s level with the Ce 5p or Gd 5p level, it is impossible to distinguish which type of hole contributes most to the H^+ desorption. The 40 eV yield change is very close to the binding energies of Ce 5s (36.8 eV) and Gd 5s (46.2 eV) levels. The inter-atomic Auger decay of the holes generated by electronic excitation at these 5s levels is efficient in producing H^+.

The ESD threshold energies for H^+ desorption from ice are also found to be 22 eV and ~40 eV.[73] The 22 eV threshold was assigned to configurationally mixed 2-hole 1-electron $(1b_1)^{-2}(4a_1)^1$ and $(3a_1)^{-1}(1b_1)^{-1}(4a_1)^1$ final states of water and the 40 eV threshold was assigned to $(3a_1)^{-2}(4a_1)^1$, $(3a_1)^{-1}(1b2)^{-1}(4a_1)^1$, and $(1b_2)^{-2}(4a1)^1$ states.[95] The yield change around 75 eV, however, is not close to any of the core levels of cerium or gadolinium, but close to the excitation energy for the formation of two-hole state at the $2a_1$ level of water. The combination of H^+ desorption threshold data strongly suggested the presence of water on GDC surface at room temperature.

4.4.3.2 Desorption of O^+

Compared to H^+ desorption, the 22 eV threshold for O^+ desorption is weak, so the contribution from the hole production at O 2s, Ce 5p or Gd 5p levels to O^+ desorption is limited. The yield change around 40 eV is much stronger and can be related to the ionization of Ce 5s or Gd 5s levels. In general, the subsequent inter-atomic Auger decay of the 5s holes, can lead to the production of O^+, as shown in Figure 4.5 (B). However, a single Auger process can only remove two electrons from an oxygen atom. If the oxygen is in O^{2-} oxidation state, then a third electron should be removed from the O 2p valence band in order to obtain O^+. One way to realize the removal of the third electron is through a double Auger process which has low cross section. However, if the involved oxygen anions are located close to oxygen vacancies and have nominal charges less than 2, then O^+ can be formed through a single Auger process. Interestingly, for O^+ desorption, a yield change around 150 eV, which is very close to the Gd 4d level (143 eV), was observed.

This yield change strongly suggests that the O^+ desorption is predominantly from the bond breaking of Gd-O rather than Ce-O. Considering the association of oxygen vacancies with gadolinium atoms in GDC, the O^+ desorption is then closely related to the oxygen vacancies. Since we know that Gd is rich in the grain boundary region of GDC, the dominant desorption sites should be located at the grain boundaries.

4.4.3.3 Desorption of H_3O^+

Unlike the desorption of H^+ and O^+, only a threshold and a yield change were observed for H_3O^+ at 22 and ~ 40 eV, respectively. The mechanism of electron stimulated H_3O^+ desorption from oxides surfaces at room temperature is not yet established. Our model on the ESD of protonated water cluster ions $[H(H_2O)_n]^+$ (n=0~8) from water ice surfaces showed that the process was initiated by positive charge localization on neighboring water molecules networked through hydrogen bonds[73].

At room temperature, water can interact with the oxygen vacancies of metal oxides dissociatively and form hydroxyl groups. Water can also chemically adsorb to the surfaces. Although no water network is observed on oxide surfaces at the room temperature, the presence of a second layer water at a sub-monolayer coverage on reduced CeO_2 (111) surface has been confirmed by Henderson et. al. using temperature programmed desorption (TPD)[96]. We therefore propose that on GDC surfaces the first layer of water molecules preferably adsorb to the oxygen vacancy, with one of the hydrogen atoms of water oriented away from the oxygen vacancy. The O-H bond then is highly polarized by the positive charge of the oxygen vacancy, leading to the adsorption

of the second layer of water on to the first layer with the formation of a hydrogen bond like interaction between the oxygen atom of water from the second layer and the polarized hydrogen atom of the first layer. The formation of [·····$H^{\delta+}$·····OH_2], very close to the H_3O^+, will then serve as a precursor for H_3O^+ desorption.

Polarization of the O-H bond of water by the vacancies on GDC surfaces means the bond breakage of O-H is facilitated by water interaction with the surfaces. The oxygen atom from the water molecule can be incorporated into the lattice through formation of a hydroxyl group at the vacancy site. This process costs much less energy than the breakage of a O=O double bond. This also means that the surface exchange process should be facilitated by water present in the feed gas. A recent study showed that a small amount of water vapor can enhance the surface oxygen exchange rate on the surface of single crystal yttria-stabilized zirconia (YSZ) up to 1000 times at 873 K.[97] The water interaction with GDC surfaces can also account for the discrepancy of the activation energy for the oxygen surface exchange reaction, i.e., around 1 eV for temperatures below 923 or 973 K and 2.4 ~ 3.3 eV at higher temperatures. At lower temperature, the water interaction with GDC is dominant while at higher temperature oxygen reduction is rate limiting.

4.4.4 Temperature dependence

4.4.4.1 Temperature dependence of H_3O^+

The influence of temperature on the ESD ion yields is presented in Figure 4.6. Under the irradiation of 400 eV electrons, the H_3O^+ data were taken from room temperature to 650 K. When the sample temperature was increased from 300 K to 360 K, the H_3O^+ ESD yields decreased sharply, most probably because of the complete desorption of the adsorbed sub-monolayer of water from the surface. For temperatures higher than 360 K, the H_3O^+ yields continued to decrease and the yields were around the detection limit.

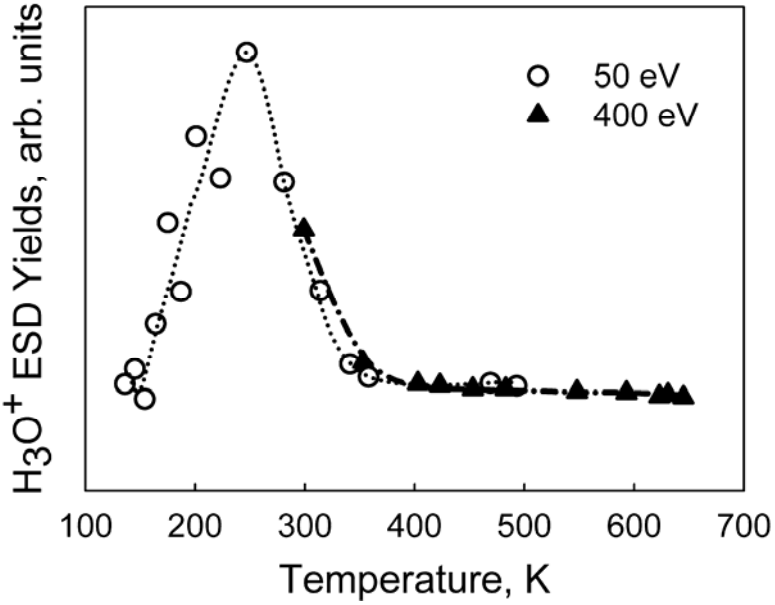

Figure 4.6 The dependence of H_3O^+ ESD ion yields on sample temperature. The incident electron energy was 400 eV with a pulse length of 200 μs and 50 eV with a pulse length of 5 μs. The peak at 250 K indicated the involvement of chemisorbed water in the H_3O^+ desorption.

Under 50 eV electron beam irradiation, the H_3O^+ data were taken after dosing 60 ML of water at liquid nitrogen temperature. In the temperature range from 100 to 550 K,

the H_3O^+ ESD yield was minimum around 150K and maximum around 250 K. A temperature programmed desorption (TPD) study of water from a 500 Å epitaxially grown CeO_2 (111) surface shows peaks between 190 K and 320 K. The TPD spectra depended upon the coverage and the oxidation states of cerium ions or the population of oxygen vacancies. All adsorbed water molecules are desorbed around 400 K regardless of the coverage and surface condition.[96] The 250 K ESD H_3O^+ peak is quite close to the TPD water peak for a water coverage of 0.58 ML on a CeO_2 (111) surface comprised of ~ 33% ML of oxygen vacancies, indicating the involvement of adsorbed sub-monolayer of water in the ESD of H_3O^+. At temperatures higher than 250 K, the H_3O^+ ESD yield drops quickly; and at 360 K, the ESD H_3O^+ yield is only 2% of that at 250 K. This quick drop in ESD yields is primarily due to the water desorption from the surface.

4.4.4.2 Temperature dependence of O^+

Presented in Figure 4.7 is the temperature dependence of O^+ ESD yields. The temperature dependence of O^+ desorption from GDC under the irradiation of 50 eV electron beam was studied in the temperature range of 300 K to 600 K without water dosing. Since the presence of water reduces the O^+ yield, we chose this temperature region to minimize the amount of adsorbed water. When the sample was heated, the ESD O^+ yields first increased, peaked around 360 K, and then decreased. Very different temperature dependence was observed for 400 eV irradiation. Specifically, the yield simply increases monotonically with temperature.

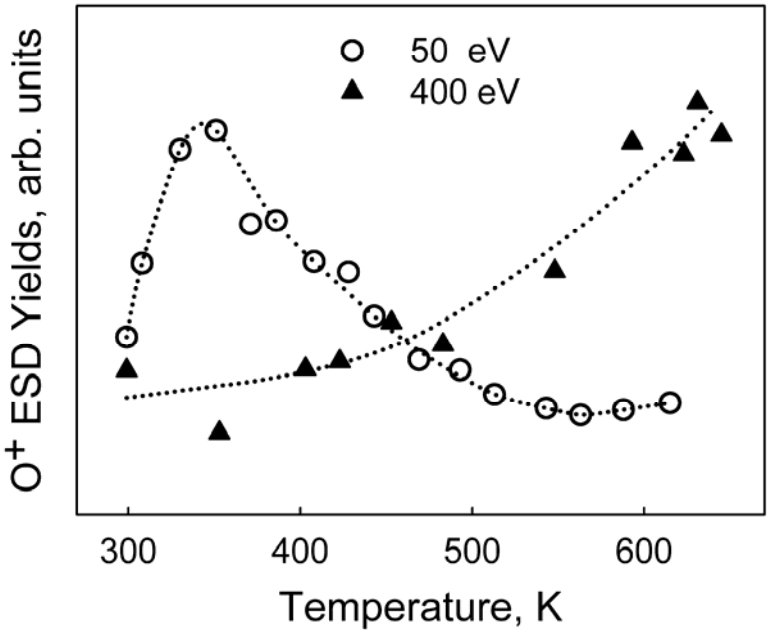

Figure 4.7 The dependence of the O^+ ESD ion yields on sample temperature. The incident electron energy was 400 eV with a pulse length of 200 μs and 50 eV with a pulse length of 5 μs. Note for temperatures greater than 360 K, the O^+ increases with temperature for 400 eV but decreases for 50 eV electron bombardment.

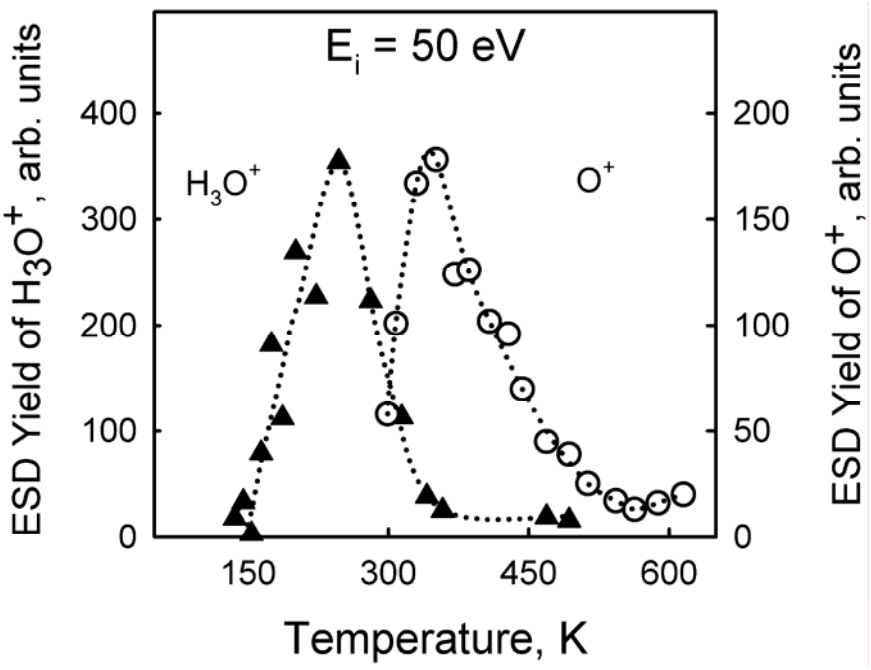

Figure 4.8 The dependence of O^+ and H_3O^+ ESD ion yields on sample temperature. The incident electron energy was 50 eV and the pulse length was 5 μs. The surface was dosed

with ~50 ML of water at liquid nitrogen temperature before the H_3O^+ desorption data was taken but no water was dosed for O^+ data. Note that around 360 K the O^+ yields started to decrease when H_3O^+ yields was below the detection limit.

A comparison of the ESD yields of H_3O^+ and O^+ from GDC surface bombarded by 50 eV electron beam is presented in Figure 4.8. It is interesting to note that the O^+ ESD yield peaked at the same temperature as the disappearance of H_3O^+, i.e., the temperature of total removal of chemisorbed water. This demonstrates, as stated above, that the chemisorbed water can influence the O^+ desorption.

4.4.4.3 Temperature effects

The threshold measurements have demonstrated that O^+ desorption is closely related to the presence of oxygen vacancies. It is therefore very interesting to explore the correlation between O^+ ESD and oxygen vacancy production on GDC surfaces. If we assume that ESD O^+ yield $Y_{ESD\,(O^+)}$ is proportional to the oxygen vacancy density, an Arrhenius plot of the logarithm of $Y_{ESD\,(O^+)}$ against 1/T in the temperature range of 400 to 600 K yielded a linear relationship (See Figure 4.9). The activation energy calculated from this plot is 0.21 eV, close to the 0.26 eV for the production of an oxygen vacancy near two Ce^{3+} in ceria as calculated by first-principles quantum mechanical simulations[83].

According to Kilner et. al.[98], for doped fluorite oxides such as GDC, the vacancies induced by dopant ions are not free but bound to the dopant forming vacancy-dopant pairs. In the temperature range of our experiment, the population of charge carrying defects is determined by the thermodynamic equilibrium between the free defects and the associated vacancy-dopant pairs. The higher the temperature, the more the free oxygen

vacancies are available for ionic conduction. This suggests a potential correlation between the ESD O^+ yields and the ionic conductivity of GDC at low temperature.

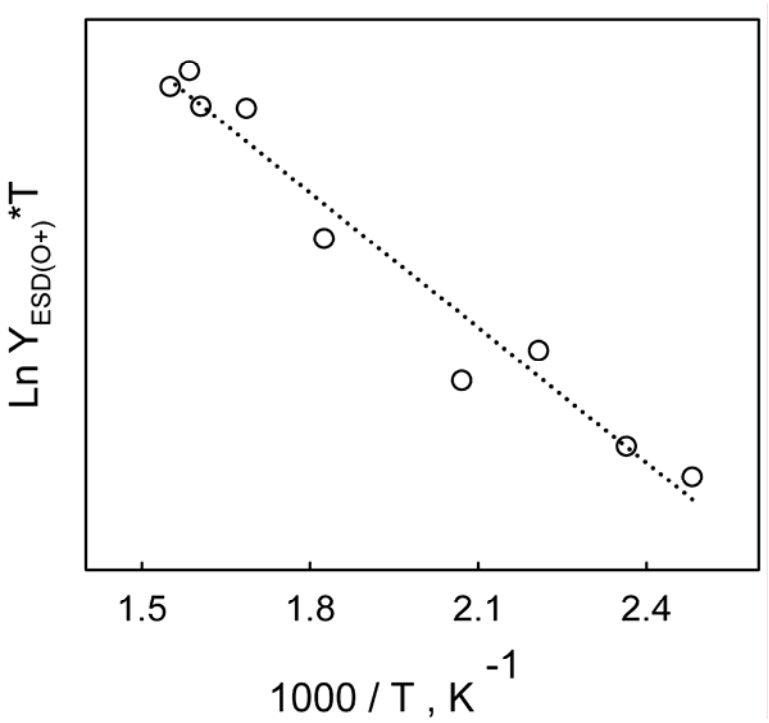

Figure 4.9 Arrhenius plot of ESD O^+ yield at 400 eV in the temperature range of 400 - 600 K. The activation energy for O^+ desorption is 0.21 eV, in agreement with the vacancy formation energy calculated by first-principles quantum mechanical simulation for ceria.

The temperature dependence of O^+ yields under 50 eV electron irradiation is completely different from that of 400 eV electrons. For temperatures greater than 360 K, the monotonic decrease of the ion yields can be understood by charge trapping of the GDC surface. Based on our previous study on GDC, bombardment by 50 eV electrons can charge the surface negatively, and these negative charges on the surface can decrease the cation desorption yields in at least two ways:

1). The existence of the negative potential can increase the re-neutralization and recapture rate of the desorbed ion and decrease the cation yields exponentially.

2). The secondary electrons trapped by oxygen vacancies will subsequently increase the average negative charge on the oxygen anion and then decrease the probability of O^+ desorption resulting from Auger processes.

Therefore, the 50 eV temperature dependence pattern can be understood as a result of two competing trends, the increase of charge trapping with temperature (i.e. with the heating or irradiation time) and the increase of the equilibrium concentration of free oxygen vacancies with temperature. For temperatures below 360 K, because of water adsorption to oxygen vacancy sites, charge build up is not significant compared to the defect density increase caused by temperature elevation. Therefore, the overall O^+ desorption yield increases with temperature. When chemisorbed water is removed, and the charge build up becomes significant, the desorption of O^+ goes down after its peak. In principal, at higher temperature, the GDC has higher electrical conductivity so the secondary electrons should be conducted rather than be trapped. However, within the temperature range of this experiment, the main contribution to conductivity of GDC is from oxygen vacancy diffusion instead of electron or hole migration. In this case, with prolonged electron beam bombardment, enough electrons can be trapped even at higher temperatures to cause the O^+ yields to decrease. The decrease of O^+ yields with temperature also suggests that free oxygen vacancies may trap electrons more efficiently than vacancy associates.

CHAPTER 5

HIHGLY EFFICIENT ELECTRON STIMULATED DESORPTION OF O^+ FROM GADOLINIA-DOPED CERIA SURFACES

5.1 Overview

Highly efficient electron stimulated desorption (ESD) of O^+ from gadolinia-doped ceria surfaces annealed at 850 K in ultrahigh vacuum is observed and investigated. O^+ desorption has a major threshold ~ 40 eV and a most probable intrinsic kinetic energy around 5.6 eV. Since the threshold energy is close to Ce 5s and Gd 5s core levels, Auger decay of core holes is likely associated with O^+ desorption from sites related to oxygen vacancies. The interactions of water and molecular oxygen with GDC surfaces indicate that water and oxygen molecules adsorb mainly to oxygen vacancies, causing the decrease of O^+ desorption. The dependence of O^+ kinetic energies on the incident electron energy and temperature reveals surface charging as a result of electron trapping, hole trapping, and electron-hole recombination. The activation energy for charge transport is found to be 0.43 eV, close to the activation energy of the electrical conduction (0.47 to 0.6 eV) on the same material measured by other methods. The material in this chapter will be submitted for publication in the Journal of Physical Chemistry B.

5.2 Background

Ceria-based metal oxides have been explored as technically important electrolyte and electrode materials for solid oxide fuel cell (SOFC) development.[36,99,100] Among various doped ceria materials, polycrystalline gadolinia-doped ceria (GDC) is widely investigated as a promising electrolyte or a component of electrodes for lowering the operation temperature of SOFCs.[42,46,52,62,101-104] Similar to most mixed oxides, GDC has intrinsic oxygen vacancies. These vacancies play critical roles in electrical conduction and chemical reaction processes occurring at surfaces / interfaces and in electrode and electrolyte materials. In-depth knowledge of the configuration and nature of different oxygen vacancies on the surfaces can further our understanding of the vacancy mediated or assisted surface processes, and thus enable the rational design of smarter materials for improved or optimized fuel cell performance.

Thus far, the direct characterization of defects on the surface of several single crystal metal oxides at the atomic level has been realized by scanning tunneling microcopy (STM)[72,82,105-107] and atomic force microscopy (AFM).[108-113] For example, on the surface of CeO_2, which has the same fluorite structure as GDC, at least three types of surface oxygen vacancies or vacancy clusters (VCs) are observed by both techniques. They are isolated oxygen vacancies, linear surface oxygen vacancy clusters (LSVCs), and surface oxygen vacancy trimers (SVTs). The relative abundance of these defects on the surface is determined by the total number of oxygen ions removed from the surface. Atom-resolved non-contact atomic force microscopy (NC-AFM) study of CeO_2 (111)[111] shows that the oxygen vacancy density on a nearly stoichiometric surface is $(0.8 – 1.7) \times 10^{12}$ cm^{-2}. Before 2% of the top layer of oxygen ions is removed, isolated oxygen vacancies dominate the surface. Linear oxygen vacancy clusters and triangular clusters

are formed and become dominant when 2.1-4.6% of the top layer is removed. In other words, vacancy clusters are dominant at high defect density. Line defects are the major multiple defects on highly reduced CeO_2 (111) and triangular clusters are rarely observed. Oxygen atom hopping was seen by NC – AFM at room temperature[119] by not observed by STM even at 300 to 400 °C.[106]

The observation of defects on polycrystalline mixed metal oxide surfaces by either STM or AFM has not been reported due to the complicated surface morphology. However, the surface of polycrystalline metal oxides can be studied by using probe molecules like molecular oxygen, which interact with the defects. Since the probe molecules may alter the defect in the probing process, a technique that doesn't depend upon any probing molecules can be useful. On oxides surfaces, the oxygen atoms directly coordinated to oxygen vacancies have different chemical environments from other oxygen atoms because of geometric relaxation or charge redistribution. Probing these oxygen atoms with appropriate techniques should generate information on defects associated with these atoms.

Electron stimulated desorption (ESD) is a surface specific technique that has been applied to the investigation of stimulated processes on metal oxide surfaces for decades.[13,25] Electron stimulated desorption of O^+ from metal oxide surfaces mainly comes from the oxygen-metal bond breaking and therefore may bear important information regarding the oxygen ions adjacent to the oxygen vacancy sites. The properties and structures of these vacancies can therefore be extracted from carefully controlled O^+ ESD studies. Our past investigation of polycrystalline GDC surfaces using

ESD has demonstrated a positive correlation of O^+ desorption yields and surface defect density.[114]

In this chapter we report a highly efficient O^+ desorption from defect sites created by ultra-high vacuum annealing. This desorption is most likely from the oxygen atoms associated with both isolated oxygen vacancies and linear oxygen vacancy clusters. These oxygen atoms have lower electron density and therefore a higher probability of being desorbed as cations. Water and molecular oxygen adsorption on the GDC surfaces suppresses the O^+ desorption, clearly indicating the interaction between the adsorbates and the vacancies. The O^+ kinetic energy measurements at different temperatures and electron energies reflect the generation and dissipation of surface charge. An activation energy for charge migration in GDC is deduced from these measurements.

5.3 Experimental details

The details of $Ce_{0.9}Gd_{0.1}O_{2-\delta}$ (GDC) sample preparation and characterization by X-ray diffraction and scanning electron microscopy are reported elsewhere.[114] The GDC samples used in this study have a polycrystalline fluorite structure (grain size 1 to 5 μm) and significant number of grain boundaries. The dimensions of the GDC pellet were about 10×6×1 mm.

ESD measurements were performed in an ultrahigh vacuum system with a base pressure of 2×10^{-10} torr. The system is equipped with a quadrupole mass spectrometer (QMS), a time-of-flight (TOF) mass spectrometer, a pulsed low-energy electron gun, a calibrated dosing system, and a heating-cooling system.

The GDC sample was mounted to a conductive molybdenum plate which was used to heat the sample and to apply a bias. It was annealed to 400 ºC to remove organic contaminants from the surface. The oxygen used is from Matheson with a purity of 99.998% and dosed into the chamber through a leak valve. Water was dosed to the surface through a directional doser after several freeze-pump-thaw cycles to remove dissolved gases. The sample was irradiated by the pulsed electron beam at 1000 Hz with an electron flux of 10^{14} electrons/cm^2s during a given pulse or time-averaged currents of 200 pico-Ampere to a few nano-Ampere. Emitted cations were collected by applying a -50 V pulsed extraction potential to the TOF front lens assembly just after the end of the electron pulse. This avoids the influence of the potential field on the incident electron energy. All ions were detected using pulse counting and a transient digitizer. Three ESD-TOF spectra were taken at each electron energy and the average yield was used for threshold measurements. The yields were normalized to the electron beam current measured by a Faraday cup at each incident electron energy.

For ion kinetic energy measurements, both the extraction potential and tube potential were set to zero and the free field ion velocity distributions were measured. For each data point, at least five spectra were taken and averaged. A standard coefficient of deviation for the peak kinetic energy measurements is less than 1%. The Jacobian transform was used to calculate the kinetic energy distribution of ions from the velocity distribution.

5.4 Results and discussion

5.4.1 Highly effective O^+ ESD

TOF spectra of electron stimulated desorption from GDC surfaces at room temperature are presented in Figure 5.1. The incident electron energy was 200 eV and the samples were annealed at 850 K and 650 K in vacuum. The main desorption products from both samples are H^+ and O^+. The H^+ desorption from the sample annealed at 850 K is only 2.5 times of that annealed at 650 K but the O^+ ESD is greater than 100 times. The enhancement of the O^+ ESD yield can be as high as 300 times with elongated annealing time. This suggests that the surface sites for O^+ desorption on the GDC sample annealed at higher temperature are greatly different from those annealed at lower temperature, and even the desorption mechanism may also be different.

According to the NC-AFM study of defects on $CeO_2(111)$[111] surface, the increase in annealing time results in a higher oxygen vacancy density. The oxygen anion density on the top layer of $CeO_2(111)$ is 7×10^{14} /cm^2. Isolated oxygen vacancies are dominant when the vacancy density is below 1×10^{13} /cm^2. However, when the vacancy density is 4×10^{13} /cm^2, line defects and triangular defects form. From a nearly stoichiometric surface to a surface with multiple defects, the vacancy density change is less than 50 times, but the O^+ yield change is more than two orders of magnitude. The O^+ yield change then can not be accounted for by the vacancy density change only. Line defects and triangular defects are likely present on the GDC surface annealed at 850 K and O^+ ESD from oxygen atoms associated with these types of defects is more efficient than from isolated oxygen vacancies.

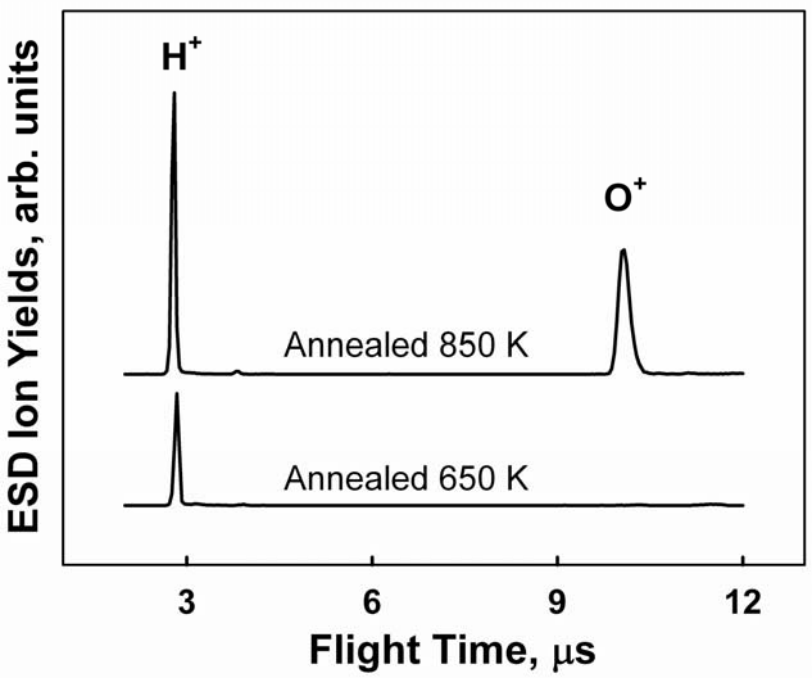

Figure 5.1 ESD-TOF spectra from GDC surfaces at room temperature. The GDC surfaces are annealed at 650 K and 850 K, respectively. The incident electron energy is 200 eV and the pulse length is 200 ns.

The dependence of O^+ desorption on incident electron energy is very useful in elucidating the dominant desorption mechanisms and is shown in Figure 5.2. The O^+ ESD has a major threshold at 40 eV, with a weak onset for O^+ around 20 eV, and an even weaker onset ~ 15 eV. The major threshold shifts slightly to higher incident energy as accumulating annealing time increases. The peak O^+ kinetic energy is greater than 5.6 eV at room temperature (see section 6.5), indicating that O^+ desorption is non-thermal.

Previous investigations on O^+ ESD from various metal oxides has demonstrated that O^+ desorption likely proceeds via an Auger-stimulated desorption mechanism described by Knotek-Feibelman model.[23] On the surface of metal oxides, oxygen anions are considered to have a nominal negative charge of two. To produce an O^+, three

electrons need to be removed from the oxygen atom. According to Knotek-Feibelman model, core holes of metal atoms are filled by electrons Auger cascading from the valence band formed by the O 2p level. This can produce multiple holes on terminal oxygen atoms and can yield O^+. The Coulombic repulsion between the O^+ and neighboring metal ions desorbs non-thermal oxygen cations. This mechanism directly correlates desorption thresholds to the core level binding energies. For GDC, the 40 eV major threshold suggests that the desorption of O^+ originates from the core level excitation of Ce 5s (36.8 eV) and Gd 5s (46.2 eV), and the weak onset at 20 eV may be associated with O2s level (21.8 eV).[88,91,115]

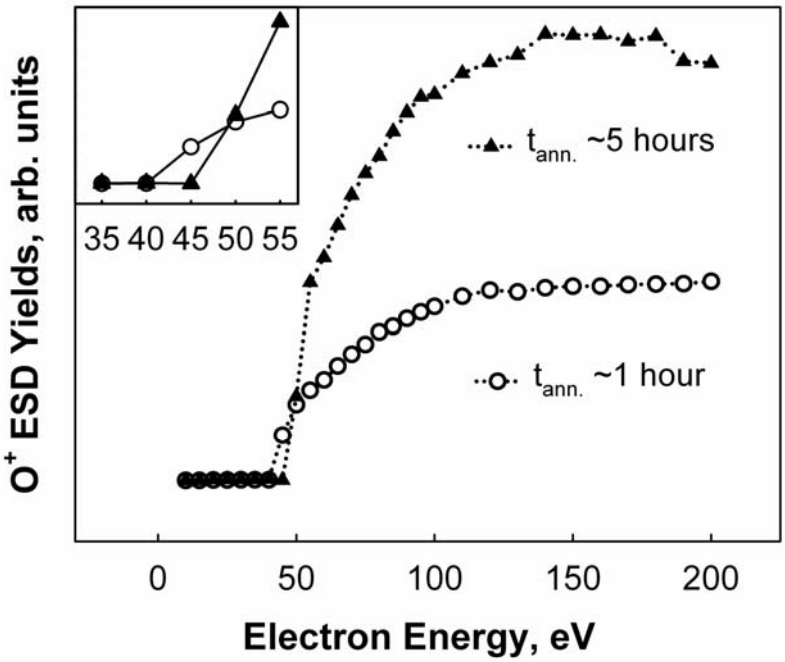

Figure 5.2 The energy dependence of O^+ ESD from GDC surface at room temperature. The only difference between the two spectra is the annealing time t_{ann}. The electron pulse length is 200 ns and the yields are normalized to the incident flux.

5.4.2 Electron density on oxygen atoms and O^+ ESD

In principle, the probability of an electronic excitation is higher when fewer electrons are involved. The above mentioned three-electron inter-atomic Auger process is very inefficient as manifested by generally low O^+ ESD yields from metal oxide surfaces. This mechanism is therefore not enough to account for the extremely high O^+ yield observed from the polycrystalline GDC surface annealed at 850 K. Any process that involves less than three electrons should result in more efficient O^+ ESD.

If the electron density on oxygen atoms is smaller than two, then less than three electrons need to be removed to produce O^+. In fact, the charge on oxygen atoms on the top layer of metal oxides is greatly influenced by their chemical environment. The chemical environment of oxygen atoms in a mixed metal oxide can be different from either of the oxide components. For example, first principle density functional calculations show that at least three different types of oxygen atoms are present in $Ce_{0.8}Zr_{0.2}O_2$.[116] O K-edge X-ray absorption near-edge spectroscopy (XANES) spectra support that oxygen atoms in $Ce_{0.8}Zr_{0.2}O_2$ are in special chemical environments different from ZrO_2 or CeO_2. For $Ce_{0.8}Zr_{0.2}O_2$, the calculated Mulliken charge on oxygen atoms is lower than that on ZrO_2 and CeO_2. For GDC, a mixed oxide similar to $Ce_{0.8}Zr_{0.2}O_2$, there may be oxygen atoms with less charge, and lower electron density on oxygen atoms means higher probability of O^+ emission.

The positive correlation between O^+ ESD yield and defect density on GDC surface has been demonstrated[114] and is observed at a grander scale in this experiment. A

close examination of the influence of the neighboring oxygen vacancies on the charge of top layer oxygen atoms may provide insights into the desorption mechanisms. For oxygen vacancies, there are related defect states available in the band gap. If the defect state is empty, electrons from oxygen ions coordinated to the oxygen vacancy may delocalize to these defect states. As a result, the electron density on these oxygen atoms is lowered and the oxygen atom may appear as O^{-} instead of O^{2-}. For this oxygen to be desorbed as O^{+}, only two electrons need to be removed and the desorption has a higher probability than a three-electron desorption process.

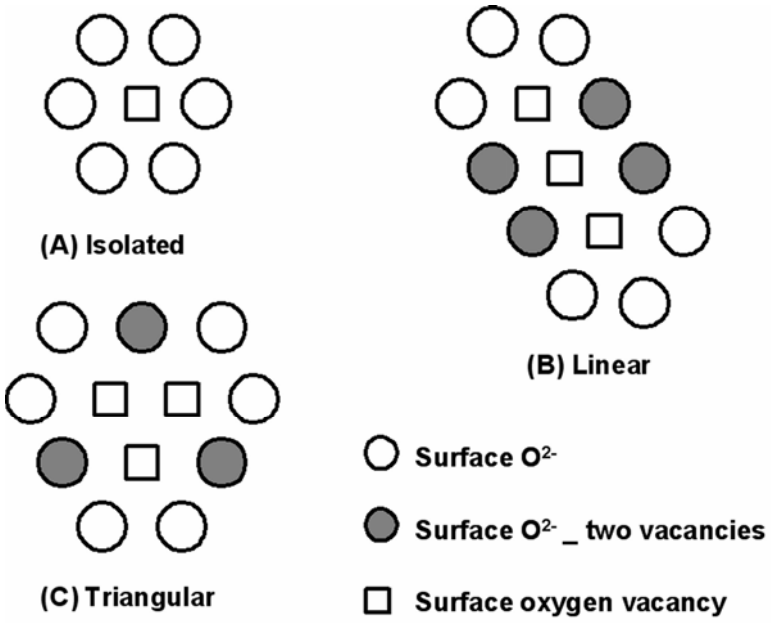

Figure 5.3 Structures of surface oxygen vacancies and vacancy clusters on a GDC (111) surface. Only the oxygen anions and vacancies in the top layer are shown.

In Figure 5.3, the chemical environment of the top layer oxygen atoms adjacent to different types of vacancies on GDC (111) surfaces is schematically presented. For oxygen ions coordinated to an isolated oxygen vacancy, the electrons on oxygen have a

chance to delocalize to one defect state. For oxygen atoms surrounding linear vacancy clusters and triangular clusters, one oxygen ion can be coordinated to two oxygen vacancies. Oxygen atoms surrounded by up to three vacancies can be seen on the STM image of CeO_2 (111)[106]. Since there are more defect states available to these highly vacancy coordinated oxygen atoms, the electron transfer probability from oxygen to these defect states is high. This may produce the equivalent of O neutral hopping on the surface. The O^+ desorption from this site should then be much easier than other sites since it is necessary to remove only one electron. As a matter of fact, we observe a very weak onset for O^+ desorption ~ 15 eV (data not shown), close to the first ionization potential of neutral oxygen atoms.

However, coordination to oxygen vacancies or vacancy clusters is not the only condition for highly efficient O^+ desorption. To be able to accept electrons from oxygen anions, the defect states have to be empty. Under electron irradiation, the defect states of GDC trap electrons at lower electron energy and holes at higher electron energy.[86] If the defect states are filled, no electrons from oxygen atoms can be delocalized to the defect states. One pathway to remove the electrons from the defect states is the recombination of electrons with holes. This process is actually a charge neutralization process and can be used to account for the shape of the O^+ ESD energy dependence curve and the influence of annealing history on threshold energies. The leading edge of the energy dependence curve is very steep, manifesting the underlying charge neutralization process. With increasing annealing time, increasing number of defects trap more electrons, and more holes are required to neutralize these electrons to create empty states. This is in agreement with the observed increase of threshold energy with annealing time.

5.4.3 Defect healing by water and molecular oxygen

From the above discussion, it is clear that the variation of surface defect density and occupation of defect states influences O^+ ESD. Water and molecular oxygen are known to adsorb to GDC surfaces dissociatively or non-dissociatively at room temperature. These adsorption processes occurs mainly at the oxygen vacancy sites and therefore can either heal the defects or change the occupancy of defect states. Under either case, the O^+ ESD yield is expected to be lower than without adsorption.

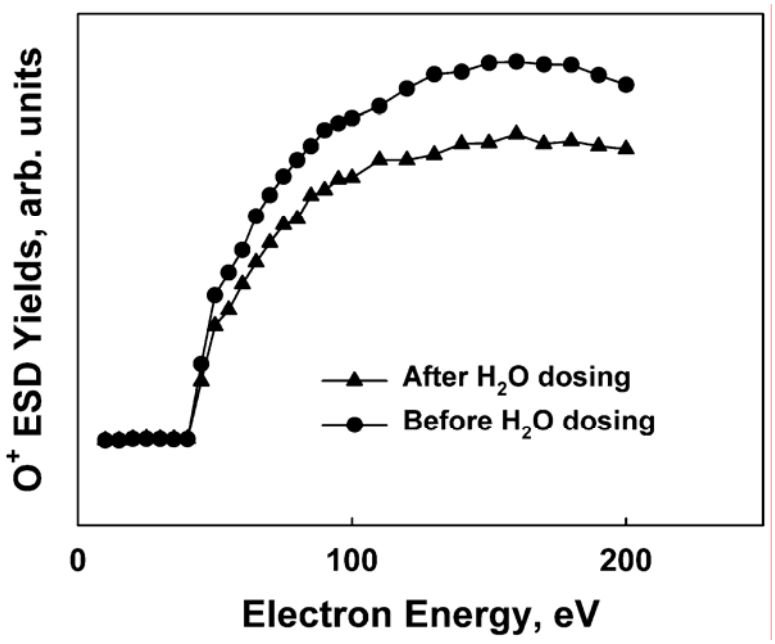

Figure 5.4 Energy dependence of electron stimulated desorption of O^+ from GDC surfaces before and after water dosing at room temperature. The pulse length of the electron beam is 200 ns. The water exposure is 100 L.

At room temperature, the O^+ yield is decreased by ~20% after GDC surfaces are exposed to ~ 100 L of water (Figure 5.4). This O^+ yield decrease can be associated with the occupancy of oxygen vacancies by water molecules. The major threshold remains ~40 eV, indicating that water adsorption doesn't change the occupancy of defect states. At the same time, the yield of H^+ ESD (not shown), an indicator of the amount of surface hydroxyl groups, is slightly increased. These results suggest the pre-existence of hydroxyl groups and may indicate that the majority of water adsorption is non-dissociative.

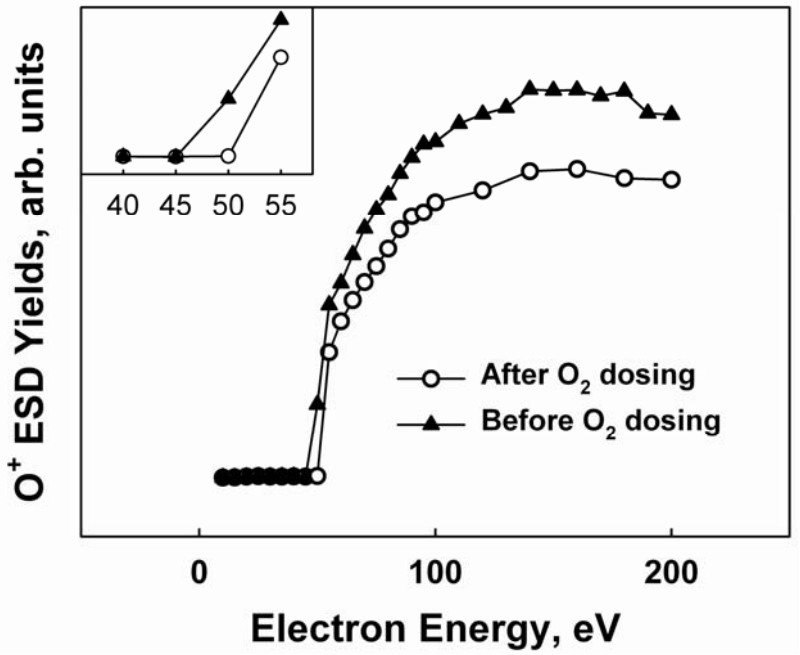

Figure 5.5 Electron energy dependence of O^+ ESD from GDC surfaces before and after molecular oxygen dosing. The pulse length of the electron beam is 200 ns. The base pressure of the chamber is 2×10^{-10} torr and the oxygen exposure is about 100 L.

Similar to water adsorption, O_2 adsorption decreases the O^+ ESD yield by ~20% (Figure 5.5), close to the suppressing effects of water on O^+ ESD. This suggests that both

water and oxygen adsorb to similar vacancy sites. A dynamic NC-AFM study shows that molecular oxygen heals mainly the vacancy clusters instead of isolated vacancies.[111] Water may heal the same type of clusters, most likely linear vacancy clusters.

In contrast to water adsorption, after oxygen dosing, the major O^+ ESD threshold shifts to higher electron energy. This is a strong indication that oxygen adsorption can modify the occupancy of defect states. The higher threshold energy reveals that it is harder to remove the trapped electrons from defect states when O_2 is adsorbed. Since molecular oxygen has a positive electron affinity, O_2^- can form and be stabilized on the surface by electrostatic interactions with metal oxide surfaces. This can produce a Schottky barrier that traps electrons to the metal oxide surface and therefore decreases the number of empty defect states essential to effective O^+ desorption.

5.4.4 Dependence of O^+ kinetic energy on incident electron energy and temperature

A high intensity O^+ ESD signal makes accurate kinetic energy measurements possible even at relatively low incident electron energy. The kinetic energy of O^+ desorbed from the surface of insulating material GDC is the sum of two components. One component originates from the Coulombic repulsion between desorbing O^+ and lattice cations and the other is from the acceleration by the electrical field induced by irradiation. For convenience of discussion, the former is referred as intrinsic kinetic energy, the later as surface potential, and the measured kinetic energy as apparent kinetic energy. If the last step of non-thermal O^+ desorption is bond breaking and Coulombic repulsion, the intrinsic energy should not be influenced either by incident electron energy or surface

temperature. Extrapolation of apparent kinetic energies should yield both intrinsic kinetic energy as well as surface potentials for specific experimental conditions.

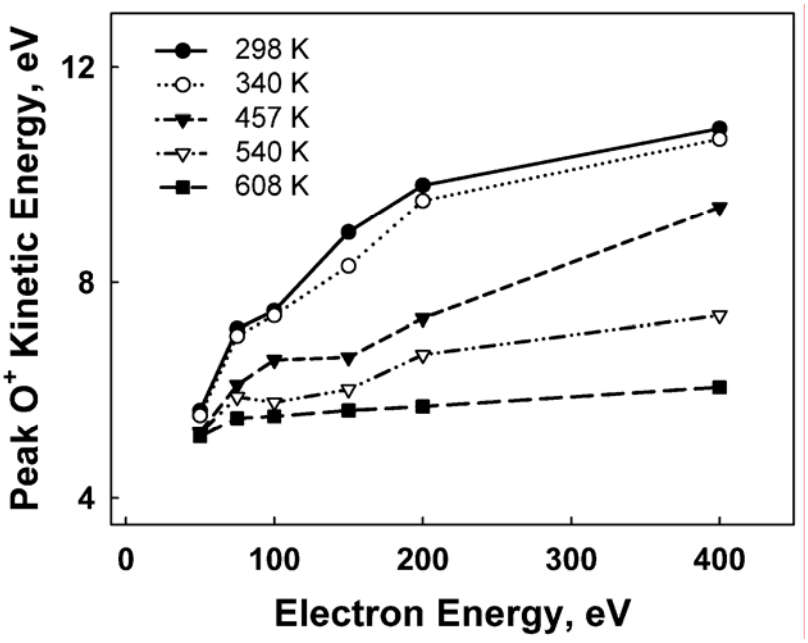

Figure 5.6 Energy dependence of the O^+ peak kinetic energy at different temperatures.

Figure 5.6 represents the dependence of O^+ peak kinetic energy on incident electron energy at different temperatures. At all temperatures studied, measured peak O^+ kinetic energies increase with electron energy. For example, at room temperature, the peak O^+ kinetic energy at 400 eV is 5.2 eV higher than at 50 eV. The increase of apparent kinetic energy with incident electron energy indicates that there is more and more positive charge on the surface at higher electron energy. Since negative surface charging at lower electron energy and charge neutralization has been observed on GDC,

there might be a specific condition under which the surface is dynamically neutral and the apparent kinetic energy at this condition can be considered as intrinsic kinetic energy. Interestingly, from Figure 5.6, the apparent kinetic energies appear to converge.

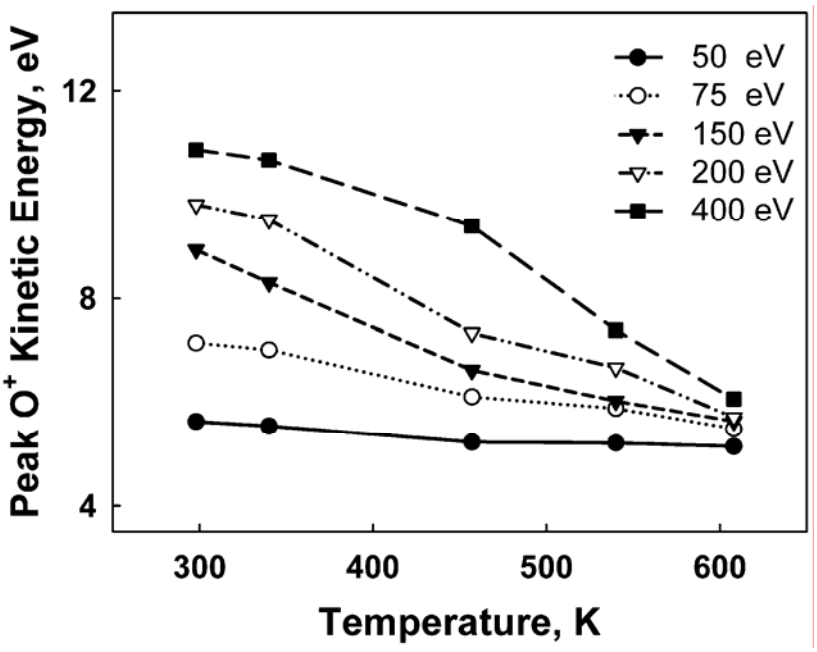

Figure 5.7 Temperature dependence of O^+ peak kinetic energy at different incident electron energies.

The influence of temperature on the O^+ kinetic energy can be viewed more clearly in Figure 5.7. For all incident electron energies, the O^+ kinetic energies decrease with increasing temperature and tend to converge to the same energy at high temperature. The temperature influences the kinetic energy more sensitively at higher incident electron energy than at lower electron energies. Judging from the general trend of the influences of temperature and electron energy on O^+ kinetic energy, the intrinsic kinetic energy can be experimentally measured at low energy and high temperature. At 45 eV, 596 K, from

the average of 30 spectra, the peak O^+ kinetic energy is found to be 5.6 eV. Water and oxygen adsorption have no influence on O^+ kinetic energy at room temperature. This result is well within the range of reported O^+ kinetic energy from ESD of TiO_2 (110) (4 eV and 7 eV)[117] and in agreement with the Coulombic repulsion from metal-oxygen bond breaking. With this measured intrinsic kinetic energy, the surface potential can be experimentally obtained by subtraction of intrinsic kinetic energy from apparent kinetic energy. The charge density calculated from the surface potential measured this way is ~ 1.2×10^8 electrons / cm^2 for 400 eV electrons at room temperature.

5.4.5 Surface charge dissipation

The surface potential is determined by the charge type and charge density on the surface. At higher electron energy, the dominant charge is positive. This can be an envelope of all positive charge carriers present on the surface, including holes trapped at Gd^{3+} sites or at lattice oxygen sites. If we assume the trapped positive charge on the surface forming a sheet of charge in an area of the electron beam spot size, then the charge density σ can be calculated from the surface potential. This charge density is a measure of the difference between the charge produced at the surface and charge dissipated from the surface during the electron pulse, which has a pulse length of 200 ns. Therefore, the charge density on the surface can be treated as an equivalent to the difference between the rate of charge production and charge dissipation ($R_{\text{charge dissipation.}}$). Since the charge generation is an electronic process that is determined by electron energy, then its rate can be considered as a constant at fixed electron energy and independent of

temperature. In contrast to charge production, the charge dissipation is a thermally activated process and is dependent on temperature. In general, the charge generation rate increases with electron energy and hole dissipation rate increases with temperature. The measured peak O^+ kinetic energies represented by Figure 5.6 and Figure 5.7 clearly display these trends.

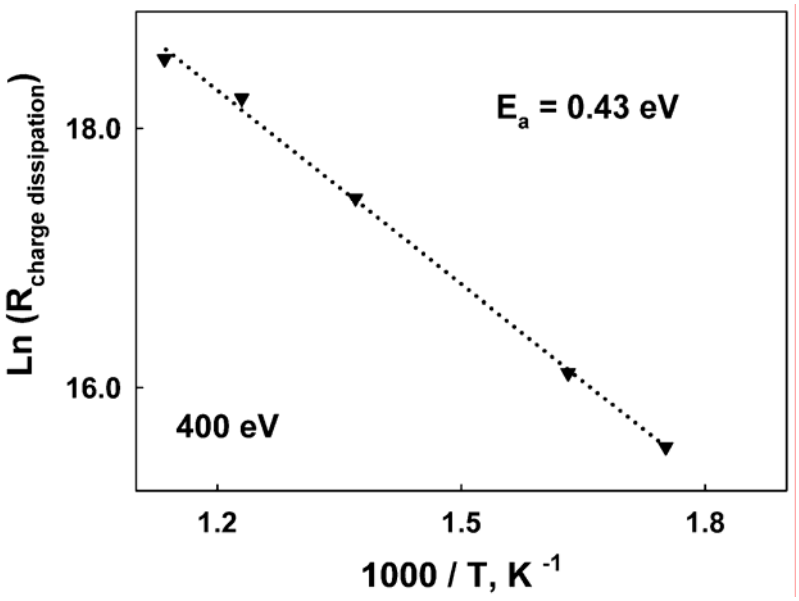

Figure 5.8 Arrhenius plot of charge dissipation rate deducted from surface charge density. The incident electron energy is 400 eV and the pulse length is 200 ns.

During the pulse, the charge dissipation rate, $R_{charge\ dissipation}$, defined as the number of charges dissipated from a unit area of the surface, is then proportional to the difference between the number of charges generated (constant at fixed electron energy) and the number of charges remained on the surface (calculated from the surface potential). An Arrhenius plot of this difference should yield a direct estimation of the activation energy for charge dissipation. Since at 400 eV the dominant surface charge are holes and the positive charge density is highest among all the measured energies, the 400 eV kinetic

energy data are then chosen for an more accurate estimation of the charge dissipation through GDC. The unknown constant is fit by a minimum least square procedure and the result is presented in Figure 5. 8. An apparent activation energy of 0.43 eV is found for the charge dissipation and the R^2 value for the fit is 0.998. However, the nature of dissipated charge carriers is not clear. They can be holes, electrons, oxygen vacancies, or any combination of them.

If the hole conduction is considered as having significant contributions to the overall charge dissipation, previous studies on this topic can be of help. However, for hole conduction through GDC, the activation energy extracted from the electrochemical impedance measurement at very high oxygen partial pressure is very diverse. For example, the activation energy for p-type conductivity of $Ce_{0.8}Gd_{0.2}O_{2-x}$ was found to be 3.6 eV[49], 1.3 eV[51], and 1.5 eV[118] by different groups, much larger than 0.43 eV. This difference may suggest that the hole migration may not be a dominant dissipation path. For GDC samples prepared with the same procedure as of this experiment, the activation energy for electrical conduction is between 0.47 eV[40] to 0.61 eV[46], closer to 0.43 eV than that of hole conduction. It is likely both electronic and ionic charge carriers are involved in the surface charge dissipation. Further investigation is needed to explore the nature of the charge carriers and the charge dissipation mechanism to account for this observation.

CHAPTER 6

OXYGEN ADSORPTION INTERMEDIATES ON GADOLINIA-DOPED CERIA SURFACES BY ELECTRON STIMULATED DESORPTION

6.1 Overview

The interactions of gas phase molecular oxygen with gadolinia-doped ceria (GDC) surfaces are investigated by electron stimulated desorption (ESD). The primary desorbed cationic species related to molecular oxygen adsorption is O_2^+. The ESD of O_2^+ yield has a threshold of 13 ~ 14 eV, indicating direct ionization of molecular oxygen containing adsorption complexes such as O_2^- formed at oxygen vacancies. The dependence of O_2^+ kinetic energies upon incident electron energy and substrate temperature reveals the dominant influence of the effective charge of the adsorption complex. The O_2^+ kinetic energy distribution is bimodal, and the onset of the faster components at room temperature may be due to the onset of hole production and subsequent reneutralisation of electrons trapped at surface states. The material in this chapter will be submitted for publication in Surface Science.

6.2 Background

Polycrystalline gadolinia-doped ceria (GDC) has been widely investigated as a promising low temperature solid oxide fuel cell (SOFC) electrolyte and as part of

composite electrodes to facilitate ionic conduction within the electrodes.[36,46,66,119] Oxygen reduction is generally thought to be confined close to the electrode / electrolyte interface and the adsorption of oxygen at various surface sites at the interface is the first step toward oxygen reduction.[10] An understanding of molecular oxygen interactions with GDC surfaces may provide insight into the oxygen reduction process at electrode /electrolyte interfaces. Since the GDC is doped ceria and has the same fluorite structure as that of CeO_2, the knowledge on the interaction of oxygen with CeO_2 surfaces can help the investigation of O_2 adsorption on GDC. The main difference between GDC and CeO_2, however, is that Gd^{3+} is not active in electron transfer while cerium can change its oxidation state readily between Ce^{3+} and Ce^{4+}.

The interactions of molecular oxygen with transition metal oxide surfaces are important in many processes involving oxygen reduction or catalytic oxidation. Various intermediates from physically adsorbed oxygen, superoxide (O_2^-), peroxide (O_2^{2-}), to O^- can be formed before oxygen is reduced to lattice O^{2-} as shown in the following equilibria:

O_2 (gas phase) $\leftrightarrow$ O_2 (ads) $\leftrightarrow$ O_2^- (ads) $\leftrightarrow$ O_2^{2-} (ads) $\leftrightarrow$ O^- (ads) $\leftrightarrow$ O^{2-} (L). For ceria, molecular oxygen presumably adsorbs at oxygen vacancy sites on partially reduced surfaces, but the exact adsorption state is not very clear.[120] Temperature programmed desorption (TPD) studies indicate that oxygen desorbs between 800 to 1250 K from ceria films.[121] Electron paramagnetic resonance (EPR) and Fourier transferred infrared (FTIR) studies show that a variety of paramagnetic superoxide radical species can be detected on many metal oxide surfaces [122] and on polycrystalline ceria surfaces.[123,124] The EPR signal of superoxide species on ceria surfaces can be grouped into two types, one is thought to be related to isolated oxygen vacancies and the other to aggregated oxygen vacancies.

The bonds between the superoxide and the surface have different degrees of covalency but the exact picture of charge localization is not completely clear. UV irradiation of CeO_2 nanoparticles [125] and CeO_2/TiO_2 [126] in the presence of oxygen greatly increases the amount of superoxide radicals. These studies were performed with an ex-situ procedure and neither physically adsorbed O_2 nor O_2^{2-} species were observed by EPR or FTIR.

An in-situ Raman spectroscopy investigations of O_2 adsorption on polycrystalline CeO_2 surfaces[127] revealed the presence of O_2 physical adsorption at very low temperature (93 K) and two types of O_2 chemisorption states associated with various oxygen vacancy sites. These include isolated, linear, triangular, as well as other vacancy aggregates. The non-dissociatively chemisorbed oxygen species can be designated as O_2^- or O_2^{2-}, depending on the cations they are associated with. The thermal stability of O_2^{2-} is higher than O_2^-, and the lifetime of the oxygen species on the surface is not exactly known. The O_2 species is stabilized by the cations in the vicinity but the overall interaction is weak.

Electron stimulated desorption (ESD) is a surface specific technique that can provide valuable information concerning surface and adsorbate structures.[13] The conventional scheme of ESD in the study of gas-solid interactions is to directly investigate the adsorbate-substrate complex. This method has yielded important information on systems such as H_2 / TiO_2 (001), NH_3 / TiO_2 (110), SO_2 / TiO_2 (110), CO / TiO_2 (110), and NO / TiO_2 (110).[25] However, this method only probes adsorbed species with long life times. The rich dynamic interaction of the gas phase with the surface is completely lost. Our recent application of ESD to GDC[86,114] has established a fundamental understanding of the GDC surfaces and has set a foundation for exploration of the interactions between GDC and oxygen.

In this chapter, we present an ESD study of non-dissociative chemical oxygen adsorption on polycrystalline gadolinia-doped ceria surfaces. We describe the experiments in Section 6.3 and the results in Section 6.4. Specifically, the electron stimulated desorption of O_2^+ is shown to originate from the GDC surfaces after O_2 adsorption. The influences of incident electron energy and substrate temperature on yields and velocity distributions are also presented in Section 6.4. The mechanism of O_2^+ desorption is discussed in terms of ionization of various oxygen adsorption complexes in Section 6.5.

6.3 Experimental details

The details of $Ce_{0.9}Gd_{0.1}O_{2-\delta}$ (GDC) sample preparation and characterization by X-ray diffraction and scanning electron microscopy are reported elsewhere[46]. The GDC samples used in this study have a polycrystalline fluorite structure (grain size 1 to 5 μm) and a significant number of grain boundaries. The dimensions of the GDC pellet were about 10×6×1 mm.

ESD measurements were performed in an ultrahigh vacuum system with a base pressure of 2×10^{-10} torr. The system is equipped with a quadrupole mass spectrometer (QMS), a time-of-flight (TOF) mass spectrometer, a pulsed low-energy electron gun, a calibrated dosing system, and a heating-cooling system sample mounting system.

The GDC sample was mounted to a conductive molybdenum plate which was used to heat the sample to 400 ºC to remove all contaminants from the surface. The oxygen used is from Matheson with a purity of 99.998%. The sample was irradiated by

the pulsed electron beam at 1000 Hz, and emitted cations were collected by applying a -50 V pulsed extraction potential to the TOF front lens assembly just after the end of the electron pulse. For mass resolved ESD measurements, the QMS (with its ionizer turned off) was employed as the mass analyzer. In general three ESD-TOF spectra were taken at each electron energy and the average yield was used for threshold measurements. The yields were normalized to the electron beam current measured by a Faraday cup.

6.4 Results

6.4.1 Electron stimulated O_2^+ desorption

Electron stimulated desorption (ESD) of cations from gadolinia-doped ceria surfaces during the dosing of molecular oxygen is depicted in Figure 6.1. Before oxygen dosing, the dominant desorption species is H^+ (see Figure 6.1, panel A) plus an insignificant amount of O^+, H_3O^+ (not shown). When oxygen is dosed and a partial pressure of oxygen ~ 5×10^{-8} torr is maintained, two new peaks with flight time 15.7 μs and 16 μs appear when the surface is irradiated by 65 eV electrons. When the extraction potential is increased, the two peaks merge into one peak with a mass of 32 amu. This mass assignment is reconfirmed by quadrupole mass spectrometry (QMS). These two peaks are therefore assigned as O_2^+ with different velocities and denoted as O_2^+ (f) and O_2^+ (s).

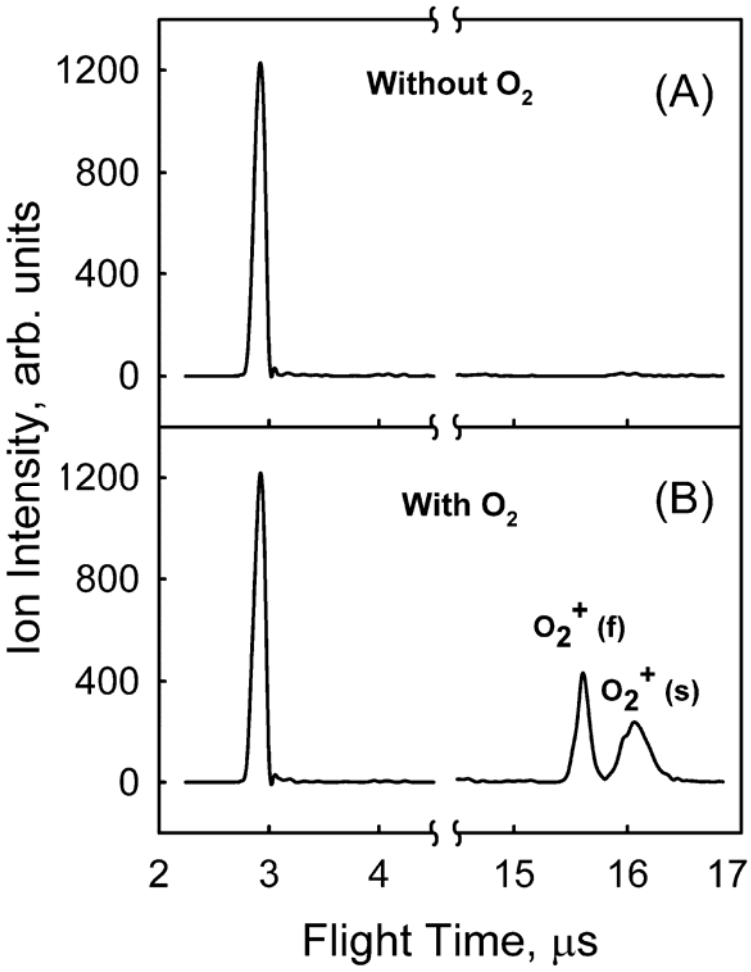

Figure 6.1 ESD-TOF spectrum of cations from a GDC surface in the presence of gas phase molecular oxygen at room temperature. The incident electron energy is 65 eV, the pulse width is 200 ns, the pressure of oxygen is 5×10^{-8} torr, and the extraction potential is – 50 V.

The O_2^+ ESD does not originate from direct electron impact ionization of gas phase oxygen but from electron stimulated desorption from the GDC surface. Under the experimental conditions employed, the number density of gas phase oxygen is 10^9 molecules / cm^3 and the impingement rate is ~ 5×10^{11} molecules / $cm^2 \cdot$ s. Assuming a typical density of surface sites of 10^{15} sites / cm^2, using a sticking probability of 0.04 for CeO_2 at room temperature,[111] simple calculations show that it takes 4×10^4 s to form a

monolayer of oxygen on the surface. When the oxygen is pumped out and ESD-TOF spectrum is taken at chamber base pressure of 2×10^{-10} torr, the total intensity of the O_2^+ desorption is reduced by 97%. This decrease in intensity suggests that the O_2^+ desorption originates from short-lived intermediate oxygen species adsorbed upon the GDC surfaces.

O_2^+ ESD was previously noticed from the O_2 / Si (111) surface[128] with a kinetic energy of 2 eV and also from the O_2 / K / Ru (001)[129] system. To our knowledge, no O_2^+ ESD has been reported from oxygen / metal oxide interactions. Photon-stimulated desorption of neutral O_2 from $YBa_2Cu_3O_{7-x}$ by core level excitation is known.[27] No desorption of O_2^+ is observed in the same experiment, demonstrating that the O_2^+ does not arise from the photoionization of desorbed neutral O_2.

6.4.2 Influence of electron energy and temperature on O_2^+ ESD

To further understand O_2^+ ESD, the influence of incident electron energy on O_2^+ desorption at room temperature was performed and presented in Figure 6.2. From 15 to 55 eV, only one O_2^+ desorption peak with flight time peaked around 16 μs is observed. This peak broadens from 45 eV and its peak position slightly shifts to lower flight time. When electron energy reaches 60 eV, a new O_2^+ peak with peaked flight time around 15.7 μs appears and the intensity of the 16 μs peak decreases. The position of this new peak shifts to shorter and shorter flight time with increasing electron energy and its intensity decreases at the same time. At low extraction potential, the flight time of O_2^+ is influenced by its kinetic energy. The slower component is mainly O_2^+ with lower kinetic energy and the faster component is from O_2^+ with higher kinetic energy.

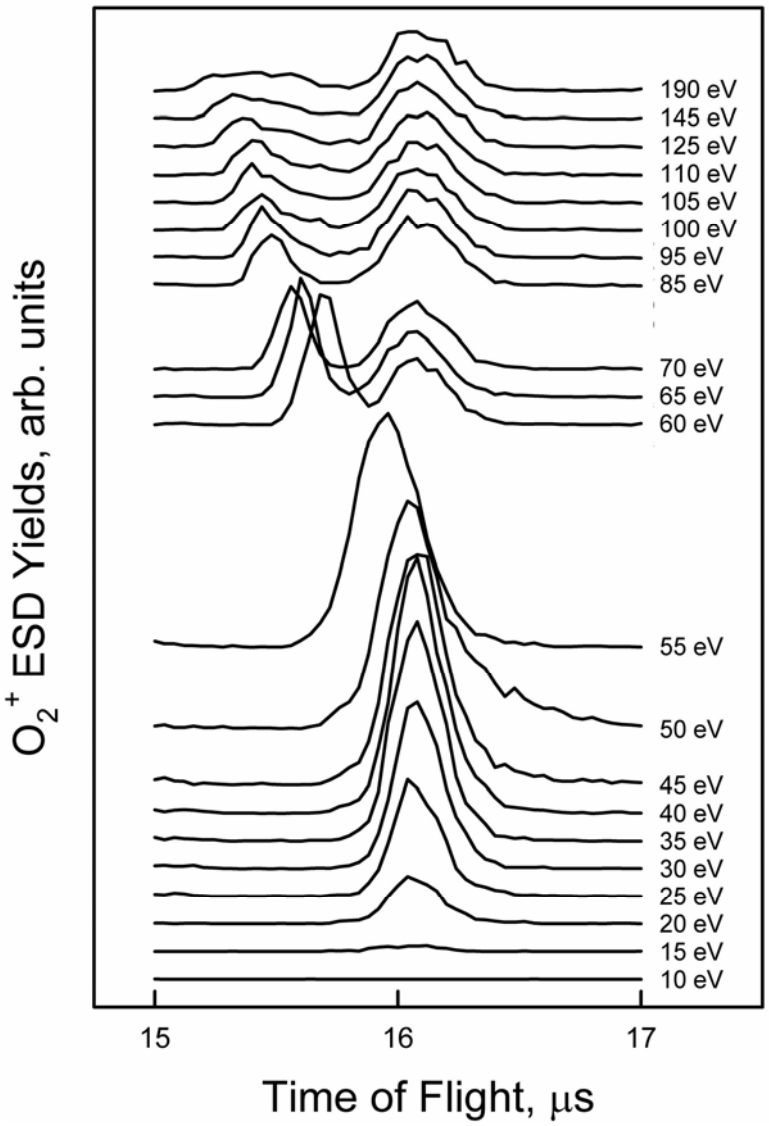

Figure 6.2 O_2^+ ESD-TOF spectra at different incident electron energies at 298 K. The pulse width is 200 ns and the background dosing pressure of oxygen is 5×10^{-8} torr.

The influence of the incident electron energy on the total O_2^+ ESD yield is presented in Figure 6.3. The O_2^+ yield increases with electron energy from 15 eV and up, peaks at 50 eV, decreases from 50 eV to 80 eV, and then levels off. This energy dependence is very different when compared to the cross sections for ionization of gas

phase O_2.[130] In particular, the striking high yield below 80 eV is absent in the gas phase data. The enhanced O_2^+ ESD in this energy range may result from enhanced O_2 adsorption on GDC. This enhancement is consistent with the observation of photon enhanced O_2^- production on TiO_2 and TiO_2 supported CeO_2 surfaces.[126,131]

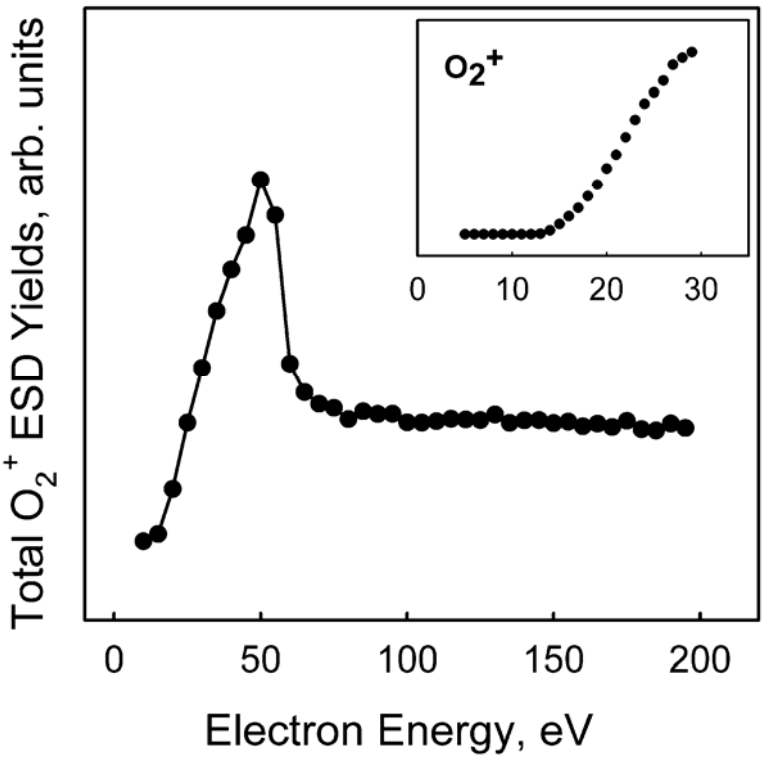

Figure 6.3 Electron energy dependence of total O_2^+ ESD yields at room temperature. The pulse width is 200 ns and the pressure of oxygen is 5×10^{-8} torr.

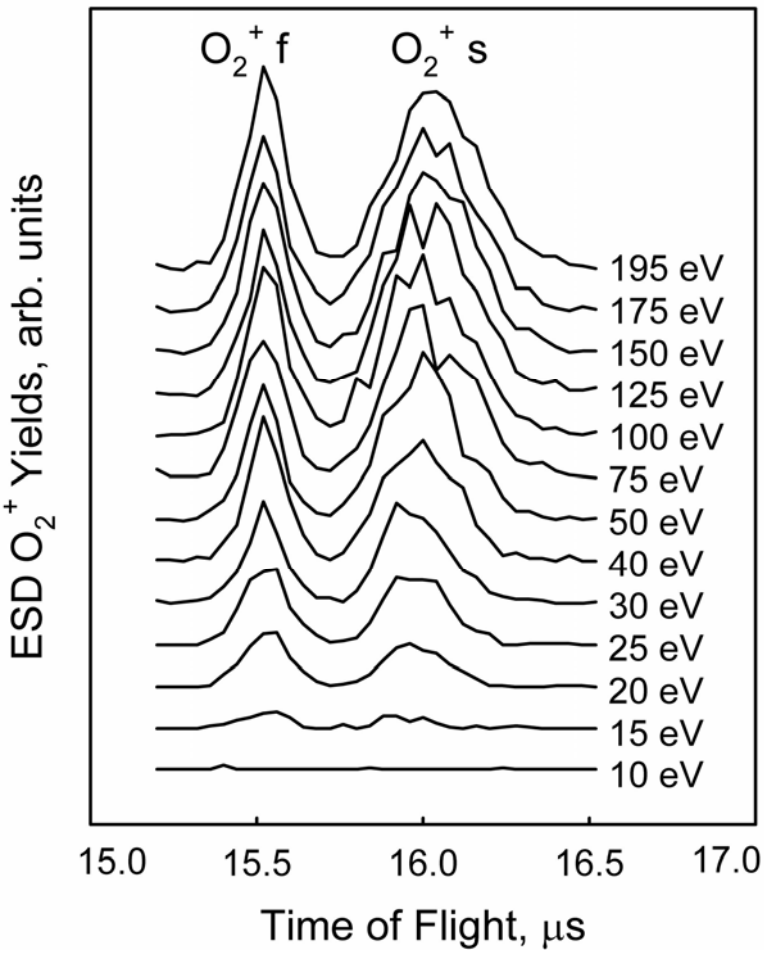

Figure 6.4 O_2^+ ESD-TOF spectra at different incident electron energy at 560 K. The pulse width is 200 ns and the pressure of oxygen is 5×10^{-8} torr.

In order to understand the nature of O_2^+ desorption, the threshold of O_2^+ ESD is measured and presented in the inset of Figure 6.3. The measured threshold of O_2^+ ESD is around ~13-14 eV. This threshold is not close to any of the core levels of Gd 5p (23.0 eV)[88], Ce 5p (18.0 eV)[91] or O2s (21.8 eV)[91]. Therefore, the near threshold O_2^+ ESD can not be caused by ionization of core level electrons of the metal oxide. In fact, this threshold is very close to the ionization potential of molecular oxygen (12.06 eV), indicating that the O_2^+ desorption can originate from electronic excitation or ionization of

adsorbed molecular oxygen species. Metastable quenching spectroscopy results on O_2 / K / Ru (001)[129] show that O_2^+ ESD is most likely from O_2^-, and possibly from O_2^{2-}.

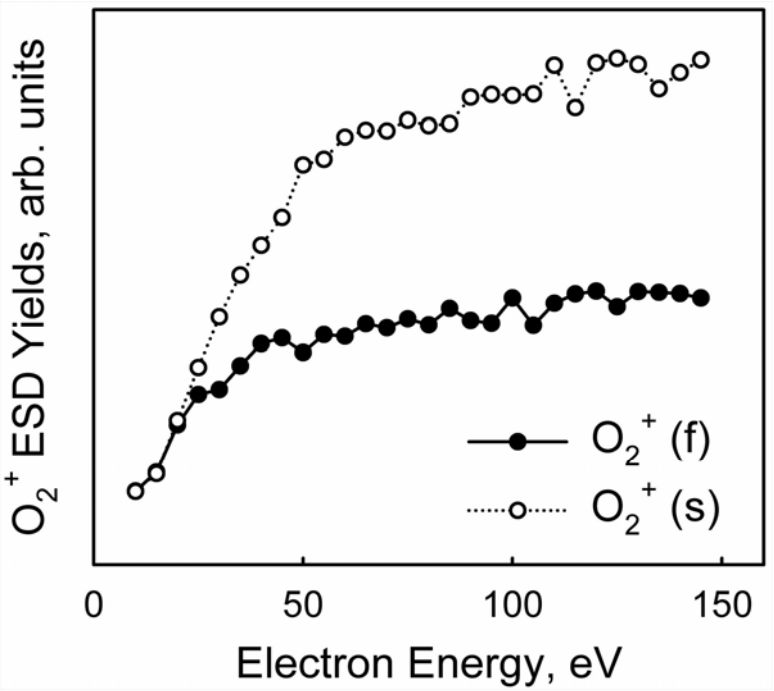

Figure 6.5 Electron energy dependence of O_2^+ ESD at 560 K. The pulse width is 200 ns and the pressure of oxygen is 5×10^{-8} torr.

O_2^+ ESD-TOF spectra at 560 K presented in Figure 6.4 are different from those obtained at room temperature (Figure 6.2) in several ways. First, at 560 K, the peak positions of two O_2^+ components shift very little with electron energy, and the very fast O_2^+ component with 15.4 μs flight time is not seen. Second, the absolute intensities of O_2^+ (f) and O_2^+ (s) at 560 K are smaller than those at room temperature, especially at lower electron energies. For example, at 50 eV, the total O_2^+ ESD yield is reduced by 85%. Third, at high temperature, the onset of the fast component of O_2^+ is the same as the slow component. It is 13 ~ 14 eV instead of the ~ 40 eV onset of O_2^+ (f) at room

temperature. At high temperature, the enhancement of oxygen adsorption at lower electron energy is not observed (See Figure 6.5). These differences from room temperature ESD-TOF manifest the influence of thermal excitation processes or thermally activated processes on O_2^+ desorption.

6.5 Discussion

6.5.1 O_2^+ ESD mechanism

The chemically adsorbed oxygen intermediates are considered to be primary precursors for O_2^+ ESD. When molecular oxygen is contacted with the surface of a metal oxide, the formation of O_2^- will occur if the energy of the adsorbed negative moiety lies below the Fermi level of the solid.[131] Electrons from partially reduced metal oxides, electrons trapped in oxygen vacancies, or electrons induced by photon irradiation, [132] can be transferred to molecular oxygen to form superoxide or peroxide. Since the electron affinity of the oxygen is positive but rather small (0.44 eV), the electrostatic contribution to the stabilization of the anionic species on the positive ions at the surface plays a fundamental role. For O_2 / MgO (100), ab initio cluster model calculations show that O_2^- is electrostatically bound with adsorption energies from 2 to 4 eV and is ~ 1.5 Å from the surface.[133]

Figure 6.6 is a very simplified schematic energy diagram of GDC and O_2 using vacuum level as common reference. In the diagram, the valence band, defect states (an anion vacancy with two electrons, or F center), Fermi level, and the conduction band of

GDC are shown. The band gap width of GDC is unknown, but estimated from the band gap of CeO_2 (~6 eV) and Gd_2O_3 (5.3 eV), the band gap of GDC should be around 5~6 eV. The highest occupied molecular orbital (HOMO) of ground state of molecular oxygen lies within the valence band of GDC while the lowest unoccupied molecular orbital (LUMO) lies below Fermi level of GDC. The HOMO of O_2 is about 12 eV below vacuum level, and the LUMO is about several electron volts above HOMO. The energy level of the defect state depends on the number of trapped electrons and is unknown. The LUMO of oxygen may lie below the F center type vacancy state, but its accurate level is also unknown.

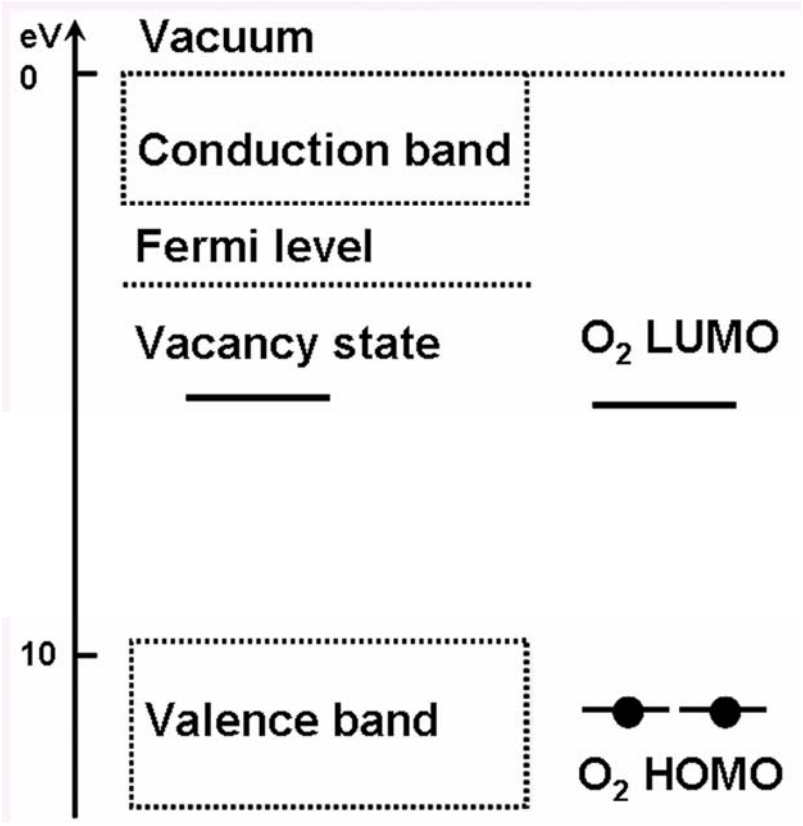

Figure 6.6 Schematic energy diagram of GDC and O_2

Without electron irradiation, when O_2 adsorbs on a vacancy with one or two trapped electrons, these electrons can be transferred from the level of the defect to the LUMO of oxygen, and O_2^- and / or O_2^{2-} can be formed and stabilized on the surfaces. If an oxygen vacancy is coordinated by two Gd^{3+} cations, no electrons on the defect level are available and no electrons can be transferred to oxygen without electron irradiation. However, if electrons are excited to the conduction band and captured by O_2, superoxide or peroxide may form on the surface. The life time of these oxygen intermediates may be influenced by the recombination of electrons with holes. Even though the denotation of O_2^- or O_2^{2-} is used to represent the adsorbed oxygen to oxygen vacancies, the number of electrons (one, two, or a fraction of electrons) localized on the adsorbed oxygen and the exact charge distribution are not known. For the convenience of discussion, oxygen adsorption complex will be used to refer the adsorbed oxygen to oxygen vacancies without specifying the charge distribution.

When the adsorption complex is excited by electrons, many electronic processes can occur. Processes that are most relevant to O_2^+ ESD can be:

1. The oxygen in the complex is excited to O_2^+ in a Frank Condon transition, resulting in an O_2^+ less than 2 Å from the surface.

2. This O_2^+ can be ejected from the surface and acquire kinetic energy mainly according to the effective charge of the rest of the adsorption complex. If the surface charge is close to neural, the O_2^+ kinetic energy is mainly converted from the vibrational energy of the excited states. If the charge is positive, the kinetic energy of O_2^+ originates from Coulombic repulsion. Higher kinetic energy is expected from excited adsorption complex with higher positive charge.

3. Any process that influences the charge of the complex should influence the O_2^+ kinetic energy. For example, if the electrons from the valence band are excited to the conduction band, holes are created. The recombination of electrons from the defect state with holes from valence band can remove electrons from defect state making the complex more positively charged. On the other hand, the slow electrons in conduction band can be captured by defect states and the number of electrons trapped can be increased, resulting in less positively charged vacancies. If a core hole is produced, multiple charged states can be created by Auger cascades and vacancies with even more positive charge can be formed. The kinetic energy of ions will thus be determined by the complicated competition and balance between these processes. Thermal excitation of electrons from defect states to the conduction band can also create positively charged complexes.

Based on our understandings of O_2^+ ESD discussed above, the energy dependence of O_2^+ at room temperature can be understood in terms of the presence of different types of adsorption complexes with different effective charges. The slowest O_2^+ component therefore comes from a complex that has the lowest effective positive charge. It can be neutral, or has trapped electrons at the defect state. For the faster components produced at higher incident electron energy, the complex has less electrons trapped or more holes localized at the defect state.

Our previous investigation of electron induced charging on GDC surfaces shows that at room temperature, at lower electron energy trapped electrons dominate at the surface and subsurface areas while at higher electron energy, the concentration of trapped holes at the surface is higher.[86] This can be used to explain the influence of electron energy on O_2^+ ESD. At low incident electron energy, trapped electrons at the defect site

decrease the effective positive charge of the vacancy and therefore the emission of slow O_2^+ is favored. At higher electron energy, hole trapping gains influence over the effective charge and results in the production of faster O_2^+. Multi-hole generation by core level Auger cascades can facilitate the emission of O_2^+ with even higher kinetic energy. The sensitivity of O_2^+ kinetic energy to the effective charge of the surface complex can not only be used to understand the interaction of O_2 with metal oxide surfaces, but also can be used to probe the surface charge and the structure of the adsorption complex. The onset of faster component indicates the onset of effective hole trapping by GDC.

For the O_2^+ energy dependence at high temperature, the lower onset energy for the faster component can be explained by thermal excitation of electrons from the defect states to the conduction band. This excitation leaves the complex one electron less or more positively charged, triggering the emission of fast O_2^+ component. The disappearance of the very fast component is most likely due to the decrease of the life time of the multiply charged state.

The electron irradiation enhanced O_2 adsorption at lower energies at room temperature (See Figure 6.3) is mainly the result of electron trapping at the GDC surface. Since the electron trapping is greatly reduced at high temperature, the electron irradiation enhanced O_2^+ production observed at room temperature should not be observed at high temperature. The electron energy dependence at 560 K presented in Figure 6.5 confirms this.

6.5.2 Types of adsorption complexes

Many investigations have demonstrated that molecular oxygen does not interact with a perfect metal oxide surfaces, but chemisorbs at defect sites, especially oxygen vacancies. High resolution scanning tunneling microscopy and density functional calculations showed that at oxygen vacancy sites on CeO_2 (111) surface, the electrons released by oxygen are exclusively localized on lattice cerium ions.[106] On slightly reduced CeO_2 surfaces, isolated vacancies prevail and can be distinguished as two types, surface and sub-surface oxygen vacancies. Two excess electrons always localize on two cerium ions that are nearest neighbors to the vacancy. Linear or triangular surface oxygen vacancies form upon further reduction. For all types of vacancies, only Ce^{3+} ions are coordinated to the defect.[106] Under the experimental conditions used in this study, the dominant defect type for CeO_2 should be isolated oxygen vacancies. On GDC surfaces, the defect type can be [Gd^{3+}—Vacancy—Gd^{3+}].[81] However, the defect type at the grain boundaries might be very different from this simplified picture.

For GDC, an atomistic understanding of the adsorption complex might be helpful. With the above information, typical oxygen vacancy — O_2 adsorption complexes can be constructed with Ce^{3+}, Ce^{4+}, and Gd^{3+} on a (111) surface. A simplified schematic of these is presented in Figure 6.7. On the (111) surface, an oxygen vacancy is coordinated by six O^{2-} ions on the topmost layer and three cations in the second layer. In the diagram, the O^{2-} ions in the first layer are omitted for the clarity. On GDC surface, the vacancies with two electrons trapped can have the configuration of A1, A2, and A3. Adsorption of O_2 on these defect sites can form an adsorption complex analogous to O_2^{2-} in the literature. Vacancies with one electron trapped can be B1 and B2, and O_2 adsorption to this type of vacancy may form O_2^-. Type C vacancy can be formed either from the ionization of the

B1 oxygen vacancy or formed from A3 by Auger double ionization. This configuration can only exist during electron irradiation and should be the type of complex that produces the fastest O_2^+ component.

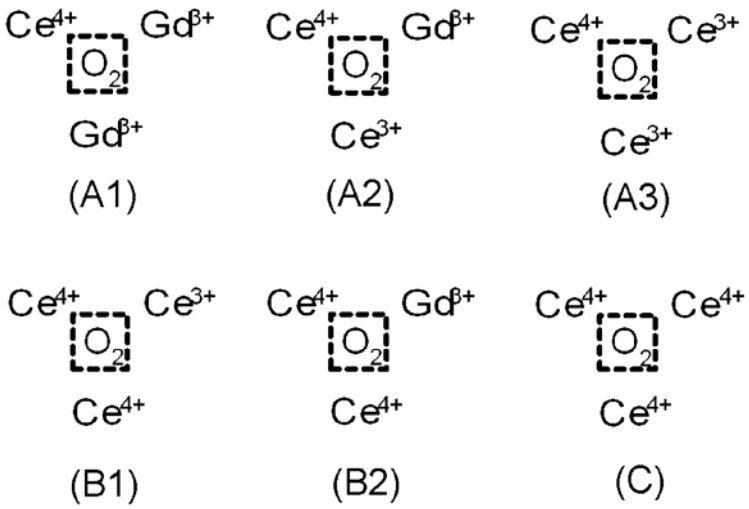

Figure 6.7 Schematic diagram of the adsorption complex of O_2 on isolated oxygen vacancies of GDC surfaces

CHAPTER 7

CONCLUSIONS AND FUTURE DIRECTIONS

7.1 Conclusions

A main conclusion from this thesis project is that electron stimulated desorption (ESD) is very informative in the study of defective polycrystalline metal oxide surfaces. Conventionally, surface charging is considered as a highly undesirable effect in many electron-based characterization techniques and is avoided either by neutralizing the surface charge with a flood electron gun or by not employing electron-based techniques at all. In our ESD study of polycrystalline gadolinia-doped ceria, the influence of surface charging on ESD is systematically investigated, effectively exploited, and fruitfully applied to the understandings of both the physical and chemical nature of defective oxides surfaces and the ESD process itself.

Specifically, the correlation between electron induced surface charging and incident electron energies is experimentally established. The dynamical equilibrium of secondary electron generation, electron trapping, hole trapping, charge neutralization, and charge dissipation processes determine the net charge on the surfaces. The surface charge therefore has signatures on excitation and post-excitation processes. Processes such as adsorption and charge transfer which can be influenced by surface charging are used to probe the surface charge and configuration of related surface defects.

In detail, the use of externally applied potentials to dielectric metal oxides was demonstrated to be a simple way of investigating the electron beam induced charging during the process of electron stimulated ion emission. The influence of surface potentials on ion yields and kinetic energies was experimentally established and applied to the study of electron induced charging of GDC. Externally applied positive potentials increase the cation kinetic energies linearly and negative potentials reduce the cation yields exponentially. The GDC surface can be charged either positively or negatively by electron beam bombardment, depending on the energy of the primary electrons. Irradiation by high energy electrons (for example, 400 eV electrons) produces a positive surface potential while irradiation by low energy electrons (for example, 75 eV electrons) generates a negative sample potential. Electron beam induced positive charge by high energy electron irradiation can be neutralized by subsequent low energy electron irradiation, and vice versa. These observations suggest efficient trapping of both the holes and the electrons by GDC surface. The grain boundary, with the presence of excess gadolinium ions Gd^{3+} and oxygen vacancies, can provide the hole traps as well as electron traps, respectively.

Electron stimulated desorption of H^+, O^+, and H_3O^+ from gadolinia-doped ceria surfaces was investigated by threshold and temperature dependence measurements. The threshold data of H^+ (22, 40, and 75 eV) and H_3O^+ (22 and 40 eV) indicate the presence of hydroxyl groups and chemically adsorbed water molecules on the GDC surfaces. The thresholds of O^+ (~ 40, ~ 150 eV) may suggest bond breaking of Gd-O as an origin of O^+ desorption and the involvement of oxygen vacancies in O^+ desorption. The temperature dependence of cation ESD at different incident electron energies suggested preferential

water adsorption on surface oxygen vacancy sites. The interaction of water with oxygen vacancies influences the desorption of H^+, O^+ and H_3O^+ as well as the oxygen surface exchange reaction of GDC. An activation energy of 0.21 eV for O^+ desorption was obtained from the temperature dependence of ESD of O^+ at 400 eV. This energy is close to the energy needed for the production of an oxygen vacancy associated with two Ce^{3+} on ceria surfaces, and therefore may indicate a correlation between the ESD O^+ yield and oxygen vacancy density on GDC surfaces.

The investigation of highly efficient electron stimulated O^+ desorption from gadolinia-doped ceria surfaces annealed at 850 K in ultrahigh vacuum shows that O^+ ESD is mainly from the electronic excitation of Ce 5s and Gd 5s core levels. The high emission efficiency results from the increased overall density of oxygen vacancies and particularly the density of vacancy clusters. The chemical environment of oxygen ions and the occupancy of defect states can influence the electron density of oxygen anions and therefore the probability of O^+ desorption. Water and molecular oxygen interactions with GDC surfaces decrease the O^+ desorption yield, indicating that dissociative or non-dissociative adsorption of these molecules occurs at vacancy sites. Surface potentials deduced from O^+ kinetic energy measurements performed at various incident electron energy and temperatures reveal the surface charging process and an apparent activation energy for charge dissipation is found to be 0.43 eV, not far from the activation energy for ionic conduction of GDC. ESD is demonstrated to be able to provide important information on the kinetics and dynamics of surface charging, charge transport, adsorption and reactions occurring at defective insulating metal oxides materials.

Electron stimulated desorption investigation of O_2^+ desorption from gadolinia-doped ceria surfaces during molecular oxygen adsorption reveals important information on both oxygen adsorption intermediates and also the adsorption sites. The ~13 eV O_2^+ ESD threshold supports a mechanism that the O_2^+ desorption originates from direct ionization of chemically adsorbed O_2. Detailed analysis of the data collectively showed that the slow O_2^+ component can be associated with a adsorption complex with higher number of trapped electrons while the faster components are related to various degrees of hole localization on the surface. ESD is demonstrated to be able to probe intermediate adsorption species such as O_2^-, as well as the positive charge of the surface. This ability makes ESD a valuable technique for surface chemistry and catalysis studies.

7.2 Future directions

Because of the explorative nature of this research project, there are many interesting experimental and theoretical directions to pursue. In this section only the directions related to experimental efforts will be schematically discussed on the basis of our findings and the focus will be given to metal oxides surfaces and ESD.

From our studies, electron stimulated desorption is very sensitive to both the defect density and the defect types on the surfaces. It is therefore logical to compare the ESD behaviors of single crystal oxides and polycrystalline oxides. For GDC, single crystal of $Ce_{0.7}Gd_{0.3}O_{2-x}$ can be prepared and therefore can be used for this purpose. Another path is to prepare a series GDC samples with different grain sizes and study them with ESD. The preparation can be done by varying the annealing temperature and

time, and grain sizes range from a few hundred nanometers up to 10 μm can be achieved. Since the defect distributions on grain boundaries and grains are different and the abundance of grain boundaries is higher on smaller grain size samples, this study should differentiate the contribution of grain boundaries from grains.

As a mater of fact, on the surfaces of polycrystalline mixed metal oxides, the grain boundaries are more defective and therefore should be more ESD active. The ion desorption rate from the grain boundaries should be greater than the desorption rate from the grains. This rate difference makes the imaging of the surface chemical reactivity of grain boundary possible. Currently available ion imaging technique can image the desorbed ion with a spatial resolution around or below 1 μm. The basic imaging setup consists of a time-of-flight mass spectrometer to effectively collect the desorbed ions, a multi-channel plate to convert the ion signals into electron pulses, which produce images on a phosphorous screen that can be recorded by a CCD camera. The ions of interest can be selected by their flight time and the interference between the trajectories of ions has been demonstrated not to be an issue.

To thoroughly understand electron stimulated desorption from GDC surfaces, other techniques may be of great help. One area of interest is the detection of neutral oxygen. Based on MGR mechanism, the cross section of neutral desorption is much greater than ion desorption and neutral desorption channels bear information associated with excitation and post-excitation processes of valence electrons. However, the detection of neutrals is much more difficult than ions. We did observe neutral oxygen with electron impact ionization with QMS detection, but it is very difficult to rule out the interference from ionization of molecular oxygen and water. The more reliable way to detect desorbed

neutrals is to use resonance enhanced multi-photon ionization (REMPI) and this should be rigorously pursued.

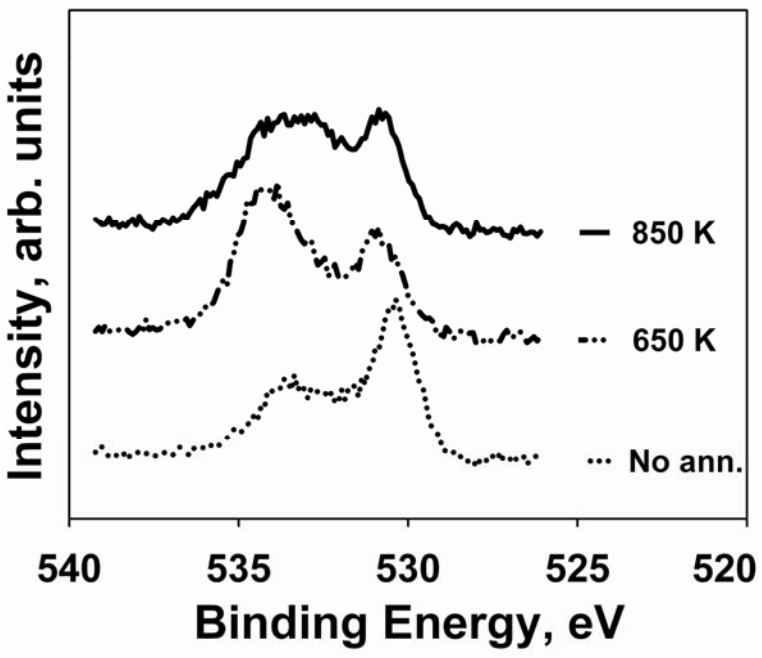

Figure 7.1 XPS O1s spectra of GDC samples treated under different annealing conditions. The spectrum shown from bottom to top is the O1s spectrum for a GDC sample without any ultrahigh vacuum annealing, annealed at 650 K, and annealed at 850 K in ultrahigh vacuum respectively. The binding energy is not corrected for surface charging.

Other surface specific techniques can help deepen our understanding of multiple surface processes. For example, the charge density on oxygen is found to be very influential in the O^+ ESD. X-ray photoelectron spectroscopy (XPS) and X-ray adsorption near- edge spectroscopy (XANES) are efficient in obtaining this information. Performing XPS and XANES study of GDC in comparison with ESD should be interesting. Our preliminary results on the O1s spectra (See Figure 7.1) obtained from GDC samples

annealed in vacuum at different temperatures indeed show the presence of different types of oxygen atoms as a consequence of different sample treatment.

There are many important aspects regarding the fuel cells should be pursued. For example, one should investigate the surface of electrode materials by ESD. Isotope exchange experiments may make the O_2 adsorption process on GDC more specific. Water interaction with O_2 pre-adsorbed surfaces can also be very insightful with regard to hydroxyl radical generation. Overall, further exploration of the ESD study of complicated mixed metal oxides or metal oxides supported metal system, such as catalysts, would be a very rewarding adventure.

REFERENCES

1. Acres GJK. Recent advances in fuel cell technology and its applications. *J. Power Sources* **(2001)**, 100, 60.

2. Appleby AJ. Fuel cell technology: Status and future prospects. *Energy* **(1996)**, 21, 521.

3. Badwal SPS, Foger K. Solid oxide electrolyte fuel cell review. *Ceram. Int.* **(1996)**, 22, 257.

4. Carrette L, Friedrich KA, Stimming U. Fuel cells: Principles, types, fuels, and applications. *ChemPhysChem* **(2000)**, 1, 162.

5. Haile SM. Fuel cell materials and components. *Acta Mater.* **(2003)**, 51, 5981.

6. Ormerod RM. Solid oxide fuel cells. *Chem. Soc. Rev.* **(2003)**, 32, 17.

7. Singhal SC. Advances in solid oxide fuel cell technology. *Solid State Ionics* **(2000)**, 135, 305.

8. Singhal SC. Solid oxide fuel cells for stationary, mobile, and military applications. *Solid State Ionics* **(2002)**, 152-153, 405.

9. Hibino T, Hashimoto A, Yano M, Suzuki M, Yoshida S, Sano M. High performance anodes for SOFCs operating in methane-air mixture at reduced temperatures. *J. Electrochem. Soc.* **(2002)**, 149, A133.

10. Adler SB. Factors governing oxygen reduction in solid oxide fuel cell cathodes. *Chem. Rev.* **(2004)**, 104, 4791.

11. Drinkwine MJ, Lichtman D. Electron Stimulated Desorption - Critical-Review. *Prog. Surf. Sci.* **(1977)**, 8, 123.

12. Madey TE, Yates JT. Electron-Stimulated Desorption as a Tool for Studies of Chemisorption - Review. *J. Vac. Sci. Technol.* **(1971)**, 8, 525.

13. Ramsier RD, Yates JT, Jr. Electron-stimulated desorption: principles and applications. *Surf. Sci. Rep.* **(1991)**, 12, 243.

14. Redhead PA. The first 50 years of electron stimulated desorption (1918-1968). *Vacuum* **(1997)**, 48, 585.

15. Williams EM, Desegovia JL. Electron-Stimulated Desorption of Ions from Surfaces - Techniques, Methodology and Some Recent Findings with Water at Metals and Semiconductors. *Vacuum* **(1989)**, 39, 633.

16. Czyzewsk.Jj, Madey TE, Yates JT. Angular-Distributions of Electron-Stimulated-Desorption Ions - Oxygen on W(100). *Phys. Rev. Lett.* **(1974)**, 32, 777.

17. Orlando TM, Oh D, Sieger MT, Lane CD. Electron collisions with complex targets: Diffraction effects in stimulated desorption. *Phys. Scr., T* **(2004)**, T110, 256.

18. Sieger MT, Orlando TM. Incident beam diffraction in electron stimulated desorption. *Surf. Sci.* **(2000)**, 451, 31.

19. Sieger MT, Schenter GK, Orlando TM. Stimulated desorption by surface electron standing waves. *Phys. Rev. Lett.* **(1999)**, 82, 3348.

20. Menzel D, Gomer R. Desorption from Metal Surfaces by Low-Energy Electrons. *J. Chem. Phys.* **(1964)**, 41, 3311.

21. Redhead PA. Interaction of Slow Electrons with Chemisorbed Oxygen. *Can. J. Phys.* **(1964)**, 42, 886.

22. Antoniewicz PR. Model for Electron-Stimulated and Photon-Stimulated Desorption. *Phys. Rev. B* **(1980)**, 21, 3811.

23. Knotek ML, Feibelman PJ. Ion desorption by core-hole Auger decay. *Phys. Rev. Lett.* **(1978)**, 40, 964.

24. Tanaka S, Mase K, Nagaoka S. Photostimulated ion desorption from the TiO_2(110) and ZnO(10$\bar{1}$ 0) surfaces. *Surf. Sci.* **(2004)**, 572, 43.

25. de Segovia JL, Williams EM. Desorption induced by electronic transitions, DIET, at oxide surfaces. *Chemical Physics of Solid Surfaces* **(2001)**, 9, 608.

26. Cocks ID, Guo Q, Williams EM. ESDIAD studies of the structure of TiO_2(110) (1x1) and (1x2) surfaces and interfaces in conjunction with LEED and STM. *Surf. Sci.* **(1997)**, 390, 119.

27. Rosenberg RA, Wen CR. Photon-Stimulated Desorption of Neutral O_2 from $YBa_2Cu_3O_{7-X}$ by Core-Level Excitation. *Phys. Rev. B* **(1988)**, 37, 9852.

28. Rosenberg RA, Wen CR. Photon-Stimulated Desorption of O_2 from $YBa_2Cu_3O_{7-X}$. *Phys. Rev. B* **(1988)**, 37, 5841.

29. Rosenberg RA, Wen CR. Photon-Stimulated Desorption and Total-Electron Yield from $DyBa_2Cu_3O_{7-X}$ between 15-180 eV. *Phys. Rev. B* **(1989)**, 39, 6630.

30. Madey TE, Yakshinskiy BV, Ageev VN, Johnson RE. Desorption of alkali atoms and ions from oxide surfaces: Relevance to origins of Na and K in atmospheres of Mercury and the Moon. *J. Geophys. Res-Planet* **(1998)**, 103, 5873.

31. Colera I, Soria E, De Segovia JL, Roman EL, Gonzalez R. Characterization of the MgO(100) surface by electron stimulated desorption. *Vacuum* **(1997)**, 48, 647.

32. Gotoh T, Takagi S, Tominaga G. Observation of ion desorption from magnesium oxide(001) by electron bombardment. *Vacuum* **(1990)**, 41, 213.

33. Guo Q, Cocks I, Williams EM. The adsorption of benzoic acid on a TiO_2(110) surface studied using STM, ESDIAD and LEED. *Surf. Sci.* **(1997)**, 393, 1.

34. Guo Q, Cocks I, Williams EM. The orientation of acetate on a TiO_2(110) surface. *J. Chem. Phys.* **(1997)**, 106, 2924.

35. Eguchi K, Setoguchi T, Inoue T, Arai H. Electrical properties of ceria-based oxides and their application to solid oxide fuel cells. *Solid State Ionics* **(1992)**, 52, 165.

36. Inaba H, Tagawa H. Ceria-based solid electrolytes. *Solid State Ionics* **(1996)**, 83, 1.

37. Kharton VV, Figueiredo FM, Navarro L, Naumovich EN, Kovalevsky AV, Yaremchenko AA, Viskup AP, Carneiro A, Marques FMB, Frade JR. Ceria-based materials for solid oxide fuel cells. *J. Mater. Sci.* **(2001)**, 36, 1105.

38. Mogensen M, Lybye D, Bonanos N, Hendriksen R, Poulsen FW. Factors controlling the oxide ion conductivity of fluorite and perovskite structured oxides. *Solid State Ionics* **(2004)**, 174, 279.

39. Mogensen M, Sammes NM, Tompsett GA. Physical, chemical and electrochemical properties of pure and doped ceria. *Solid State Ionics* **(2000)**, 129, 63.

40. Cheng JG, Zha SW, Huang J, Liu XQ, Meng GY. Sintering behavior and electrical conductivity of $Ce_{0.9}Gd_{0.1}O_{1.95}$ powder prepared by the gel-casting process. *Mater. Chem. Phys.* **(2003)**, 78, 791.

41. Mahata I, Das G, Mishra RK, Sharma BP. Combustion synthesis of gadolinia doped ceria powder. *J. Alloys Compd.* **(2005)**, 391, 129.

42. Marina OA, Bagger C, Primdahl S, Mogensen M. A solid oxide fuel cell with a gadolinia-doped ceria anode: preparation and performance. *Solid State Ionics* **(1999)**, 123, 199.

43. Nguyen TL, Kobayashi K, Honda T, Iimura Y, Kato K, Neghisi A, Nozaki K, Tappero F, Sasaki K, Shirahama H and others. Preparation and evaluation of doped ceria interlayer on supported stabilized zirconia electrolyte SOFCs by wet ceramic processes. *Solid State Ionics* **(2004)**, 174, 163.

44. Rocha RA, Muccillo ENS. Preparation of nanocrystalline gadolinia doped ceria powders by combustion synthesis process. *Br. Ceram. Trans.* **(2003)**, 102, 216.

45. Sin A, Dubitsky Y, Zaopo A, Arico AS, Gullo L, La Rosa D, Siracusano S, Antonucci V, Oliva C, Ballabio O. Preparation and sintering of $Ce_{1-x}Gd_xO_{2-x/2}$ nanopowders and their electrochemical and EPR characterization. *Solid State Ionics* **(2004)**, 175, 361.

46. Xia CR, Liu ML. Microstructures, conductivities, and electrochemical properties of $Ce_{0.9}Gd_{0.1}O_2$ and GDC-Ni anodes for low-temperature SOFCs. *Solid State Ionics* **(2002)**, 152, 423.

47. Yaremchenko AA, Valente AA, Kharton VV, Bashmakov IA, Rocha J, Marques FMB. Direct oxidation of dry methane on nanocrystalline $Ce_{0.8}Gd_{0.2}O_{2-delta}$/Pt anodes. *Catal. Commun.* **(2003)**, 4, 477.

48. Chen L, Chen CL, Huang DX, Lin Y, Chen X, Jacobson AJ. High temperature electrical conductivity of epitaxial Gd-doped CeO_2 thin films. *Solid State Ionics* **(2004)**, 175, 103.

49. Costa ADS, Labrincha JA, Marques FMB. p-Type conductivity in gadolinia-doped ceria. *J. Mater. Sci. Lett.* **(1996)**, 15, 1716.

50. Fagg DP, Kharton VV, Frade JR. P-type electronic transport in $Ce_{0.8}Gd_{0.2}O_{2-delta}$: The effect of transition metal oxide sintering aids. *J.Electroceram.* **(2003)**, 9, 199.

51. Figueiredo FM, Marques FMB, Frade JR. Electron hole conductivity of gadolinia doped ceria. *J. Eur. Ceram. Soc.* **(1999)**, 19, 807.

52. Gourba E, Briois P, Ringuede A, Cassir M, Billard A. Electrical properties of gadolinia-doped ceria thin films deposited by sputtering in view of SOFC application. *J. Solid State Electrochem.* **(2004)**, 8, 633.

53. Ji Y, Kilner JA, Carolan MF. Electrical conductivity and oxygen transfer in gadolinia-doped ceria (CGO)-$Co_3O_{4-delta}$ composites. *J. Eur. Ceram. Soc.* **(2004)**, 24, 3613.

54. Jud E, Gauckler LJ. The effect of cobalt oxide addition on the conductivity of $Ce_{0.9}Gd_{0.1}O_{1.95}$. *J.Electroceram.* **(2005)**, 15, 159.

55. Lubke S, Wiemhofer HD. Electronic conductivity of gadolinia doped ceria. *Ber. Bunsen-Ges. Phys. Chem.* **(1998)**, 102, 642.

56. Navarro I, Marques F, Frade J. n-type conductivity in gadolinia-doped ceria. *J. Electrochem. Soc.* **(1997)**, 44, 267.

57. Ruiz-Trejo E, Sirman JD, Baikov YM, Kilner JA. Oxygen ion diffusivity, surface exchange and ionic conductivity in single crystal gadolinia doped ceria. *Solid State Ionics* **(1998)**, 113-115, 565.

58. Kharton VV, Kovalevsky AV, Viskup AP, Shaula AL, Figueiredo FM, Naumovich EN, Marques FMB. Oxygen transport in $Ce_{0.8}Gd_{0.2}O_{2-delta}$-based composite membranes. *Solid State Ionics* **(2003)**, 160, 247.

59. Lane JA, Kilner JA. Oxygen surface exchange on gadolinia doped ceria. *Solid State Ionics* **(2000)**, 136-137, 927.

60. Yashiro K, Onuma S, Kaimai A, Nigara Y, Kawada T, Mizusaki J, Kawamura K, Horita T, Yokokawa H. Mass transport properties of $Ce_{0.9}Gd_{0.1}O_{2-delta}$ at the surface and in the bulk. *Solid State Ionics* **(2002)**, 1 52, 469.

61. Martinez-Arias A, Hungria AB, Fernandez-Garcia M, Iglesias-Juez A, Conesa JC, Mather GC, Munuera G. Cerium-terbium mixed oxides as potential materials for anodes in solid oxide fuel cells. *J. Power Sources* **(2005)**, 151, 43.

62. De Souza S, Visco SJ, De Jonghe LC. Reduced-temperature solid oxide fuel cell based on YSZ thin-film electrolyte. *J. Electrochem. Soc.* **(1997)**, 144, L35.

63. Minh NQ. Ceramic fuel cells. *J. Am. Ceram. Soc.* **(1993)**, 76, 563.

64. Suzuki T, Kosacki I, Anderson HU. Microstructure-electrical conductivity relationships in nanocrystalline ceria thin films. *Solid State Ionics* **(2002)**, 151, 111.

65. Xia C, Liu M. Novel cathodes for low-temperature solid oxide fuel cells. *Adv. Mater. (Weinheim, Ger.)* **(2002)**, 14, 521.

66. Steele BCH. Appraisal of $Ce_{1-y}Gd_yO_{2-y/2}$ electrolytes for IT-SOFC operation at 500 DegC. *Solid State Ionics* **(2000)**, 129, 95.

67. Manning PS, Sirman JD, Kilner JA. Oxygen self-diffusion and surface exchange studies of oxide electrolytes having the fluorite structure. *Solid State Ionics* **(1996)**, 93, 125.

68. Torquemada MC, de Segovia JL, Roman E. Reactivity of CO on a TiO_2(110) defective surface studied by electron stimulated desorption. *Surf. Sci.* **(1995)**, 337, 31.

69. Simpson WC, Wang WK, Yarmoff JA, Orlando TM. Photon- and electron-stimulated desorption of O^+ from zirconia. *Surf. Sci.* **(1999)**, 423, 225.

70. Orlando TM, Aleksandrov AB, Herring J. Electron-Stimulated Desorption of H^+, H_2^+, OH^+, and $H^+(H_2O)_n$ from Water-Covered Zirconia Surfaces. *J. Phys. Chem. B* **(2003)**, 107, 9370.

71. Lei Y, Ito Y, Browning ND, Mazanec TJ. Segregation effects at grain boundaries in fluorite-structured ceramics. *J. Am. Ceram. Soc.* **(2002)**, 85, 2359.

72. Norenberg H, Briggs GAD. Defect Structure of Nonstoichiometric $CeO_2(111)$ Surfaces Studied by Scanning Tunneling Microscopy. *Phys. Rev. Lett.* **(1997)**, 79, 4222.

73. Herring J, Aleksandrov A, Orlando T. Stimulated Desorption of Cations from Pristine and Acidic Low-temperature Water Ice Surface. *Phys. Rev. Lett.* **(2004)**, 92, 187602.

74. Afanas'ev VV, Stesmans A. Hole trapping in ultrathin Al_2O_3 and ZrO_2 insulators on silicon. *Appl. Phys. Lett.* **(2002)**, 80, 1261.

75. Afanas'ev VV, Stesmans A. Stable trapping of electrons and holes in deposited insulating oxides: Al_2O_3, ZrO_2, and HfO_2. *J. Appl. Phys.* **(2004)**, 95, 2518.

76. Aleksandrov AB, Aluker ED, Vasiliev IA, Nechaev AF. Introduction to Radiation Physics and Chemistry of Alkali Halide Crystals Interface; 1989. 247 p.

77. Simpson WC, Orlando TM, Parenteau L, Nagesha K, Sanche L. Dissociative electron attachment in nanoscale ice films: Thickness and charge trapping effects. *J. Chem. Phys.* **(1998)**, 108, 5027.

78. Bass AD, Cloutier P, Sanche L. Measurements of charge accumulation induced by monochromatic low-energy electrons at the surface of insulating samples. *J. Appl. Phys.* **(1998)**, 84, 2740.

79. Vallayer B, Blaise G, Treheux D. Space charge measurement in a dielectric material after irradiation with a 30 kV electron beam: Application to single-crystals oxide trapping properties. *Rev. Sci. Instrum.* **(1999)**, 70, 3102.

80. Liebault J, Zarbout K, Moya-Siesse D, Bernardini J, Moya G. New technique to characterize thin oxide films under electronic irradiation. *Appl. Surf. Sci.* **(2003)**, 212-213, 809.

81. Inaba H, Sagawa R, Hayashi H, Kawamura K. Molecular dynamics simulation of gadolinia-doped ceria. *Solid State Ionics* **(1999)**, 122, 95.

82. Norenberg H, Briggs GAD. The surface structure of CeO_2(110) single crystals studied by STM and RHEED. *Surf. Sci.* **(1999)**, 433-435, 127.

83. Skorodumova NV, Simak SI, Lundqvist BI, Abrikosov IA, Johansson B. Quantum origin of the oxygen storage capability of ceria. *Phys. Rev. Lett.* **(2002)**, 89, 166601/1.

84. Petot-Ervas G, Petot C, Raulot JM, Kusinski J, Sproule I, Graham M. Role of the microstructure on the transport properties of Y-doped zirconia and Gd-doped ceria. *Ionics* **(2003)**, 9, 195.

85. Ramaker DE. Covalent interaction effects in electron/photon-stimulated desorption. *J. Vac. Sci. Technol., A* **(1983)**, 1, 1137.

86. Chen H, Chen Y, Aleksandrov A, Dong J, Liu M, Orlando TM. Charging effects on electron-stimulated desorption of cations from gadolinia-doped ceria surfaces. *Appl. Surf. Sci.* **(2005)**, 243, 166.

87. Song HZ, Wang HB, Zha SW, Peng DK, Meng GY. Aerosol-assisted MOCVD growth of Gd_2O_3-doped CeO_2 thin SOFC electrolyte film on anode substrate. *Solid State Ionics* **(2003)**, 156, 249.

88. Raiser D, Deville JP. Study of XPS photoemission of some gadolinium compounds. *J. Electron Spectrosc. Relat. Phenom.* **(1991)**, 57, 91.

89. Wandelt K, Brundle CR. The interaction of oxygen with gadolinium: UPS and XPS studies. *Surf. Sci.* **(1985)**, 157, 162.

90. Emeline AV, Kataeva GV, Ryabchuk VK, Serpone N. Photostimulated generation of defects and surface reactions on a series of wide band gap metal-oxide solids. *J. Phys. Chem. B* **(1999)**, 103, 9190.

91. Teterin YA, Teterin AY, Lebedev AM, Utkin IO. X-ray photoelectron spectra of oxygen-containing cerium compounds. *Radiochemistry (Moscow)(Translation of Radiokhimiya)* **(1998)**, 40, 101.

92. Kundakovic L, Mullins DR, Overbury SH. Adsorption and reaction of H_2O and CO on oxidized and reduced Rh/CeO_x(111) surfaces. *Surf. Sci.* **(2000)**, 457, 51.

93. Loubriel G, Knotek ML, Stulen RH, Koel BE, Parks CC. Photon- and electron-stimulated desorption from rare earth oxides. *J. Vac. Sci. Technol., A* **(1983)**, 1, 1145.

94. Koel BE, Loubriel GM, Knotek ML, Stulen RH, Rosenberg RA, Parks CC. Resonant photon-stimulated desorption of ions from oxidized cerium. *Phys. Rev. B: Condens. Matter Mater. Phys.* **(1982)**, 25, 5551.

95. Sieger MT, Simpson WC, Orlando TM. Electron-stimulated desorption of D^+ from D_2O ice: Surface structure and electronic excitations. *Phys. Rev. B* **(1997)**, 56, 4925.

96. Henderson MA, Perkins CL, Engelhard MH, Thevuthasan S, Peden CHF. Redox properties of water on the oxidized and reduced surfaces of CeO_2(1 1 1). *Surf. Sci.* **(2003)**, 526, 1.

97. Sakai N, Yamaji K, Horita T, Xiong YP, Kishimoto H, Yokokawa H. Effect of water on oxygen transport properties on electrolyte surface in SOFCs. I. Surface reaction mechanism of oxygen isotope exchange on solid oxide electrolytes. *J. Electrochem. Soc.* **(2003)**, 150, A689.

98. Kilner JA, Steele BCH. Mass transport in anion-deficient fluorite oxides. *Nonstoichiom. Oxides* **(1981)** 233.

99. Kharton VV, Marques FMB, Atkinson A. Transport properties of solid oxide electrolyte ceramics: a brief review. *Solid State Ionics* **(2004)**, 174, 135.

100. Park S, Gorte RJ, Vohs JM. Applications of heterogeneous catalysis in the direct oxidation of hydrocarbons in a solid-oxide fuel cell. *Appl. Cata. A-General* **(2000)**, 200, 55.

101. Hart NT, Brandon NP, Day MJ, Lapena-Rey N. Functionally graded composite cathodes for solid oxide fuel cells. *J. Power Sources* **(2002)**, 106, 42.

102. Leng YJ, Chan SH, Jiang SP, Khor KA. Low-temperature SOFC with thin film GDC electrolyte prepared in situ by solid-state reaction. *Solid State Ionics* **(2004)**, 170, 9.

103. Ralph JM, Rossignol C, Kumar R. Cathode materials for reduced-temperature SOFCs. *J. Electrochem. Soc.* **(2003)**, 150, A1518.

104. Tsoga A, Gupta A, Naoumidis A, Nikolopoulos P. Gadolinia-doped ceria and yttria stabilized zirconia interfaces: Regarding their application for SOFC technology. *Acta Mater.* **(2000)**, 48, 4709.

105. Diebold U. The surface science of titanium dioxide. *Surf. Sci. Rep.* **(2003)**, 48, 53.

106. Esch F, Fabris S, Zhou L, Montini T, Africh C, Fornasiero P, Comelli G, Rosei R. Electron Localization Determines Defect Formation on Ceria Substrates. *Science (Washington, DC, U. S.)* **(2005)**, 309, 752.

107. Norenberg H, Briggs GAD. Defect formation on CeO_2(111) surfaces after annealing studied by STM. *Surf. Sci.* **(1999)**, 424, L352.

108. Bird DPC, de Castilho CMC, Lambert RM. Catalyst genesis studied by atomic force microscopy. *Surf. Sci.* **(2000)**, 449, L221.

109. Fukui K, Namai Y, Iwasawa Y. Imaging of surface oxygen atoms and their defect structures on CeO_2(111) by noncontact atomic force microscopy. *Appl. Surf. Sci.* **(2002)**, 188, 252.

110. Fukui K, Takakusagi S, Tero R, Aizawa M, Namai Y, Iwasawa Y. Dynamic aspects and associated structures of TiO_2(110) and CeO_2(111) surfaces relevant to oxide catalyses. *Phys. Chem. Chem. Phys.* **(2003)**, 5, 5349.

111. Namai Y, Fukui K, Iwasawa Y. Atom-resolved noncontact atomic force microscopic observations of CeO_2(111) surfaces with different oxidation states: Surface structure and behavior of surface oxygen atoms. *J. Phys. Chem. B* **(2003)**, 107, 11666.

112. Namai Y, Fukui K, Iwasawa Y. The dynamic behaviour of CH_3OH and NO_2 adsorbed on CeO_2(111) studied by noncontact atomic force microscopy. *Nanotechnology* **(2004)**, 15, S49.

113. Namai Y, Fukui KI, Iwasawa Y. Atom-resolved noncontact atomic force microscopic and scanning tunneling microscopic observations of the structure and dynamic behavior of CeO_2(111) surfaces. *Catal. Today* **(2003)**, 85, 79.

114. Chen H, Aleksandrov A, Chen Y, Zha S, Liu M, Orlando TM. Probing Water Interactions and Vacancy Production on Gadolinia-Doped Ceria Surfaces Using Electron Stimulated Desorption. *J. Phys. Chem. B* **(2005)**, 109, 11257.

115. Teterin YA, Teterin AY, Lebedev AM, Utkin IO. The XPS spectra of cerium compounds containing oxygen. *J. Electron Spectrosc. Relat. Phenom.* **(1998)**, 88-91, 275.

116. Liu G, Rodriguez JA, Hrbek J, Dvorak J, Peden CHF. Electronic and chemical properties of $Ce_{0.8}Zr_{0.2}O_2$(111) surfaces: Photoemission, XANES, density-functional, and NO_2 adsorption studies. *J. Phys. Chem. B* **(2001)**, 105, 7762.

117. Yakshinskiy B, Akbulut M, Madey TE. Transmission of low-energy (<10 eV) O^+ ions through Au films on TiO_2(110). *Surf. Sci.* **(1997)**, 390, 132.

118. Kharton VV, Viskup AP, Figueiredo FM, Naumovich EN, Yaremchenko AA, Marques FMB. Electron-hole conduction in Pr-doped Ce(Gd)$O_{2\text{-delta}}$ by faradaic efficiency and emf measurements. *Electrochim. Acta* **(2001)**, 46, 2879.

119. Xia C, Liu M. Low-temperature SOFCs based on $Gd_{0.1}Ce_{0.9}O_{1.95}$ fabricated by dry pressing. *Solid State Ionics* **(2001)**, 144, 249.

120. Trovarelli A, editor. Catalysis by Ceria and Related Materials. Volume 2: Imperial College Press; 2002. 508 p.

121. Putna ES, Vohs JM, Gorte RJ. Evidence for weakly bound oxygen on ceria film. *J. Phys. Chem.* **(1996)**, 100, 17862.

122. Labanowska M. EPR monitoring of redox processes in transition metal oxide catalysts. *ChemPhysChem* **(2001)**, 2, 712.

123. Soria J, Martinez-Arias A, Conesa JC. Spectroscopic study of oxygen adsorption as a method to study surface defects on CeO_2. *J. Chem. Soc., Faraday Trans.* **(1995)**, 91, 1669.

124. Zhang X, Klabunde KJ. spectroscopic study of oxygen adsorption as a method to study surface defects on CeO_2. *Inorg. Chem.* **(1992)**, 31, 1707.

125. Hernandez-Alonso MD, Hungria AB, Martinez-Arias A, Fernandez-Garcia M, Coronado JM, Conesa JC, Soria J. EPR study of the photoassisted formation of radicals on CeO_2 nanoparticles employed for toluene photooxidation. *Appl. Catal., B* **(2004)**, 50, 167.

126. Coronado JM, Javier Maira A, Martinez-Arias A, Conesa JC, Soria J. EPR study of the radicals formed upon UV irradiation of ceria-based photocatalysts. *J. Photochem. Photobiol., A* **(2002)**, 150, 213.

127. Pushkarev VV, Kovalchuk VI, D'Itri JL. Probing Defect Sites on the CeO_2 Surface with Dioxygen. *J. Phys. Chem. B* **(2004)**, 108, 5341.

128. Sakamoto K, Nakatsuji K, Daimon H, Yonezawa T, Suga S. Electron-Stimulated Desorption (Esd) of the O_2 Si(111) Surface. *Surf. Sci.* **(1994)**, 306, 93.

129. Rocker GH, Huang C, Cobb CL, Redding JD, Metiu H, Martin RM. The Interaction of Oxygen and Potassium on the Ru(001) Surface. *Surf. Sci.* **(1991)**, 250, 33.

130. Krishnakumar E, Srivastava SK. Cross-Sections for Electron-Impact Ionization of O_2. *Int. J. Mass Spectrom. Ion Processes* **(1992)**, 113, 1.

131. Anpo M, Che M, Fubini B, Garrone E, Giamello E, Paganini MC. Generation of superoxide ions at oxide surfaces. *Top. Catal.* **(1999)**, 8, 189.

132. Anpo M, Aikawa N, Kubokawa Y, Che M, Louis C, Giamello E. Photoluminescence and Photocatalytic Activity of Highly Dispersed Titanium-Oxide Anchored onto Porous Vycor Glass. *J. Phys. Chem.* **(1985)**, 89, 5017.

133. Pacchioni G, Ferrari AM, Giamello E. Cluster model of O_2^- adsorption on regular and defect sites and F-s centers of the MgO(100) surface. *Chem. Phys. Lett.* **(1996)**, 255, 58.